ICARUS 74, 172–230 (1988)

Tidal Evolution of the Uranian Satellites

I. Passage of Ariel and Umbriel through the 5 : 3 Mean-Motion Commensurability

WILLIAM C. TITTEMORE AND JACK WISDOM

Department of Earth, Atmospheric, and Planetary Sciences, Massachusetts Institute of Technology, Cambridge, Massachusetts 02139

Received June 17, 1987; revised November 9, 1987

Ariel and Umbriel have passed through the 5 : 3 mean-motion commensurability if the specific dissipation function (Q) for Uranus is less than about 100,000. There is a significant chaotic zone associated with this resonance. Due to the presence of this chaotic zone, the standard theory describing passage through orbital resonances is not applicable. In particular, there are significant changes in the mechanism for and probability of capture into resonance. Tidal evolution within the chaotic zone may have driven orbital eccentricities to relatively high values, with some probability of escape from resonance remaining. In the planar approximation, eccentricities high enough to have a significant effect on the thermal history of Ariel have not been found. © 1988 Academic Press, Inc.

1. INTRODUCTION

The major satellites of Uranus are not presently involved in any mean-motion commensurabilities. However, a number of low-order resonances between various satellites may have been encountered in the past as the orbits of the satellites evolved as a result of tidal friction (see Peale 1988 for a recent review). The present eccentricities of the inner large satellites are anomalously high when the time scales of eccentricity damping due to tides raised on the satellites by Uranus are considered (Squyres *et al.* 1985), and this cannot be accounted for by the mutual perturbations alone (Dermott and Nicholson 1986, Laskar 1986). Also, the recent observations by Voyager 2 (Smith *et al.* 1986) of extensive resurfacing of Miranda, Ariel, and Titania indicate that the thermal histories of these satellites have been spectacular. The importance of tidal heating in the thermal balance of satellites has been demonstrated in the melting of Io due to tides raised by Jupiter on this satellite (Peale *et al.* 1979), and the possibility that analogous phenomena have significantly affected the Uranian satellites warrants investigation.

Dermott (1984) has suggested that resonant motion of the Uranian satellites may be chaotic. His argument is based on the resonance overlap criterion, which provides a useful criterion for predicting the onset of large-scale chaotic behavior in many systems (see Chirikov 1979). For the satellite systems of Jupiter and Saturn, the group of resonances associated with a particular mean-motion commensurability are well separated by precession induced by the planetary oblateness. However, the J_2 of Uranus is small ($J_2 \approx 0.0033$) and the resonances associated with any particular mean-motion commensurability between the Uranian satellites are not well separated. Dermott argues that the resonance overlap criterion then implies that there should be chaotic behavior. While Dermott was correct in pointing out the importance of the small J_2 for the motion of the Uranian satellites, the specific application of the resonance overlap criterion is incorrect. The overlap criterion states that chaotic behavior ensues when the sum of the libration

0019-1035/88 $3.00

half-widths of two neighboring resonances is larger than their separation. Intuitively, two independent combinations of the variables in the problem cannot simultaneously librate. For example, if $\sigma_1 = \theta_1 - \theta_2$ oscillates about zero while both θ_1 and θ_2 are circulating, then the possibility of the simultaneous oscillation of $\sigma_2 = \theta_1 - 2\theta_2$ is excluded. If a "good" perturbation theory suggests that both variables should oscillate then chaotic behavior most likely results. For mean-motion resonances the situation is more complicated. Different resonance variables may correspond to independent degrees of freedom. In this case the libration of one resonance is independent of the libration of the other resonance. In the example above, the oscillation or circulation of θ_1 may be completely independent of the oscillation or circulation of θ_2. The fact that a system is in a region of phase phase where both θ_1 and θ_2 oscillate does not indicate the presence of chaotic behavior. In this case the simultaneous libration of independent combinations of θ_1 and θ_2 is not prohibited. Wisdom (1985a) has shown that "overlapping" resonances belonging to the same mean-motion commensurability do not necessarily lead to chaotic behavior, but also that chaotic behavior may result from only a single mean-motion resonance if accompanied by the proper secular terms. For example, the mathematical problem of motion near a first-order commensurability in the elliptic restricted three-body problem, taking into account only the two resonances which are first order in eccentricity, is integrable, even though there is strong "overlap" of the region of libration in the individual resonances (see Wisdom 1987 and references therein). No simple argument about overlapping mean-motion resonances can predict whether large-scale chaos exists. A proper application of the resonance overlap criterion involves checking for the overlap of regions of libration of independent resonances between the degrees of freedom. In any case, the proximity of several resonances in the situation where J_2 is small certainly enhances the likelihood of interesting dynamical behavior.

The theory of passage through isolated mean-motion commensurabilities between satellites is well developed (Allan 1969, Sinclair 1972, 1974, Yoder 1979, Henrard and Lemaitre 1983, Lemaitre 1984, Borderies and Goldreich 1984). The work of Henrard (1987), in particular, places the theory of passage through mean-motion resonances in a general framework of passage through isolated resonances. The single resonance theory can be used to compute the probability of capture into a mean-motion commensurability, and the changes in the eccentricity or inclination as the resonance is encountered, *provided the assumptions which have been made in deriving the formulas are satisfied.* Unfortunately, critical assumptions of the single resonance derivation are not valid for the Uranian satellites. First, the Hamiltonian which is used in the derivation of the single resonance formulas is assumed to be well represented by the terms from the disturbing function involving a single resonant argument, and actually more commonly by a single resonant term from the disturbing potential. However, since the J_2 of Uranus is small ($J_2 \approx 0.0033$) the resonances are not well separated, and the quasiperiodic resonance regions can be significantly different from those predicted by single resonance approximations. In some cases alternate formulas could be derived which are based on the more complete resonance Hamiltonian, though to our knowledge calculations of this sort have not as yet been published (see, however, Tittemore and Wisdom 1988). A more fundamental problem with the standard single resonance theory is that the motion at the point of capture into resonance is assumed to be regular, i.e., quasiperiodic. Whether the trajectory is captured or escapes depends on the (generally unknown) phase of the resonant argument as the separatrix is encountered. The separatrix is the regular trajectory of the single resonance problem which separates regions where the resonant

argument librates from regions where it circulates. The "decision" of capture or escape is made on a single libration and depends on the phase at which the separatrix is encountered. A capture probability is defined by assuming some initial distribution of phases and is computed by evaluating certain integrals along the separatrix. The assumption of a regular, quasiperiodic separatrix completely permeates the existing theory of passage through mean-motion resonances. Generically, though, the motion near a separatrix is chaotic, not quasiperiodic (see e.g., Chirikov 1979). Thus the boundary has a finite width. The motion near the separatrix is no longer the motion assumed by the isolated resonance theory. The presence of the chaotic zone will be unimportant if the chaotic zone is so small that it is crossed in a time short compared to a libration period, for then the chaotic dynamics are indistinguishable from the regular dynamics assumed in the standard theory of passage through resonance. On the other hand, if the region of chaotic behavior near the separatrix is large enough that the trajectory has enough time to make significant chaotic wanderings during the transition then *there is no reason to believe that the single resonance predictions have any relevance at all.* The process of passage through resonance has qualitatively changed. As will be demonstrated below there are significant chaotic zones near mean-motion commensurabilities between the Uranian satellites. Thus predictions based on the single resonance model are highly suspect, and most likely irrelevant. The importance of the chaotic separatrix in changing the mechanism of capture was previously pointed out by Wisdom *et al.* (1984).

This paper is the first of a series of papers which will systematically examine the tidal evolution of the orbits and spins of the Uranian satellites. The full extent of the tidal evolution of the Uranian satellites is unknown, since the magnitude of the specific dissipation function (Q) for Uranus is unknown. Our systematic examination begins then with the current configuration and proceeds backward in time. Hopefully, at some point a barrier will be reached, through which evolution to the present configuration will be impossible or unlikely. The requirement that that configuration has never been encountered would then provide a constraint on the Q of Uranus.

In this, our first study, we consider only the Ariel–Umbriel 5 : 3 mean-motion commensurability. The 5 : 3 commensurability between Ariel and Umbriel would have been the most recently encountered of the first- and second-order commensurabilities between the Uranian satellites. For this commensurability there are three important mean-motion resonances involving the eccentricities and three involving the inclinations, as well as a strong secular coupling. The 5 : 3 resonance therefore promises to be quite interesting.

We consider the Ariel–Umbriel 5 : 3 resonant interaction in the planar approximation. The restriction to the planar problem has been made in an effort to get some understanding of the dynamical mechanisms involved in the passage through such a complicated resonance. The planar system has the advantage of being reducible to two degrees of freedom, which allows the detailed study of the phase space using the Poincaré surface of section technique. This technique has been found to be invaluable for understanding the qualitative features of motion of asteroids in the 3 : 1 Kirkwood gap (Wisdom 1985a).

In Section 2, the planar resonant Hamiltonian of the system is discussed, the full development being given in Appendix I. Since the masses of the satellites are comparable, a treatment of the full resonant three-body problem is required. The evolution of the system is studied with the aid of an algebraic mapping with the same resonant structure as this three-body problem, analogous to that developed by Wisdom (1982, 1983) for the restricted problem to

study resonant asteroid motion. The map and its derivation are given in Appendix II.

In Section 3 some aspects of the dynamics of the 5:3 Ariel–Umbriel mean-motion commensurability are exhibited. Surfaces of section for this system reveal the presence of significant chaotic zones, even for relatively low eccentricities. A pair of islands on the surfaces of section may be associated with the normal modes of the linear secular theory. The development of large-scale chaotic zones is associated with the fixed point associated with one of these modes becoming unstable.

Section 4 explores the evolution of the system through the resonance with small tidal dissipation included. Results are compiled for five numerical runs with distinct families of initial conditions. In each case large numbers of trajectories have been followed to assess the probabilities of various outcomes. It is found that the satellites can be driven to relatively high eccentricities in the chaotic zone and still escape from the resonance. The maximum eccentricities during passage through resonance are always found to be higher than the initial values and occur during the chaotic phase of the resonance encounter. The mechanism of capture is markedly different from that of the isolated resonance theory. In the single resonance picture capture or escape occurs depending on the phase of the trajectory as the regular separatrix is encountered. For the 5:3 commensurability the "decision" of capture or escape occurs while the motion is chaotic. The trajectory approaches the resonance from a quasiperiodic region of phase space in which the resonant arguments circulate. There is another quasiperiodic circulation region on the other side of the resonance, into which trajectories may escape. In the resonance region the phase space is dominated by a large chaotic zone. The chaotic zone acts as a bridge between these two quasiperiodic regions. If, during the period of chaotic evolution, the trajectory becomes trapped in the second region of quasiperiodic circulation, the trajectory escapes from the resonance. If, on the other hand, the trajectory remains in the chaotic zone, then the energy surface eventually divides the phase space into two regions in which libration of one or more resonant arguments must occur. At this point capture into resonance has occurred, *even though the trajectory may still be chaotic.* Upon further evolution those trajectories which were chaotic at the point of capture eventually become quasiperiodic librators. The probability of escape depends not only on the eccentricities of the satellites far from the resonance, which vary considerably due to the strong secular interaction, but also on the initial distribution of energy between the two secular modes. The coupled nature of the problem makes comparison with the standard single resonance model of evolution through resonances impossible. Even qualitative features of passage through resonance differ from the picture developed for passage through isolated resonances. For example, the average eccentricity of Umbriel after escape from the resonance can be higher than the average value before the resonance is encountered. In the standard theory, the eccentricity after escape is always smaller.

Section 5 discusses physical applications of these results. Final eccentricities of escaping trajectories are consistent with the present values. Eccentricities high enough to have had a significant effect on the thermal history of Ariel have not been found so far in this study. This may be due to limitations of the planar approximation; higher eccentricities may be possible in the full three-dimensional problem (see Wisdom 1983, 1987).

Since we are concerned with the determination of the probabilities of various outcomes of tidal evolution in a complicated dynamical environment we have as a check verified that our methods properly reproduce the known capture probabilities in the single resonance approximation. Appendix III discusses these results.

2. THE RESONANT HAMILTONIAN

This study looks at the system of Uranus and its satellites. The planet is considered to be the dominating mass, which is symmetric about its rotation axis, and the satellites are considered to be $n - 1$ point masses. The gravitational potential of this system can be written

$$U = -\sum_{i=1}^{n-1} \frac{GMm_i}{r_i}\left[1 + \sum_{l=2}^{\infty} J_l \left(\frac{R}{r_i}\right)^l P_l(\sin \varphi_i)\right] - \sum_{i<j<n} \frac{Gm_i m_j}{r_{ij}}, \quad (1)$$

where the satellite index i increases with the satellite's distance from the planet. G is the gravitational constant, M is the mass of Uranus, m_i are the satellite masses, r_i are the distances of the satellites from Uranus, R is the planet radius, J_l are the gravitational harmonic coefficients, P_l are Legendre polynomials, φ_i are the satellite latitudes with respect to the planet equator, and r_{ij} are the distances between the satellites.

To first order in the ratios of satellite masses to planet mass, the total Hamiltonian for the system can be written

$$\mathcal{H} = -\sum_{i=1}^{n-1} \frac{GMm_i}{2a_i}\left[1 + \sum_{l=2}^{\infty} J_l \left(\frac{R}{a_i}\right)^l P_l(\sin \varphi_i)\right] - \sum_{i<j<n} \frac{Gm_i m_j}{a_j} R_{ij}, \quad (2)$$

where R_{ij} is the disturbing function (see, for example, Leverrier 1855). This Hamiltonian represents a set of $n - 1$ perturbed Kepler problems. The lowest order terms in the perturbations due to spherical harmonics are of order $J_2(R/a_i)^2$ relative to the Keplerian terms. The lowest order terms in the disturbing function are of order a_i/a_j, so these perturbations are of order $(m_i/M)(a_i/a_j)$ relative to the Keplerian terms. In the case of Uranus and its satellites, the effects of these two types of perturbation are of similar magnitude (see Table I). This has important consequences for the evolution.

TABLE I

PHYSICAL PARAMETERS

Units:
- Mass: mass of Uranus: $GM = 5.794 \times 10^6$ km^3 sec^{-1} (Stone and Miner 1986)
- Distance: radius of Uranus: $R = 26{,}200$ km (French *et al.* 1985)
- Time: years

$\frac{m_A}{M} = 0.0000155$, $\frac{m_U}{M} = 0.0000147$ (Stone and Miner 1986)

$R_A = 0.0221R$, $R_U = 0.0227R$ (Stone and Miner 1986)

$e_A = 0.0017$, $e_U = 0.0043$ (Peale 1988)

Potential Love number of Uranus: $k_2 = 0.104$ (Gavrilov and Zharkov 1977)

Shear modulus (rigidity) of satellites: $\mu = 3 \times 10^6$ ($\approx 10^{11}$ dynes/cm)

Potential Love numbers of satellites, using the expression:

$$k_{2i} = \frac{3/2}{1 + 19\mu_i/(2\rho_i g_i R_i)} \approx \frac{3\rho_i g_i R_i}{19\mu_i}$$

$k_{2A} = 4.1 \times 10^{-3}$, $k_{2U} = 3.3 \times 10^{-3}$

Specific dissipation functions: $Q_A \approx Q_U \approx 100$

Spherical harmonic of Uranus: $J_2 = 0.0033461$ (French *et al.* 1985)

In this paper all terms in the disturbing function involving inclinations are set equal to zero. Since the inclinations are less than one degree, this is a reasonable first approximation. Recall, though, that taking into account the inclinations in the 3 : 1 asteroid–Jupiter–Sun problem significantly enhanced the variations in the eccentricities (Wisdom 1983, 1987).

We are interested in studying changes in the osculating eccentricities and longitudes of pericenter of the orbits caused by passage through the resonance. These changes occur over time scales which are generally much longer than the orbit periods. The major contributions to these changes in the elements are resonant interactions between Ariel and Umbriel involving the slowly varying combination of mean longitudes $5\lambda_U - 3\lambda_A$ and the secular interactions between the satellites. Here and in the following development, the subscript A refers to Ariel and the subscript U to Umbriel.

The secular interactions of the Uranian satellites are relatively strong (Dermott and Nicholson 1986, Laskar 1986). However, the largest contributions to the secular variations of Ariel and Umbriel arise from their mutual interaction. In this first paper we have ignored the secular perturbations due to the other satellites. With this approximation the problem remains a two degree of freedom problem, allowing a detailed study of the complicated dynamics with the surface of section technique.

Near the resonance, the evolution of e_i and $\tilde{\omega}_i$ is dominated by the low frequency perturbations, with frequencies associated with changes in the resonant combination of longitudes $5\lambda_U - 3\lambda_A$ and the longitudes of pericenter $\tilde{\omega}_i$. The high-frequency contributions associated with the motions of λ_A and λ_U, and with other nonresonant combinations of the mean longitudes, are removed in first order by averaging.

As resonance coordinates we have chosen (see Appendix I)

$$\sigma_A = \frac{1}{2}(5\lambda_U - 3\lambda_A - 2\tilde{\omega}_A)$$

$$\sigma_U = \frac{1}{2}(5\lambda_U - 3\lambda_A - 2\tilde{\omega}_U) \qquad (3)$$

which together with λ_A and λ_U form a complete set of generalized coordinates. The momenta conjugate to σ_A and σ_U are, in terms of the Delaunay momenta $L_i \approx m_i\sqrt{GMa_i}$ and $G_i = L_i\sqrt{1 - e_i^2}$ (see Plummer 1960):

$$\Sigma_A = L_A - G_A$$

$$\Sigma_U = L_U - G_U. \qquad (4)$$

This choice of variables results in two integrals of motion, the momenta conjugate to $\gamma_A = \lambda_A$ and $\gamma_U = \lambda_U$, since in the new variables the resonant Hamiltonian is cyclic in these variables. The resonance integrals are

$$\Gamma_A = L_A + \frac{3}{2}(\Sigma_A + \Sigma_U)$$

$$\Gamma_U = L_U - \frac{5}{2}(\Sigma_A + \Sigma_U). \qquad (5)$$

Note that $\Sigma_i \approx \Gamma_i e_i^2/2$. The lowest order resonant terms in the disturbing function which influence the evolution of the eccentricities and pericenter longitudes are of order e_i^2. The lowest order secular terms are also of this order (see Appendix I). The Hamiltonian is now expanded in powers of Σ_i/Γ_i to this order, and constant terms are removed. The resulting expression is

$$\begin{aligned}\mathcal{H} = {} & 2A(\Sigma_A + \Sigma_U) + 4B(\Sigma_A + \Sigma_U)^2 \\ & + 2C\Sigma_A + 2D\Sigma_U \\ & + 2E\sqrt{\Sigma_A\Sigma_U}\cos(\sigma_A - \sigma_U) \\ & + 2F\Sigma_A\cos(2\sigma_A) \\ & + 2G\sqrt{\Sigma_A\Sigma_U}\cos(\sigma_A + \sigma_U) \\ & + 2H\Sigma_U\cos(2\sigma_U). \qquad (6)\end{aligned}$$

Expressions for the coefficients are given in Appendix I. For low eccentricities, the coefficient $A \approx \frac{1}{4}(5n_U - 3n_A)$. Near the 5:3 mean-motion resonance, this quantity is near zero. Tidal dissipation in the planet causes the orbits of the satellites to expand differentially (Goldreich 1965). Because of this differential expansion, n_A decreases relative to n_U (see Section 4.1). Therefore, the quantity $(5n_U - 3n_A)$ increases as energy is dissipated in the planet and changes sign when the mean motions are exactly commensurate. This provides a convenient measure of distance from the resonance. We define the parameter $\delta = 4A + 2(C + D)$ to be the resonance parameter in this problem. At small eccentricities it is proportional to the nonresonant contribution to $5n_U - 3n_A - \dot{\tilde{\omega}}_A - \dot{\tilde{\omega}}_U$, and it changes sign in the middle of the resonance region (see Appendix III). The other coefficients are proportional to the semimajor axis ratio as it appears in the Leverrier coefficients (see Appendix I). The change in semimajor axis ratio as the resonance is traversed is of order one part in a thousand, while the fractional change in δ is of order unity. The changes in the numerical values of the coefficients are therefore small compared to the changes in δ and consequently will be neglected.

The transformation to canonical coordinates

$$y_i = \sqrt{2\Sigma_i}\,\sin(\sigma_i) \approx e_i\sqrt{\Gamma_i}\,\sin(\sigma_i) \quad (7)$$

and the conjugate momenta

$$x_i = \sqrt{2\Sigma_i}\,\cos(\sigma_i) \approx e_i\sqrt{\Gamma_i}\,\cos(\sigma_i) \quad (8)$$

is made, resulting in the final form of the Hamiltonian:

$$\begin{aligned}\mathcal{H} = {} & \frac{1}{4}(\delta - 2(C + D))(x_A^2 + y_A^2 + x_U^2 + y_U^2) \\ & + B(x_A^2 + y_A^2 + x_U^2 + y_U^2)^2 \\ & + C(x_A^2 + y_A^2) + D(x_U^2 + y_U^2) \\ & + E(x_A x_U + y_A y_U) + F(x_A^2 - y_A^2) \\ & + G(x_A x_U - y_A y_U) + H(x_U^2 - y_U^2).\end{aligned} \quad (9)$$

This Hamiltonian has two degrees of freedom. Note the similarity between this and the Hamiltonian studied by Hénon and Heiles (1964)—essentially a pair of harmonic oscillators with nonlinear coupling. Hénon and Heiles studied a cubic interaction; in this case the nonlinear terms are quartic.

Wisdom (1982, 1983) has derived an algebraic map of phrase space onto itself for the Hamiltonian describing the motion of asteroids near the 3 : 1 Kirkwood gap, analogous to the approach used by Chirikov (1979) for systems with pendulum-like Hamiltonians. This method has had considerable success in predicting the behavior of asteroidal motion near the Jovian mean-motion commensurabilities. In a similar way, the Ariel–Umbriel 5 : 3 resonance problem can be approximated by a mapping (see Appendix II). However, since this problem is not a restricted three-body problem, it requires a different development. The basic principle involves changing the form of the high-frequency terms in the Hamiltonian. These terms are first removed by averaging, and then new high-frequency terms are introduced in such a way that periodic data functions are formed. The resulting equations are "locally integrable" across the delta functions and between them. Integration of the equations of motion now involves only the evaluation of simple functions. The main advantage of the algebraic mapping is speed of computation. Of course, if is difficult to make meaningful comparisons of speed between qualitatively different methods. In practice, though, the mapping makes a MicroVAX competitive with conventional methods used on supercomputers. The gain in this case is approximately a factor of 10 over the *analytically averaged* differential equations with a relative precision of 10^{-9} per time step, which is on the order of one year. The gain over direct integration of unaveraged differential equations would be at least one or two orders of magnitude. One could argue that since the relative precision of the mapping is the full numerical precision of the computer, the real gain in speed of computation is much greater. This gain is significant for long numerical runs involving slow tidal evolution. It is essential that the simulated tidal evolution be slow enough to avoid artifacts (see Section 4.1).

3. RESONANCE DYNAMICS

3.1. Surfaces of Section

In problems such as that considered by Hénon and Heiles the presence of large-scale chaos is difficult to predict with the resonance overlap criterion or other methods. The Hamiltonian (9) is quite similar to the Hénon–Heiles Hamiltonian in this respect; it is a bit too complicated to rely on a simple criterion such as the resonance overlap criterion. In order to securely determine the extent of chaotic behavior, it is necessary to resort to numerical methods. For a system with two degrees of freedom, it is possible to study the structure of phase space using the Poincaré surface of section technique (see Hénon and Heiles 1964). The basic idea of the surface of section is to study the intersections of a trajectory with a two-dimensional plane through the phase space, rather than the full four-dimensional phase space. These intersections reveal the qualitative character of the trajectories, i.e., whether they are chaotic or quasiperiodic. For quasiperiodic trajectories successive intersections will fall on smooth curves; for chaotic trajectories successive intersections appear to fill an area in an irregular manner.

Two sections have been chosen for study in this paper: plotting y_A vs x_A when $x_U = 0$, which we designate section I, and plotting y_U vs x_U when $x_A = 0$, which we designate section II. On these plots, the radial distance from the origin is proportional to eccentricity, and the resonance variables σ_i are polar angles. The choice of these section conditions simplifies the determination of initial conditions on the section.

A point on a section defined by a condition such as $x_i = 0$ does not necessarily correspond to a unique trajectory. It is useful to add further conditions on the section so that this will be the case. For instance, in the Hénon–Heiles (1964) problem, the usual surface of section is to plot p_y versus y whenever $x = 0$. Since the Hénon–Heiles Hamiltonian is quadratic in the momenta, each point on the section corresponds to two possible values of p_x. Points on the section will correspond to unique trajectories if an additional condition, say that p_x be nonnegative, is added. Our problem is more complicated. The Hamiltonian is quartic in the x_i and y_i. Due to the quartic nature of the Hamiltonian, for given values of δ, the energy, and the coordinates on the subspace defining the section, there can be two or four values of y_i conjugate to that x_i for which the section condition $x_i = 0$ has been chosen. It is desirable, therefore, to further constrain the surface of section as belonging to one of four root "families." When there are four roots these families are labeled a, b, c, d in order of decreasing numerical value. When there are only two roots they are labelled a and d in order of decreasing numerical value. As indicated by the nomenclature these two families join continuously the corresponding families in the four root case. Root families a and d will be referred to as the "outer" pair and root families b and c will be referred to as the "inner" pair. The sections for these particular root families will be referred to as Ia, Ib, Ic, Id and IIa, IIb, IIc, and IId.

Inspection of the Hamiltonian (9) allows us to determine regions in the δ-energy parameter space in which these root families may be found. For energies less than zero, only two real roots of the quartic equation exist. This is the outer pair. For energies greater than zero and $\delta > -2(C - D) + 4F$, the inner pair of root families exists for points on both sections near the origin.

For energies greater than

$$E_1 = \begin{cases} 0, & \delta < 2(C - D) + 4H, \\ -(\delta - 2(C - D) - 4H)^2/64B, & \\ & \delta \geq 2(C - D) + 4H, \end{cases} \quad (10)$$

there are no real roots for points at the origin of sections I. The boundary of the energy surface on the section divides it into two separate regions, and σ_A must librate on sections I. In this case libration on the section corresponds to an actual libration of σ_A in the full phase space.

Similarly, for energies greater than

$$E_2 = \begin{cases} 0, & \delta < -2(C - D) + 4F, \\ -(\delta + 2(C - D) - 4F)^2/64B, & \\ & \delta \geq -2(C - D) + 4F, \end{cases} \quad (11)$$

σ_U must librate on sections II and in the full phase space (see Fig. 6). Note that $E_1 > E_2$.

The most interesting dynamical behavior occurs for energies near E_1 and E_2. To more easily display the results of our calculations we introduce the new parameter $\Delta E = \mathscr{E} - E_2$, where $\mathscr{E}$ is the numerical value of the Hamiltonian. ΔE naturally reflects the types of motion possible on sections. For $\Delta E \geq 0$, σ_U must librate; for $\Delta E \geq E_1 - E_2$, both σ_A and σ_U must librate. For $0 > \Delta E \geq -E_2$, the resonance variables may circulate or librate, and there are four root families. For $\Delta E < -E_2$ (equivalently $\mathscr{E} < 0$), there are only two root families, and the resonance variables circulate. This is summarized in Fig. 1. The shaded regions in the upper left corners of each plot are regions of δ, ΔE in which there are no real roots for either subspace, and are therefore forbidden regions.

Far from the resonance, the resonant combination of mean longitudes $5\lambda_U - 3\lambda_A$

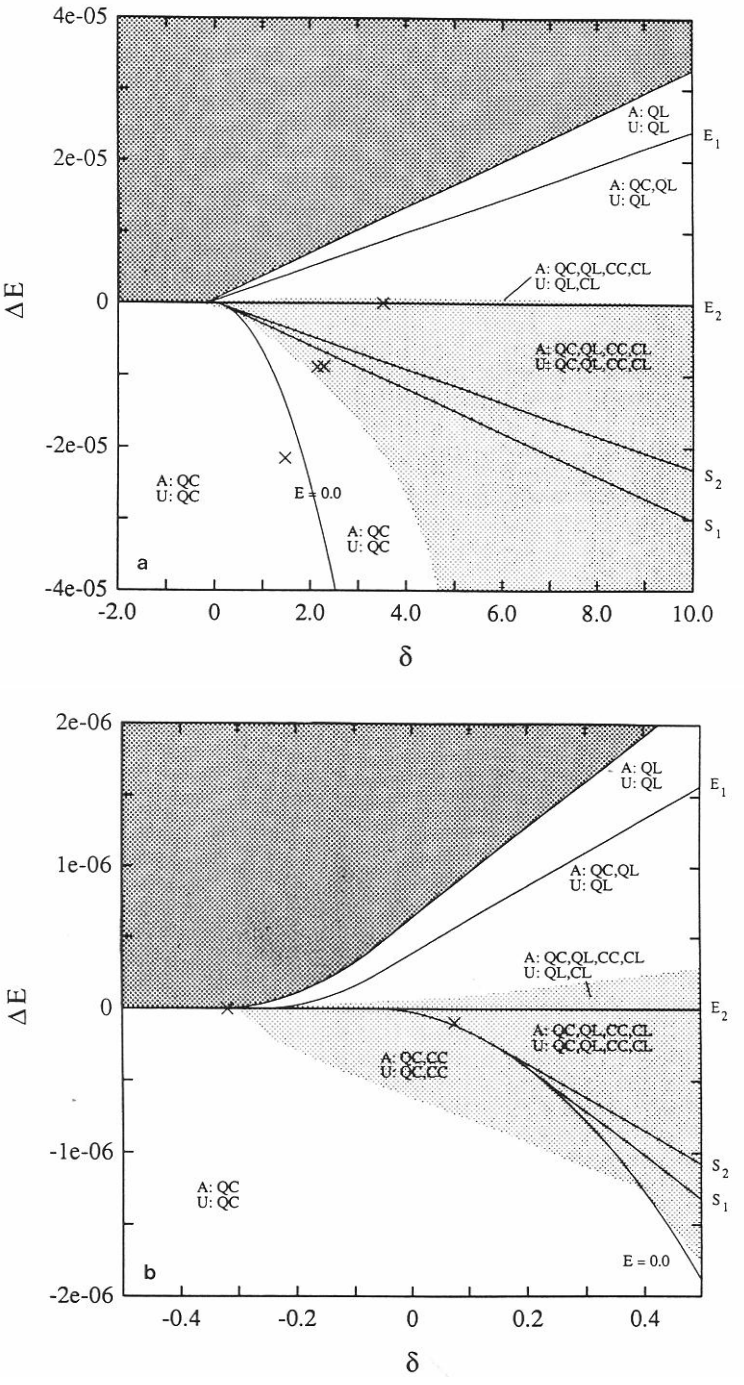

FIG. 1. (a,b) δ, ΔE parameter space at two scales. Crosses indicate parameters of the surfaces of section shown in this paper. Various types of possible motion: QC, quasiperiodic circulation; QL, quasiperiodic libration; CC, chaotic circulation; CL, chaotic libration. S_1 is the energy of the separatrix associated with the Ariel (e_A^2) resonance, and S_2 is the energy of the separatrix associated with the Umbriel (e_U^2) resonance. For energies greater than E_2, σ_U must librate. For energies greater than E_1, both σ_U and σ_A must librate.

circulates rapidly, and the interaction is dominated by the secular interaction. The terms in (6) containing the angles $2\sigma_A$, $2\sigma_U$, and $\sigma_A + \sigma_U$ oscillate rapidly; the angle $\sigma_A - \sigma_U = -(\bar{\omega}_A - \bar{\omega}_U)$ varies slowly. If a canonical transformation to new variables which are the sum and difference of σ_A and σ_U is made, the combination $\Sigma_A + \Sigma_U$ is conjugate to the rapidly circulating sum and is therefore approximately conserved. After removing the high-frequency resonant terms by averaging, the new Hamiltonian becomes

$$\mathcal{H}' = \frac{1}{4}(\delta + 2(C - D))(x_A^2 + y_A^2) + \frac{1}{4}(\delta - 2(C - D))(x_U^2 + y_U^2) + E(x_A x_U + y_A y_U) \quad (12)$$

which is the linear secular Hamiltonian for these two satellites in the resonance coordinates. For a given value of the Hamiltonian, a point on a surface of section defined by $x_i = 0$ can have either of two values of the conjugate coordinate y_i, which may be found by solving a quadratic equation. The points on the section are made to correspond to unique trajectories by specifying which of the two root families is being plotted. These two root families correspond to the outer pair of roots in the more complete resonance problem.

This Hamiltonian can be diagonalized and normal modes found, yielding the standard Lagrange solution of the secular problem (see, e.g., Brouwer and Clemence 1961). The solution is of the form

$$x_i = A_{i1}\cos(\alpha_1 t + \beta_1) + A_{i2}\cos(\alpha_2 t + \beta_2)$$
$$y_i = A_{i1}\sin(\alpha_1 t + \beta_1) + A_{i2}\sin(\alpha_2 t + \beta_2), \quad (13)$$

where α's are the eigenfrequencies.

Periodic orbits are found wherever the amplitude of one of the modes is zero, and the eccentricities are constant. In these cases, the solutions are of the form

$$x_A = A_{Aj}\cos(\alpha_j t + \beta_j)$$
$$y_A = A_{Aj}\sin(\alpha_j t + \beta_j)$$
$$x_U = A_{Uj}\cos(\alpha_j t + \beta_j)$$
$$y_U = A_{Uj}\sin(\alpha_j t + \beta_j). \quad (14)$$

If the section condition is, for instance, $x_U = 0$, then $\alpha_j t + \beta_j = \pi/2$ or $3\pi/2$, and therefore $x_A = 0$ also. There are two fixed points on the section, with $x_A = 0$ and $y_A = \pm A_{Aj}$. The "roots," the values of the coordinate conjugate to the section variable $x_U(=0)$ for the fixed points on the section, are $y_U = \pm A_{Uj}$, one root in family *a* and one root in family *d*. There are two such fixed points associated with the other eigenmode. We therefore expect, that for a given section condition, there are four fixed points on the *y*-axis, two of which belong to root family *a* and two to root family *d*. Thus sections I*a*, I*d*, II*a*, and II*d* each have two fixed points in the linear secular problem.

Representative surfaces of section for the full 5:3 resonance problem before the resonance is encountered are shown in Figs. 2 and 3. Figures 2a and b display sections I*a*, *d*, respectively, and Figs. 3a and b display sections II*a*, *d*, respectively. The same trajectories are plotted on all figures. As expected, on each section there are two fixed points corresponding to each pure mode, each surrounded by concentric invariant curves. Note that the regions dominated by each mode are not periodic islands associated with a resonance phenomenon, and they are not divided by an infinite period separatrix with an unstable equilibrium. The position of a curve on the section depends on the relative strengths of the two eigenmodes. For a particular trajectory points alternately appear on the sections corresponding to the two root families. For instance the points forming the small loop at the top of Fig. 3a and the small loop at the bottom of Fig. 3b were generated by the same trajectory. Similarly, the big loops on Figs. 3a and 3b were generated by the same trajectory. Each section is dominated by one of the modes. The other mode appears

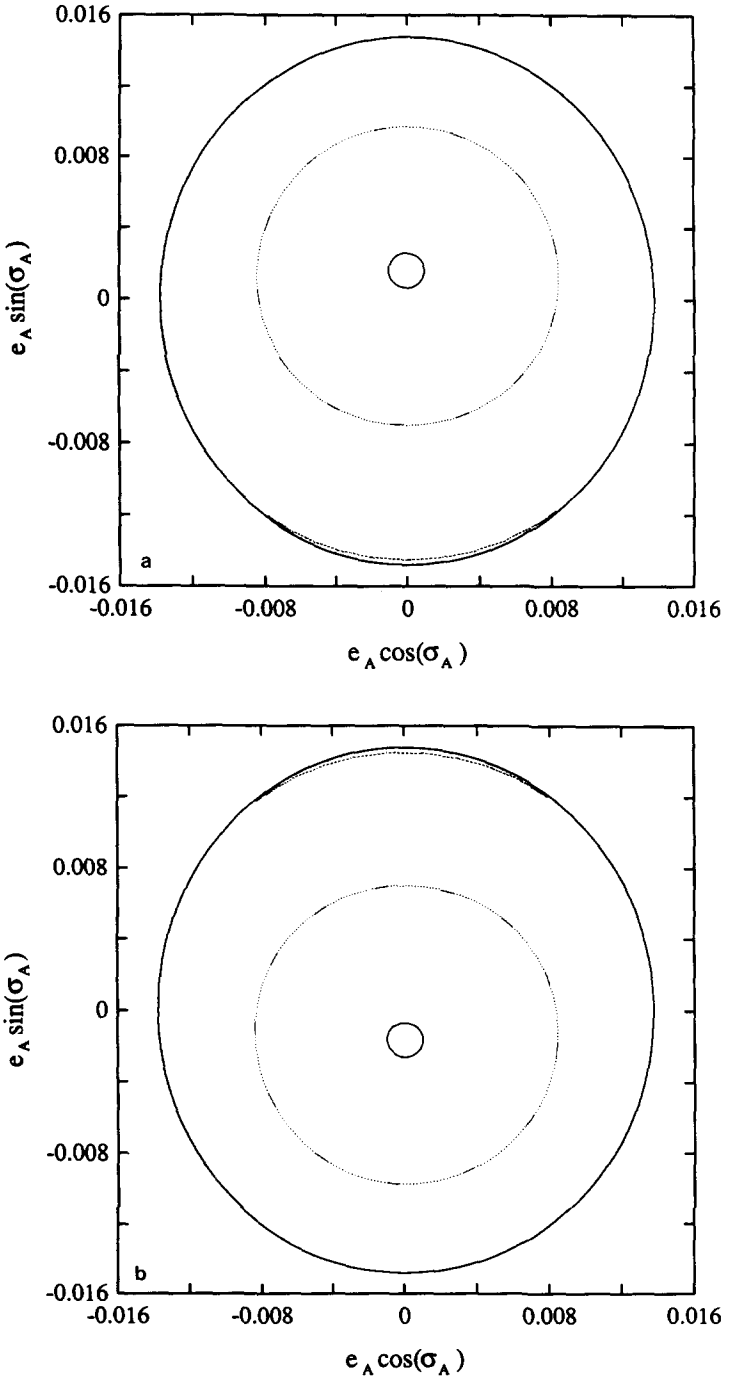

FIG. 2. Surfaces of section showing quasiperiodic secular normal modes, at $\delta = 1.4263$, $\Delta E = -2.1626 \times 10^{-5}$. (a) Section I*a* (largest quartic root family). (b) Section I*d* (smallest quartic root family). The Mode I fixed point occupies the central region of both figures. The Mode II fixed point occupies the small regions close to the energy surface boundary, near the bottom of section I*a* and near the top of section I*d*.

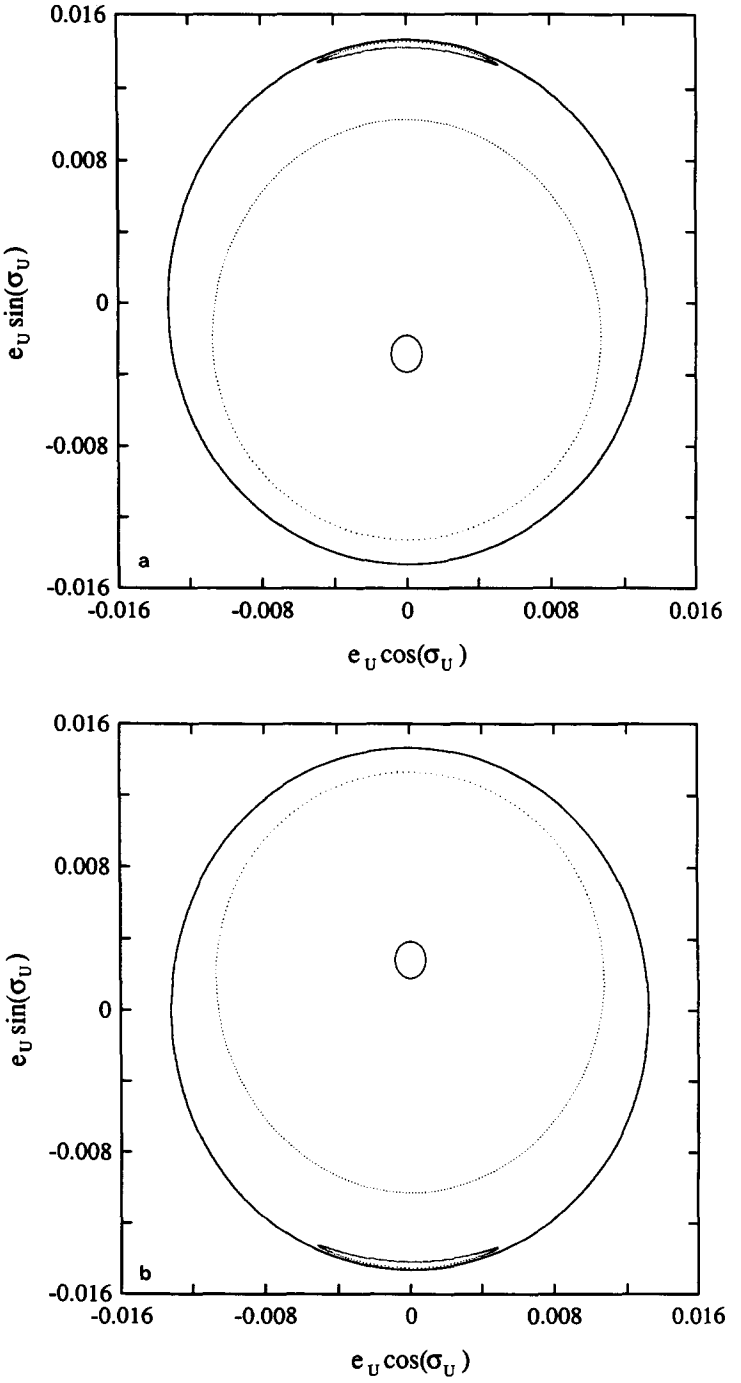

FIG. 3. Surfaces of section showing quasiperiodic secular normal modes, at $\delta = 1.4263$, $\Delta E = -2.1626 \times 10^{-5}$. (a) Section II*a* (largest quartic root family). (b) Section II*d* (smallest quartic root family). The curves shown in these figures are generated by the same trajectories as generated the curves in Fig. 2. The Mode II fixed point occupies the central region of both figures. The Mode I fixed point occupies the small regions close to the energy surface boundary, near the top of section I*a* and near the bottom of section I*d*.

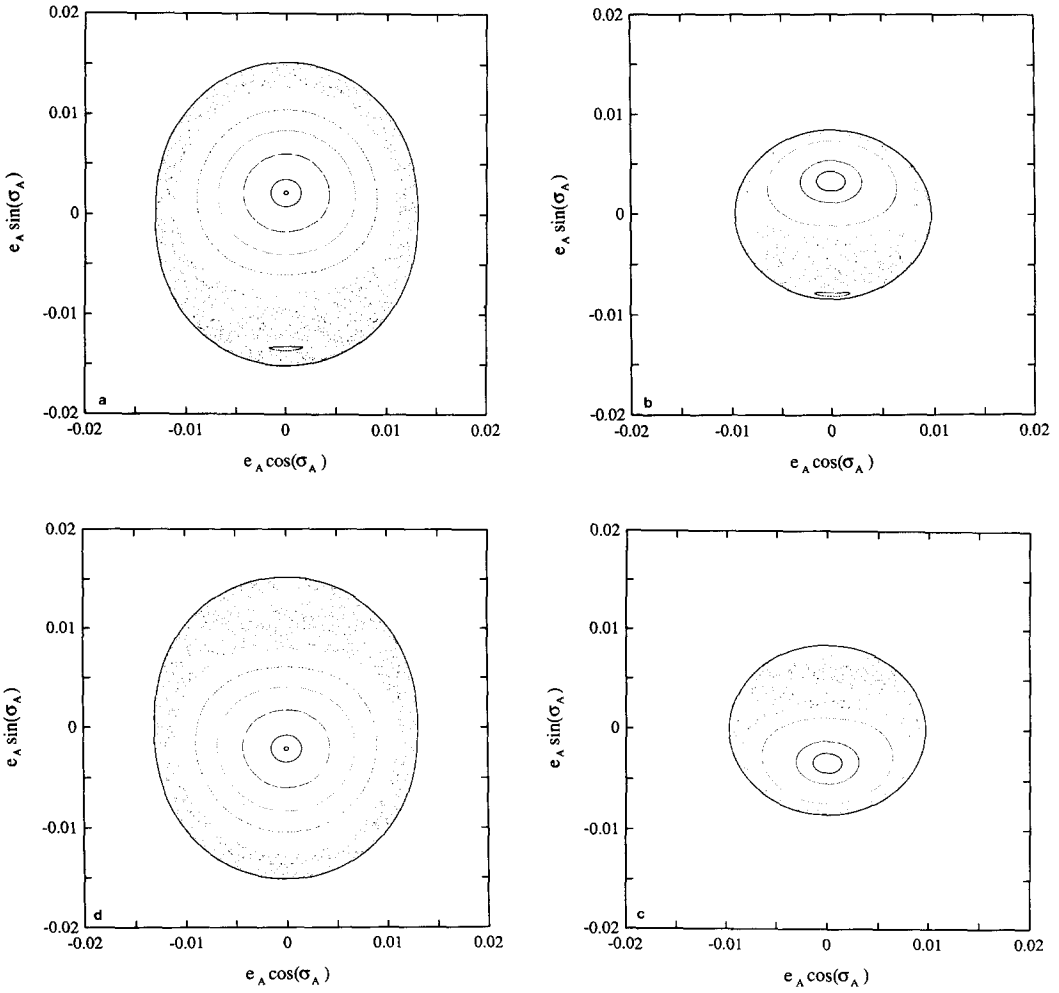

FIG. 4. Sections I in the region of parameter of space in which large-scale chaotic behavior is possible, at $\delta = 2.258$, $\Delta E = -8.78 \times 10^{-6}$. Quartic root families are ordered (a)–(d) according to numerical value. Much of the region surrounding the Model II fixed point on sections I*a* and I*d* in Fig. 2 has become chaotic. Escape from the resonance occurs in the large quasiperiodic zone in roots (b) and (c). The fixed point of this large quasiperiodic region becomes Mode I far from the resonance. The small quasiperiodic curve near the bottom of section I*a* and the small quasiperiodic curve near the bottom of section I*b* are generated by a trajectory for which σ_A librates.

on the sections near the boundary of the energy surface. Note that even though the resonance angle σ_i may not encircle the origin on the section for a particular trajectory, the resonance variable is not librating. The apparent libration on the section is simply a matter of one resonance variable being strobed by the other. We designate the mode dominating sections I as Mode I, and that dominating sections II as Mode II.

The surfaces of section in Figs. 4 and 5 show more interesting behavior. The same trajectories on both sections I*a–d* (Fig. 4) and sections II*a–d* (Fig. 5) are shown. For these parameters all four root families exist. All sections for all root families continue to show the bimodal structure, but now the modes are separated by a large chaotic region. The fixed point at the center of the large quasiperiodic island on sec-

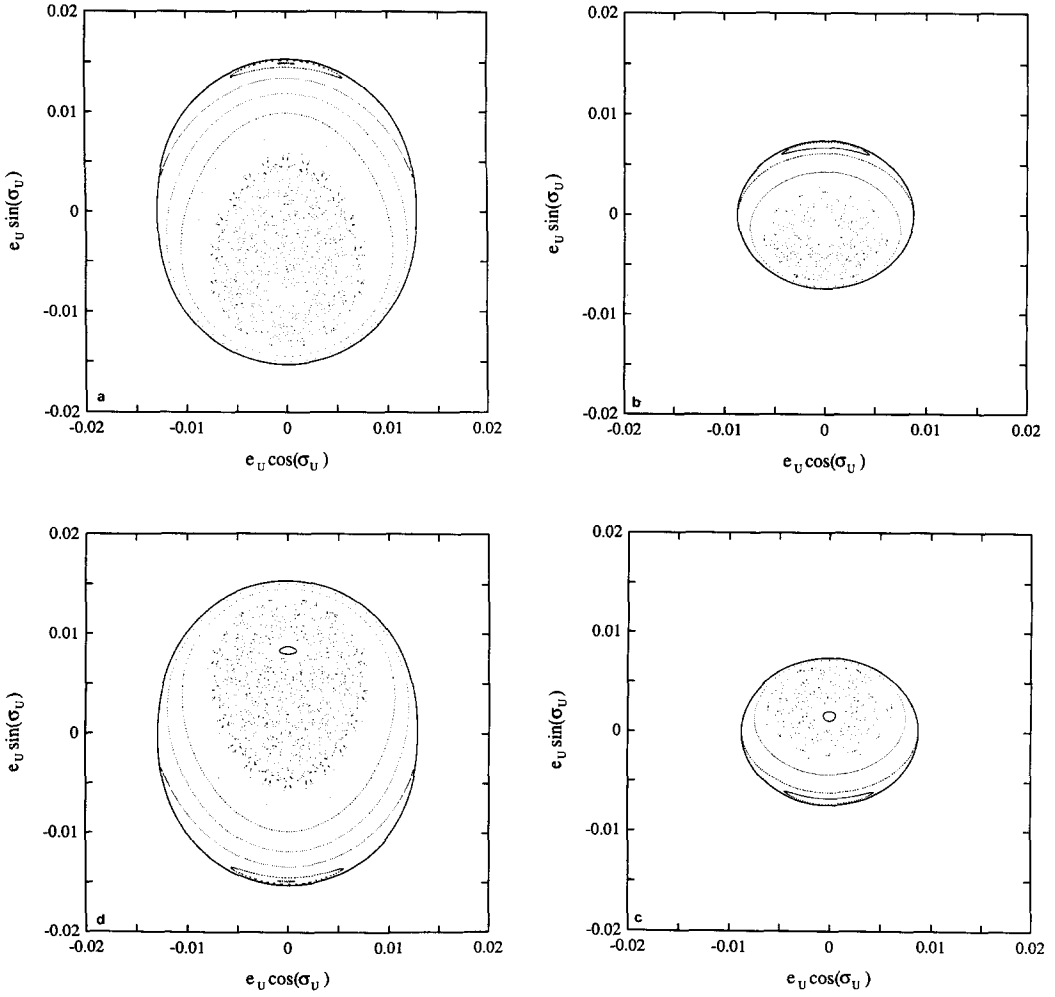

FIG. 5. Sections II in the region of parameter space in which large-scale chaotic behavior is possible, at $\delta = 2.258$, $\Delta E = -8.78 \times 10^{-6}$. Quartic root families are ordered (a)–(d) according to numerical value. The curves shown in these figures are generated by the same trajectories as generated the curves in Fig. 4. Escape from the resonance occurs in the large quasiperiodic zone in roots (b) and (c). The small quasiperiodic curves in the midst of the chaotic zone on sections II*c* and II*d* are generated by the same trajectory that generates the small quasiperiodic curves in Figs. 4a and 4b, for which σ_A librates.

tions I*a* and I*d* is part of a continuous family of periodic orbits which becomes Mode I far inside the resonance region ($\delta \ll 0$). Similarly, the fixed point at the center of the large quasiperiodic island on sections I*b* and I*c* is part of a continuous family of periodic orbits which becomes Mode I far outside the resonance region ($\delta \gg 0$). The quasiperiodic zone surrounding these latter islands is the region of phase space into which trajectories escape from the resonance. We continue then to refer to the islands surrounding these fixed points as Mode I. Trajectories in Mode I on sections I*a* and I*d* alternately visit each of these sections. In a similar manner, Mode I trajectories on sections I*b* and I*c* alternately visit each of the sections. No Mode I trajectory generates points on all the sections corresponding to all four root families. For cha-

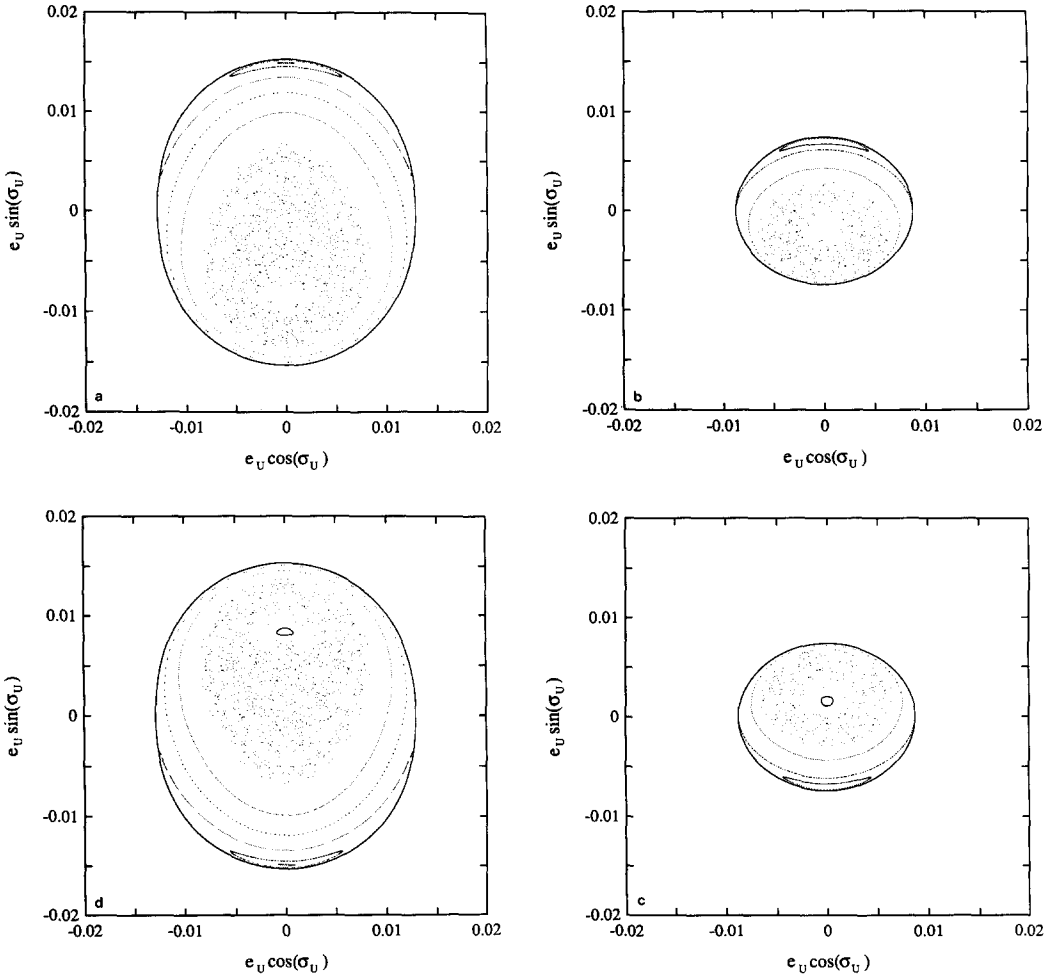

FIG. 6. Sections II in the region of parameter space in which large-scale chaotic behavior is possible, at $\delta = 2.258$, $\Delta E = -8.78 \times 10^{-6}$, computed using *differential equations* for the averaged planar Hamiltonian. Quartic root families are ordered (a)–(d) according to decreasing numerical value. The curves shown in these figures have the same initial coordinates at the curves in Fig. 5.

otic trajectories successive points appear on the sections corresponding to all four root families in a typically chaotic manner. The small islands in the lower parts of Figs. 4a and 4b (sections I*a* and I*b*) are alternately visited by the trajectories which generate them. The periodic orbits at the center of these islands are associated with Mode II, but in a more complicated way than was the case for Mode I (see next section). A similar part of small islands exists on sections I*c* and I*d*, but trajectories belonging to these islands were not computed on the figure. Trajectories on these small islands librate in σ_A and may librate in σ_U. Mode I trajectories do not librate. The surfaces of section in Fig. 5 show the same features as in Fig. 4, but in Umbriel variables (sections II). The large features in Fig. 5 were generated by the same trajectories as generated the large features in Fig. 4. The small islands in both Figs. 4 and 5 were generated by the same trajectories.

The surfaces of section in Fig. 6 show the same trajectories as in Fig. 5, but this time computed using the averaged Hamiltonian

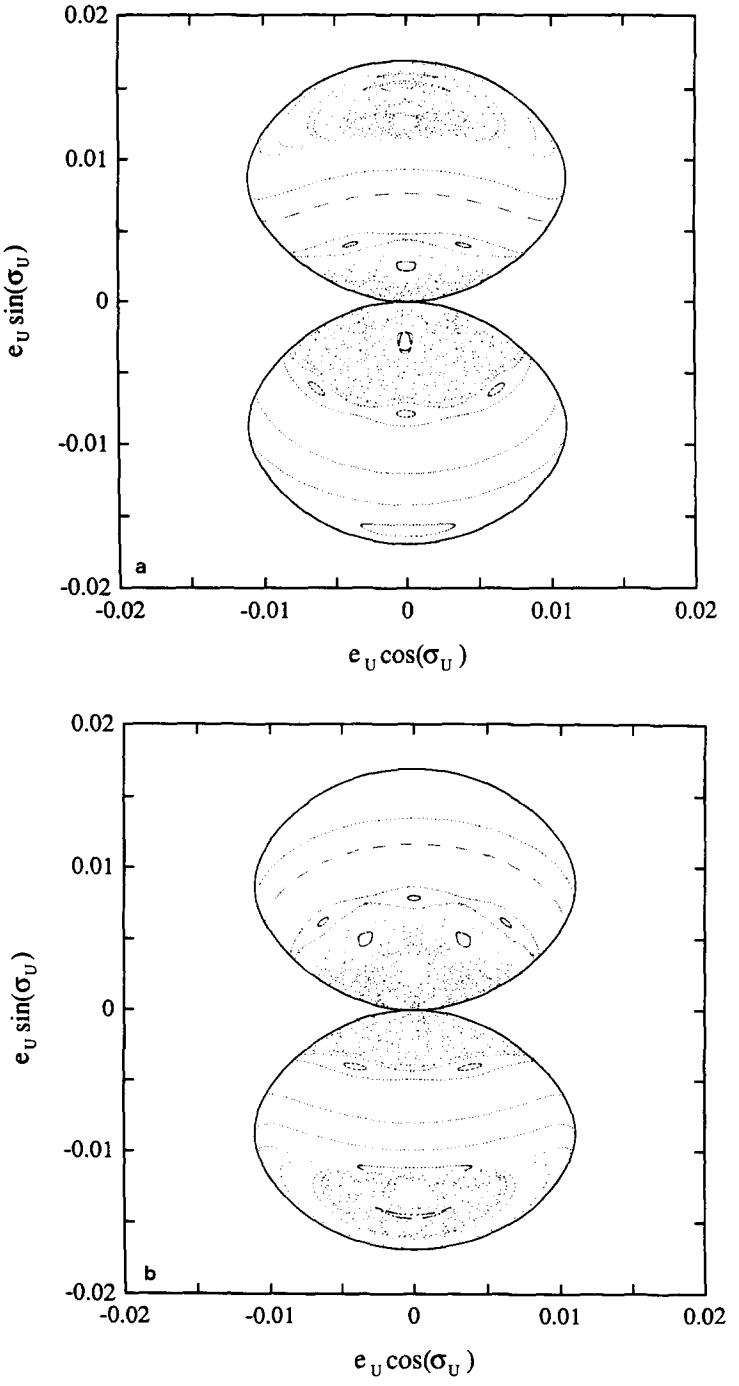

FIG. 7. Sections II at $\delta = 3.5$, $\Delta E = 0$, on the boundary in parameter space above which capture into the resonance occurs. (a) Section II*a* (larges quartic root family). (b) Section II*d* (smallest quartic root family). σ_U librates in the full phase space for all trajectories on these plots. All trajectories shown, even chaotic trajectories, have been captured into the resonance.

(9) with a relative precision of 10^{-9} per time step. The correspondence between trajectories in excellent, indicating that the mapping represents the Hamiltonian (9) well. The slight difference in appearance of the chaotic zone is expected, since using a different integrator is equivalent to beginning with a slightly different initial set of coordinates. In a chaotic region, two trajectories with slightly different initial coordinates diverge exponentially with time. While the detailed evolution within the chaotic zone will differ, the qualitative behavior is the same. In the long run the same region of phase space will be filled.

The surface of section in Fig. 7 is at $\Delta E = 0$, computed with the mapping. The energy surface has split the section into two independent regions, and σ_U librates for trajectories in each region, independently of the quasiperiodic or chaotic character of the trajectory. The libration is forced by the topology of the energy surface. Successive appearances of points on the section are confined to one region or the other. At still higher ΔE, the two regions move apart, and the large chaotic zone disappears. The forced libration of chaotic trajectories is a new feature of this problem. More usually, the chaotic zone occurs at the boundary between libration and circulation, and thus a chaotic trajectory alternately librates and circulates. This new feature provides a new mechanism for capture into resonance. *Trajectories may be captured into resonance while they are still chaotic.*

Figure 8 shows results of a computation of the maximum Lyapunov characteristic exponent λ (see, e.g., Bennettin *et al.* 1976). The Lyapunov characteristic exponent provides a measure of the exponential divergence of trajectories in chaotic zones. Trajectories from two different regions of parameter space have been represented: one in the large chaotic zone shown in Figs. 4–6 and one in the large chaotic zone in the librating region shown in the lower half of Fig. 7. In both cases, λ approaches a value

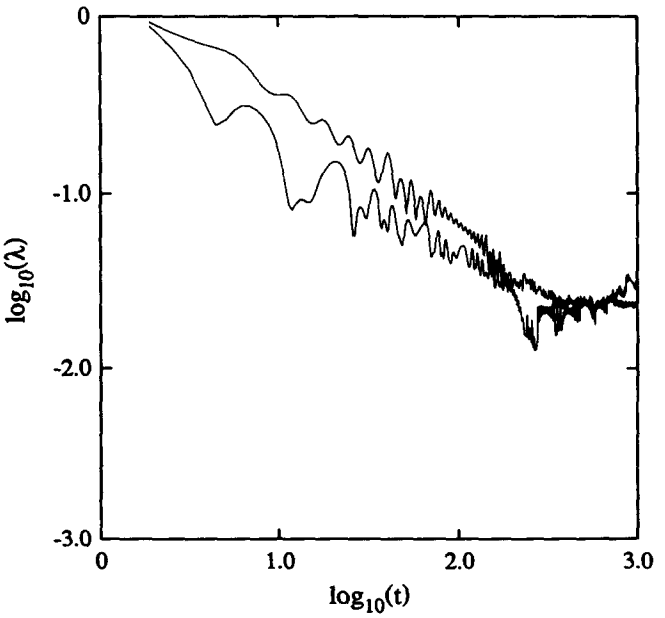

FIG. 8. Maximum Lyapunov characteristic exponents for trajectories in the chaotic zones in the previous figures. The unit of time is one year. The upper curve at low t was computed for a trajectory in the chaotic zone in the lower libration region shown in Fig. 7, and the lower curve at low t was computed for a trajectory in the chaotic zone in Figs. 4 and 5.

≈ 0.03 year^{-1}. This corresponds to an e-folding time for the distance function of about 30 years, which is comparable to the secular evolution time scale.

3.2. *Onset of Chaos*

The lightly shaded regions in the lower right of Fig. 1 show the parameter regions where "macroscopic" chaotic zones are accessible some place on the surface of section. The extent of the region was determined by evaluating the rate of growth of distance between two nearby trajectories for 20 initial conditions evenly spaced along the y-axis between the energy boundary limits on Sections II for a given δ and ΔE—if one of these was found to indicate chaos, the section is considered to have a "macroscopic" chaotic zone. Note that the two single resonance separatrix energies, denoted S_1 and S_2, run through the middle of the chaotic zone (see Appendix III).

The onset of large-scale chaos is associated with an instability of the Mode II fixed point. A tidally evolving system with increasing δ will encounter the region in δ–ΔE parameter space in which large-scale chaos is present on the surfaces of section from the lower left of Fig. 1. Near the boundary of this region of large-scale chaos the fixed point of Mode II goes through two period-3 bifurcations (see, e.g., Meyer 1970, Hénon 1970). These bifurcations are associated with a 3:1 resonance between the degrees of freedom in the problem. After these bifurcations the nature of the fixed points has changed, with the result that σ_A librates in the small quasiperiodic island surrounding the Mode II fixed point. Before the bifurcations σ_A circulated in Mode II.

Figure 9 illustrates these bifurcations on section IIb. The changes in δ and ΔE in the series 9a–9e simulate possible variations during tidal evolution (see next Section). These surfaces of section therefore illustrate the changes in the structure of the phase space available to a trajectory as it crosses the boundary. Successive appearances of points on the section near the Mode II stable fixed point before the bifurcation (Fig. 9a) alternate between sections IIb and IIc, and σ_A and σ_U circulate. As the parameters evolve toward larger δ and ΔE, the region of stability near the Mode II fixed point shrinks, the extent of the chaotic zone in phase space increases, and eventually the Mode II fixed point becomes unstable (Fig. 9b). After the first bifurcation, a stable island appears around the fixed point (Fig. 9c), but now the points alternate between sections IIa and IIb. σ_A librates for trajectories within these islands. A second period-3 bifurcation occurs (Figs. 9d–9e). Note that the orientation of the roughly triangular trajectory surrounding the stable fixed point has inverted, a characteristic feature of this type of bifurcation (see, e.g., Hénon 1966a,b, 1969, 1970). Again, the points alternate between sections IIa and IIb, and σ_A librates. The trajectories generating these islands librate in σ_A and, as tidal evolution continues, eventually in σ_U around $\pi/2$ or $3\pi/2$. (A similar pair of islands appears on sections IIc and IId.) Note that throughout the sequence of Figs. 8a–8e the region surrounding the Mode I fixed point remains stable.

Another qualitative change in phase space concerns the accessibility of the root families. Before the bifurcation, trajectories generate points alternately on the sections corresponding to the "outer" pair of root families (a and d) or the "inner" pair (b and c). As the first bifurcation occurs, the large chaotic zone appears around the fixed point on the section corresponding to the periodic orbit associated with Mode II, which has become unstable. Successive points generated by a chaotic trajectory appear on the sections corresponding to all four root families. Therefore, the appearance of the chaotic zone supplies a dynamical mechanism by which trajectories which generate points on sections corresponding to one pair of root families gain access to the sections corresponding to the other pair of root families. This is important in the mechanism of escape from the resonance, as seen in the next Section.

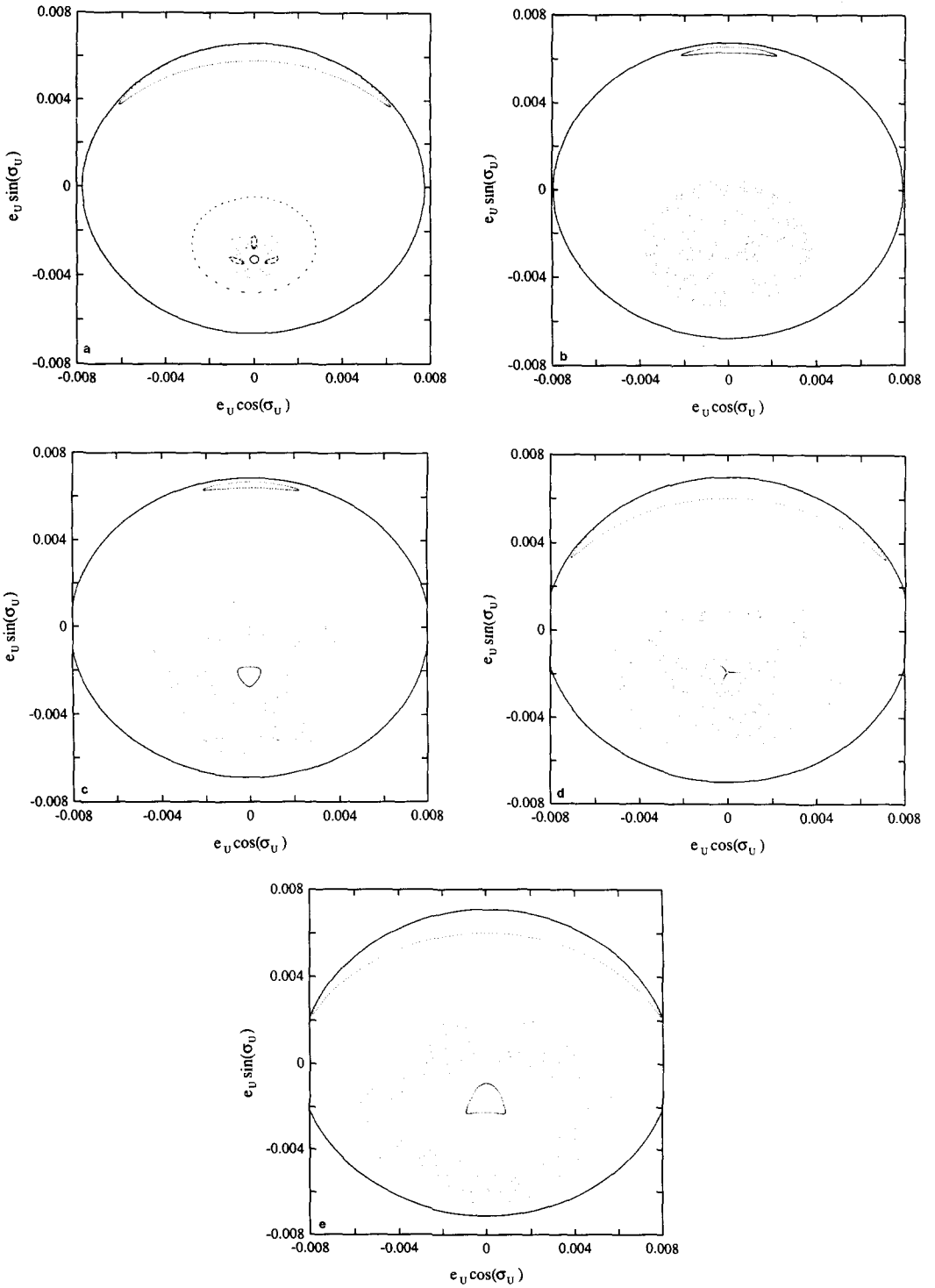

FIG. 9. Period-3 bifurcation on section II*b*. (a) $\delta = 2.066$, $\Delta E = -9.34 \times 10^{-6}$; (b) $\delta = 2.09$, $\Delta E = -9.1 \times 10^{-6}$; (c) $\delta = 2.11$, $\Delta E = -8.9 \times 10^{-6}$; (d) $\delta = 2.13$, $\Delta E = -8.7 \times 10^{-6}$; (e) $\delta = 2.15$, $\Delta E = -8.5 \times 10^{-6}$. This corresponds to a 3 : 1 resonance between the degrees of freedom.

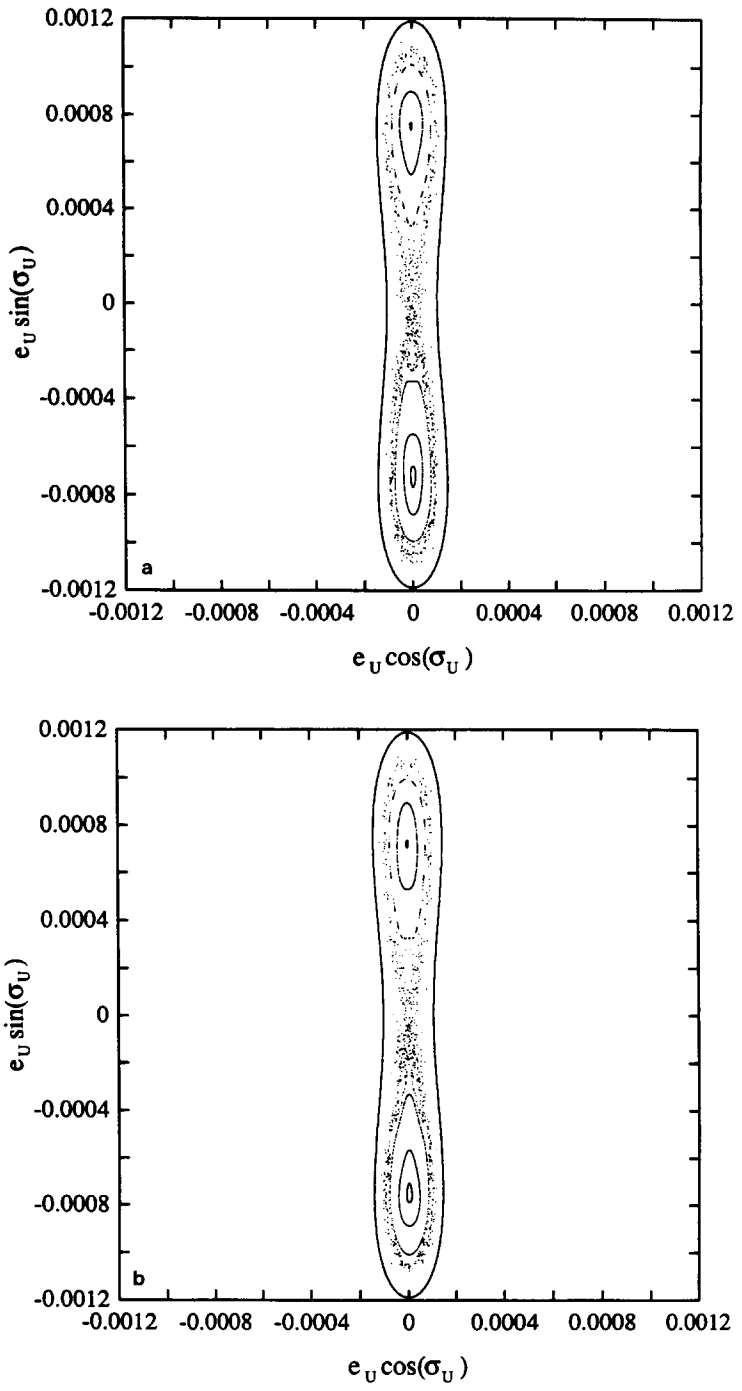

FIG. 10. Sections II for low eccentricities, $\delta = -0.32$, $\Delta E = -1.0 \times 10^{-9}$. (a) Section II*a* (largest quartic root family). (b) Section II*d* (smallest quartic root family). The chaotic zone is characteristic of a perturbed separatrix.

For very low eccentricities, the coupling between resonances is weakened, and one might expect to observe behavior characteristic of a perturbed single resonance problem. Figure 10 illustrates this for values of δ and ΔE near those where the Umbriel resonance is first encountered in the single resonance approximation (see Appendix III). There is a relatively narrow chaotic zone with the characteristic "figure 8" shape of the separatrix in the single resonance case.

4. EVOLUTION THROUGH THE RESONANCE

4.1. Tidal Dissipation

The results of the previous section illustrate the behavior of the Hamiltonian (9) for fixed values of the parameters δ and ΔE. This section discusses the tidal evolution through the resonance. Tidal friction enters in two distinct ways. The principal modification of the model is that the coefficients of the Hamiltonian become time dependent. This is primarily due to the differential tidal expansion of the orbits. There is also the direct action of tidal friction in the satellites on the degrees of freedom. Thus tidal friction gives rise to time-dependent coefficients as well as explicit friction terms in the equations of motion.

Of the various coefficients in the resonance Hamiltonian, only δ depends strongly on the resonant combination of mean motions; during passage through the resonance, the fractional change in the parameter δ is large compared to the fractional changes in the other coefficients. The other coefficients will therefore be taken to be constant. In addition, the value of δ is influenced by the damping of eccentricities due to tidal dissipation in the satellites. The time rate of change of δ is

$$\dot{\delta} = 4\dot{A}. \tag{15}$$

From the expansion of A to first order in Σ_i

$$\begin{aligned}\dot{\delta} &\simeq \frac{d}{dt}\left[(5n_{\mathrm{U}} - 3n_{\mathrm{A}}) - 16B(\Sigma_{\mathrm{A}} + \Sigma_{\mathrm{U}})\right] \\ &= (5\dot{n}_{\mathrm{U}} - 3\dot{n}_{\mathrm{A}}) - 16B(\dot{\Sigma}_{\mathrm{A}} + \dot{\Sigma}_{\mathrm{U}}),\end{aligned} \tag{16}$$

where

$$\dot{\Sigma}_i \simeq \Sigma_i\left[-\frac{1}{3}\frac{\dot{n}_i}{n_i} + 2\frac{\dot{e}_i}{e_i}\right]. \tag{17}$$

Tidal friction results in a secular variation of the mean motions (e.g., Goldreich 1965)

$$\dot{n}_i = -\frac{9}{2}k_2 n_i^2 \frac{m_i}{M}\left(\frac{R}{a_i}\right)^5 \frac{1}{Q} \tag{18}$$

and a damping of the orbital eccentricities (Goldreich 1963)

$$\begin{aligned}\dot{e}_i = &-\frac{21}{2}k_{2i}n_i\frac{M}{m_i}\left(\frac{R}{a_i}\right)^5\frac{e_i}{Q_i} \\ &+\frac{57}{8}k_2 n_i\frac{m_i}{M}\left(\frac{R_i}{a_i}\right)^5\frac{e_i}{Q},\end{aligned} \tag{19}$$

where k_2 *and* Q are, respectively, the potential Love number and specific dissipation function for Uranus, and the k_{2i}'s and Q_i's are the same quantities for the satellites. The first term in the expression for $\dot{e}_i$ is the contribution due to tidal dissipation in the satellite, and the second term is due to tidal dissipation in the planet. The contribution due to tidal dissipation in the satellites dominates the contribution due to tidal dissipation in the planet by approximately a factor of 100. Using numerical values from Table I with $Q = 6600$ to evaluate relative contributions to $\dot{\delta}$,

$$\frac{5\dot{n}_{\mathrm{U}}}{3\dot{n}_{\mathrm{A}}} \simeq \frac{5m_{\mathrm{U}}}{3m_{\mathrm{A}}}\left(\frac{a_{\mathrm{A}}}{a_{\mathrm{U}}}\right)^8 \approx 0.1 \tag{20}$$

so the orbit of Ariel expands relative to that of Umbriel. The ratio of the eccentricity dependent terms is

$$\frac{\dot{\Sigma}_{\mathrm{U}}}{\dot{\Sigma}_{\mathrm{A}}} \approx 0.1\frac{e_{\mathrm{U}}}{e_{\mathrm{A}}}. \tag{21}$$

The most significant terms in (16) are therefore

$$\dot{\delta} = -3\dot{n}_{\mathrm{A}} - 16B\dot{\Sigma}_{\mathrm{A}} \tag{22}$$

and the relative contributions from these terms are expressed

$$\frac{16B\dot{\Sigma}_{\mathrm{A}}}{3\dot{n}_{\mathrm{A}}} \approx -1.5 \times 10^3 e_{\mathrm{A}}^2. \tag{23}$$

For the current eccentricity of Ariel, the above expression ≈ -0.004, so the $\dot{n}_A$ term is clearly dominant in the expression for $\dot{\delta}$. The $\dot{\Sigma}_A$ term becomes comparable to the $\dot{n}_A$ term only for eccentricities of approximately 0.025. Since we are studying the evolution for systems with initial eccentricities much less than this, we have only retained the $\dot{n}_A$ term in the expression for $\dot{\delta}$. However, if large increases in the eccentricity result from resonant interactions between the satellites, this approximation will require some reconsideration. In our approximation, the expression for $\dot{\delta}$ is

$$\dot{\delta} \simeq \frac{9G^2M^2m_A^3}{2\Gamma_A^3}\frac{\dot{a}_A}{a_A}. \qquad (24)$$

Tidal friction also introduces explicit frictional terms into the equations of motion. The most important frictional terms arise from the damping of the orbital eccentricities from dissipation within the satellites. From Eq. (19), with rigidities $\mu_A = \mu_U \approx 10^{11}$ dynes/cm^2 (see Table I), the eccentricity damping time scale for Ariel is about $1.5 \times 10^6 Q_A$ years, and that for Umbriel is about $1.4 \times 10^7 Q_U$ years. For $Q_A \approx Q_U \approx 100$, these time scales are on the order of 10^8 and 10^9 years, respectively. Whether $\dot{e}_i$ is important in our study depends on the time scale of resonance passage compared to the eccentricity damping time scale. The time scale of resonance passage depends in turn on the rate of orbital evolution, which is determined by the specific dissipation function Q of Uranus, as discussed below.

The value of Q can be constrained by considering reasonable scenarios for the orbital evolution of the satellites of Uranus (Peale 1988). The rate at which the system evolves is inversely proportional to Q. By extrapolating the evolution backward in time, and eliminating unreasonable configurations of the satellites from the present to the time of formation of the Solar System, it is possible to find upper and lower limits to the possible values Q can take. A lower limit $Q \approx 6600$ places Miranda and Ariel at the same distance from Uranus at the time of formation of the Solar System. This study is only relevant if the Q of Uranus is less than about 100,000, since this Q places Ariel and Umbriel at the 5:3 resonance at the time of formation of the Solar System. Higher values of Q are possible, but then Ariel and Umbriel would never have encountered the 5:3 resonance.

Whether or not $\dot{e}_i$ is important depends on Q. The maximum time of resonance passage would occur for the maximum $Q = 100{,}000$. We have assumed that during the passage through resonance δ varies linearly with time due to the decrease of n_A. The change in δ during resonance passage is of order 1–3 year^{-1}. This indicates that the maximum time of resonance passage is less than approximately 3.1×10^8 years. As discussed above, the tidal damping time scales of the satellites are approximately 10^8 years for Ariel and 10^9 years for Umbriel. These time scales are comparable to the maximum time of resonance passage. For the maximum value of Q, then, direct tidal damping of eccentricities will be important. The rate of evolution is inversely proportional to the value of Q assumed for Uranus. Therefore, for values of Q near the minimum allowed Q, the time scale of resonance passage will be much shorter (less than $\approx 10^7$ years), and damping of eccentricities should have a much smaller effect on the dynamics of the system. The direct tidal damping of e_i could be important, but we neglect it in this initial study.

The principal effect of tidal friction is that the parameter δ varies secularly. The rate of secular variation of δ depends primarily on the unknown value of the Q of Uranus (see Eqs. (18)–(24)).

The numerical study of this system is constrained by finite computer resources. Unfortunately, even the lower limit of Q discussed above requires enormous expenditures of computer time to make a satisfactory study of the evolution of trajectories, even with the algebraic mapping. It is necessary, therefore, to artificially increase the rate of tidal evolution of the system above

the maximum limit imposed by the dynamics of the Uranian satellite system. In the single, integrable resonance model of passage through resonance the outcome of the resonance encounter does not depend on the rate of passage through the resonance as long as the passage is sufficiently slow. The single resonance formulas only require that the fractional change in the libration frequency over a libration period be much less than unity. For the problem under consideration here, where the dynamics and mechanism of passage through resonance are different than those of the single resonance theory, it is no longer clear that the outcome of resonance passage will become independent of the rate of passage for sufficiently slow passage. It is however plausible that this should be the case, whenever the time scale for resonance passage becomes much greater than all dynamical time scales. In any case, in numerical studies of passage through complicated resonances it is not satisfactory to simply choose an arbitrary rate of passage through resonance and hope that it is adequately slow. The burden of showing that the results of numerical experiments of passage through resonance reflect the true dynamics rests with the experimenter. As we illustrate below, the rate of passage through the 5:3 Ariel–Umbriel resonance must be extremely slow in order to avoid artifacts.

We parameterize the rate of evolution in our numerical model by the effective specific dissipation function of Uranus. We designate this effective specific dissipation function by the script $\mathcal{Q}$, in order to emphasize that it is the parameter in our numerical model and not the physical Q of Uranus. With limited computer resources we must increase the rate of evolution determined by $\mathcal{Q}$ as much as possible without affecting the outcome of the resonance passage. In order to draw conclusions about the physical system we must show that the dynamics of passage through resonance become independent of $\mathcal{Q}$ for sufficiently large $\mathcal{Q}$.

To illustrate the effect of $\mathcal{Q}$ on the dynamics of the full resonant problem, Fig. 11

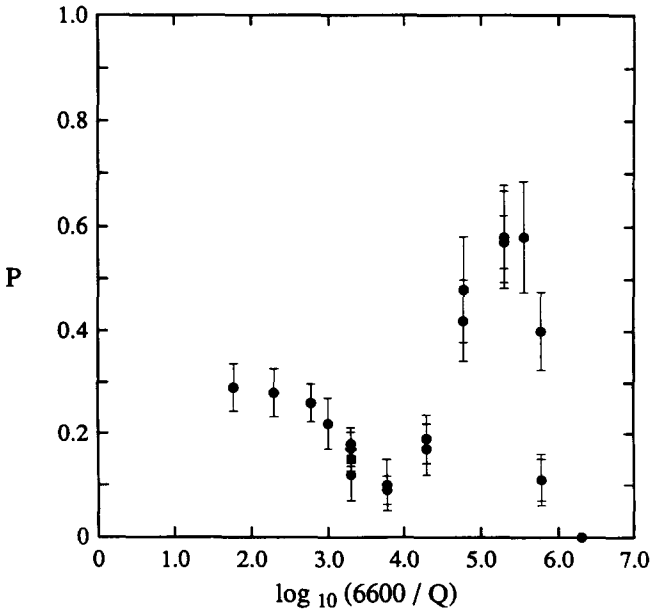

FIG. 11. Measured probability of escape versus tidal dissipation rate for the full resonance problem, in terms of the effective specific dissipation function of Uranus $\mathcal{Q}$. Circles, $\Omega = 20$ year^{-1}; diamond, $\Omega = 80$ year^{-1}; square, differential equations for analytically averaged Hamiltonian.

displays the probability of escape from the resonance against dissipation rate. The probability of escape was determined by integrating sets of 100 trajectories through the resonance with different dissipation rates (see Section 4.2 for more details). The rate of dissipation increases to the right in the figure, and the value of Q decreases. The minimum physically reasonable value of $Q = 6600$ corresponds to the minimum dissipation rate shown. The choice of $\mathfrak{Q}$ apparently can have a significant effect on the results: there is a dependence of escape probability on rate, especially for high dissipation rates (small $\mathfrak{Q}$). Most of the runs described in this paper have used $\mathfrak{Q} = 110$, or 60 times the minimum physical dissipation rate. This is the minimum dissipation rate for which a data point is shown in Fig. 11. This value of $\mathfrak{Q}$ corresponds to $\dot{a}_A/a_A \simeq 1.4 \times 10^{-11}$ per orbit period during passage through the resonance. For somewhat larger dissipation rates, the measured escape probability is similar to that for $\mathfrak{Q} = 110$, indicating that changes in $\mathfrak{Q}$ near this value do not greatly affect the dynamics. It is plausible that the numerical experiments at this $\mathfrak{Q}$ reflect the dynamics at the physical Q. Limitations on available computer time have not allowed us to further verify this numerically. However, trajectories evolved through the resonance with $\mathfrak{Q} = 3300$ do show features similar to these with $\mathfrak{Q} = 110$ (see next section). As a further check of the mapping, we have computed runs with a higher mapping frequency $\Omega = 80$ year^{-1} (diamond in Fig. 11) and with differential equations of the averaged Hamiltonian with a relative precision of 10^{-9} per time step (square) at $\mathfrak{Q} = 6.6$. These have similar escape probabilities to those runs with $\Omega = 20$ year^{-1} (circles in Fig. 11).

Figure 11 emphasizes that for much higher dissipation rates, the dynamics are strongly affected by the choice of $\mathfrak{Q}$. It is apparent that a run with $\mathfrak{Q} = 3.3$, or $\dot{a}_A/a_A \simeq 4.8 \times 10^{-10}$ per orbit period, will produce results significantly different from the physical system, i.e., there are significant artifacts. This is even more evident when the energy evolution of the trajectories is compared: the trajectories in Fig. 12 have the same initial conditions as those in Fig. 15 (see next subsection), but the dissipation rate is 1000 times higher ($\dot{a}_A a_A \simeq 1.4 \times 10^{-8}$ per orbit period). The faster evolution gives a more exciting picture of the evolution through resonance, with large increases in eccentricity, but *it is wrong*.

4.2. Numerical Runs

Figures 13 through 17 show results of numerical runs in which, for each of five initial values of δ and ΔE, 100 trajectories were evolved through the resonance using the mapping (see Appendix II) with slow tidal evolution ($\mathfrak{Q} = 110$). The initial values of δ and ΔE, and the physical parameters corresponding to these values, are given in Table II. The 100 initial points for Run 3 were on an invariant curve of sections II. For the other runs each set of 100 initial points was obtained by mapping the trajectory forward in time 7 (Runs 1, 2, and 4) or 10 (Run 5) mapping iterations from the initial point with no tidal dissipation, in order to thoroughly mix the phases σ_A and σ_U, but keep the "actions" the same. Since the trajectories are initially quasiperiodic there is, in principle, a transformation to action-angle variables. Under slow variation of parameters these actions are to first order conserved; the actions are first-order adiabatic invariants. For slightly different initial conditions the dynamical frequencies are slightly different, and the initial angles will rapidly be spread over all values. (Motion on the n-torus is ergodic.) Thus the essential parameters which determine the probabilities of various outcomes are the actions; the angles are physically unknowable and considered to be uniformly distributed in the calculation of probabilities. In the single resonance theory the phase corresponding to these angles is also assumed to be uniformly distributed in the calculation of probabilities.

The trajectories in δ, ΔE parameter space

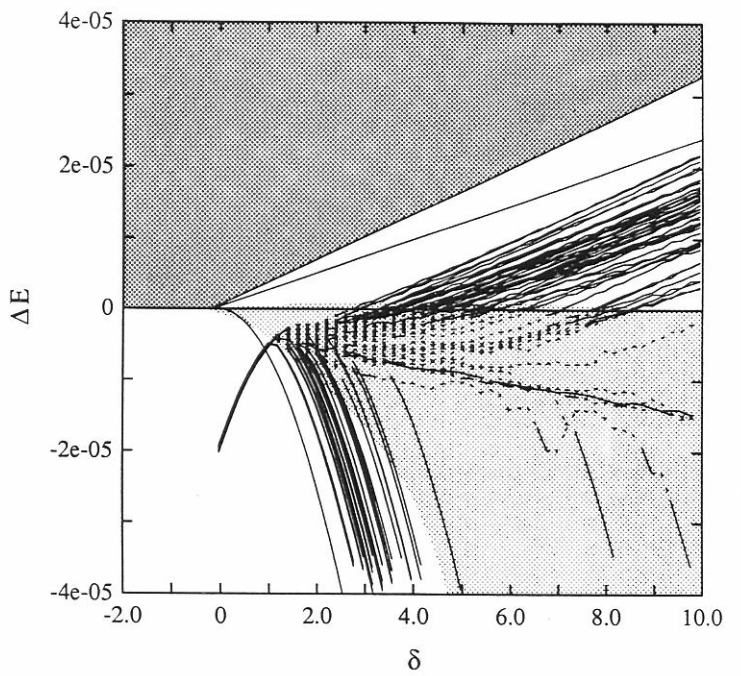

FIG. 12. Trajectories evolved through the resonance with a high tidal dissipation rate ($\mathcal{Q} = 0.11$). Solid lines indicate quasiperiodic behavior, dashed lines indicate chaotic behavior. The types of behavior possible for each orbit may be determined by comparing this figure with Fig. 1a. Evolution of these trajectories is strongly affected by the rate of tidal dissipation: the extremely wide range of outcomes is an artifact of evolving the system too rapidly through resonance. These trajectories have the same initial conditions as the trajectories in Run 3 (Fig. 15), but the dissipation rate is 1000 times higher. This picture is more exciting than that presented in Fig. 15, but *this picture is wrong*.

are represented by solid lines when the evolution is quasiperiodic and by dashed lines when the evolution is chaotic, as determined by evaluation of the rate of growth of the distance between nearby trajectories (Lyapunov exponent) at discrete intervals in δ along the trajectories.

The trajectories appear to have nearly

TABLE II

INITIAL PARAMETERS

Run	ΔE	δ	a_A a_U	e_A e_U	σ_A σ_U	x_A x_U	y_A y_U
1	-9.4511×10^{-7}	−0.1781	7.1633 10.0703	0.0017 0.0043	270.0 270.0	0.0 0.0	-1.4649×10^{-3} -3.9289×10^{-3}
2	-5.6281×10^{-6}	−0.1869	7.1625 10.0703	0.005 0.005	90.0 90.0	0.0 0.0	4.3084×10^{-3} 4.5685×10^{-3}
3	-1.9623×10^{-5}	−0.0283	7.1611 10.0703	0.0102 0.0031	90.0 45.0	0.0 0.002	8.7907×10^{-3} 0.002
4	-2.1626×10^{-5}	1.4263	7.1610 10.0703	0.01 0.01	0.0 0.0	8.6168×10^{-3} 9.1371×10^{-3}	0.0 0.0
5	-6.0706×10^{-5}	2.0000	7.1588 10.0703	0.0125 0.0125	0.0 0.0	1.0771×10^{-2} 1.1421×10^{-2}	0.0 0.0

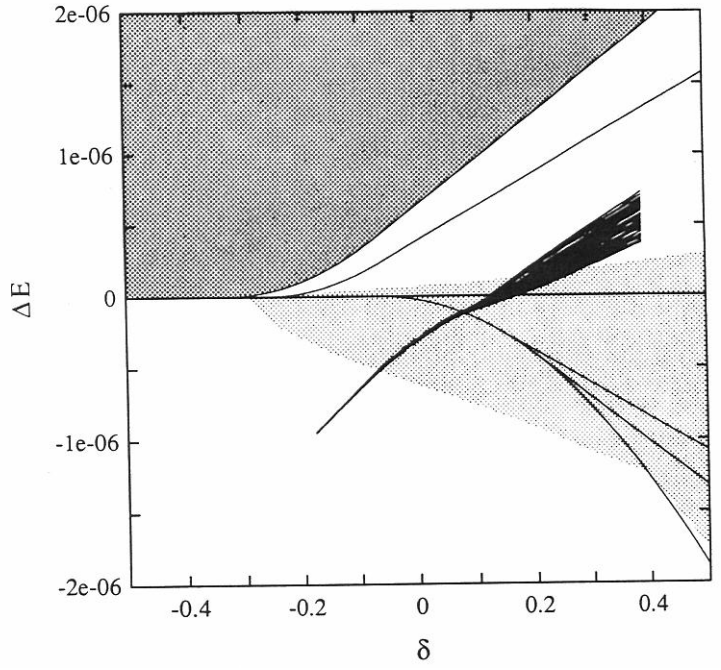

FIG. 13. Trajectories in $\delta,\Delta E$ parameter space for Run 1 with $\mathfrak{Q} = 110$. Solid lines indicate quasiperiodic behavior, dashed lines indicate chaotic behavior. The types of behavior possible for each orbit may be determined by comparing this figure with Fig. 1b. None of the trajectories in this set escaped from the resonance.

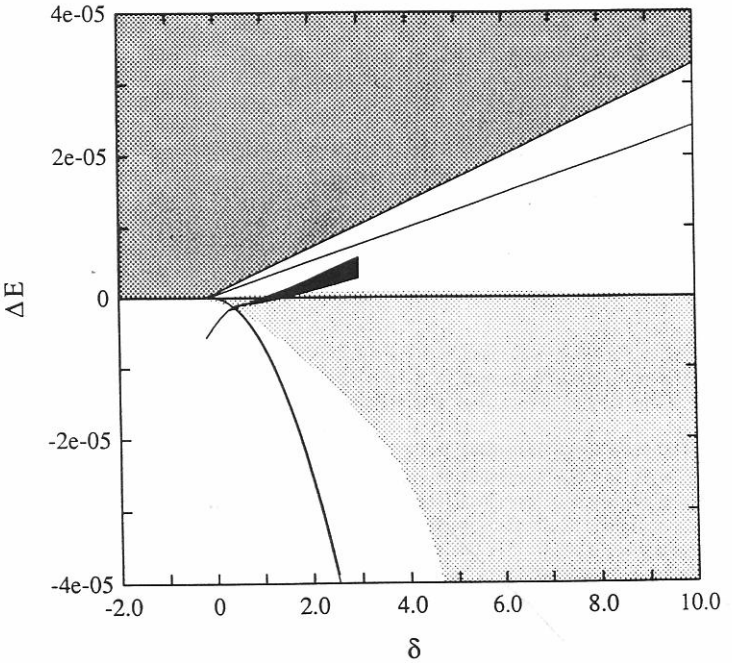

FIG. 14. Trajectories in $\delta,\Delta E$ parameter space for Run 2 with $\mathfrak{Q} = 110$. Solid lines indicate quasiperiodic behavior, dashed lines indicate chaotic behavior. The types of behavior possible for each orbit may be determined by comparing this figure with Fig. 1a. Only one of these trajectories escaped from the resonance (see Table III), closely following the curve of $E = 0.0$.

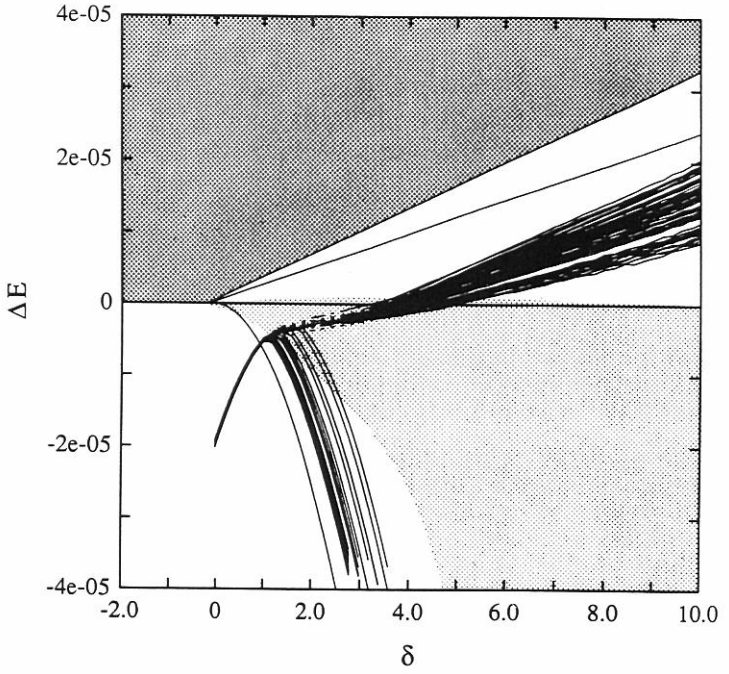

FIG. 15. Trajectories in δ, ΔE parameter space for Run 3 with $\mathfrak{Q} = 110$. Solid lines indicate quasiperiodic behavior, dashed lines indicate chaotic behavior. The types of behavior possible for each orbit may be determined by comparing this figure with Fig. 1a. Of the 100 trajectories, 29 escaped from the resonance.

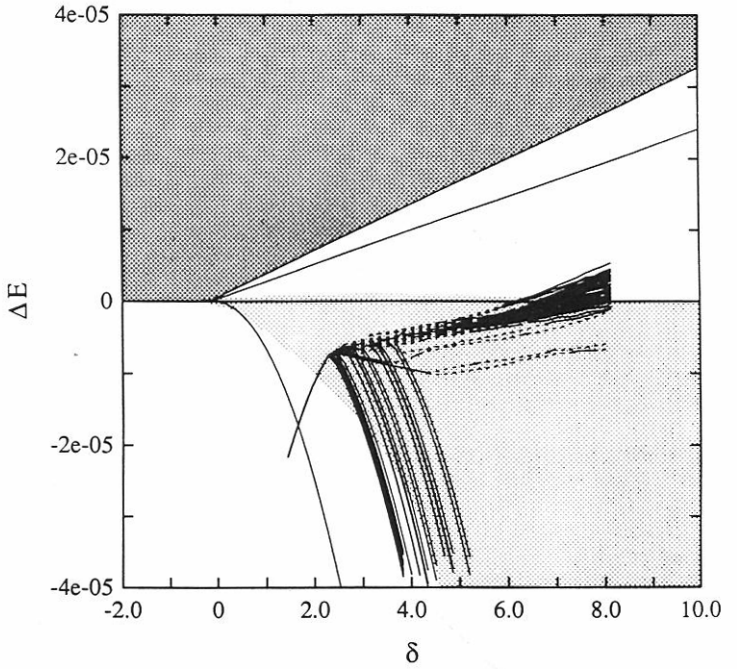

FIG. 16. Trajectories in $\delta, \Delta E$ parameter space for Run 4 with $\mathfrak{Q} = 110$. Solid lines indicate quasiperiodic behavior, dashed lines indicate chaotic behavior. The types of behavior possible for each orbit may be determined by comparing this figure with Fig. 1a. All of the trajectories which did not escape by the end of the run displayed were eventually captured into the resonance. Of the 100 trajectories, 28 escaped from the resonance. The trajectories which appear linear and quasiperiodic between $\delta \approx 2.5$ and $\delta \approx 4.5$ are temporarily captured into a quasiperiodic region of phase space in which σ_A librates.

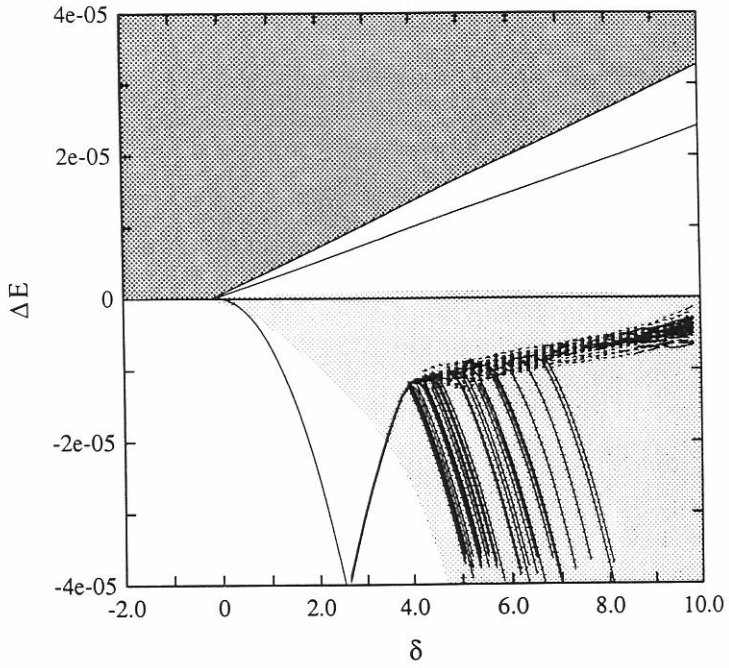

FIG. 17. Trajectories in $\delta, \Delta E$ parameter space for Run 5 with $\mathcal{Q} = 110$. Solid lines indicate quasiperiodic behavior, dashed lines indicate chaotic behavior. The types of behavior possible for each orbit may be determined by comparing this figure with Fig. 1a. All of the trajectories which did not escape by the end of the run displayed were eventually captured into the resonance. Of the 100 trajectories, 39 escaped from the resonance.

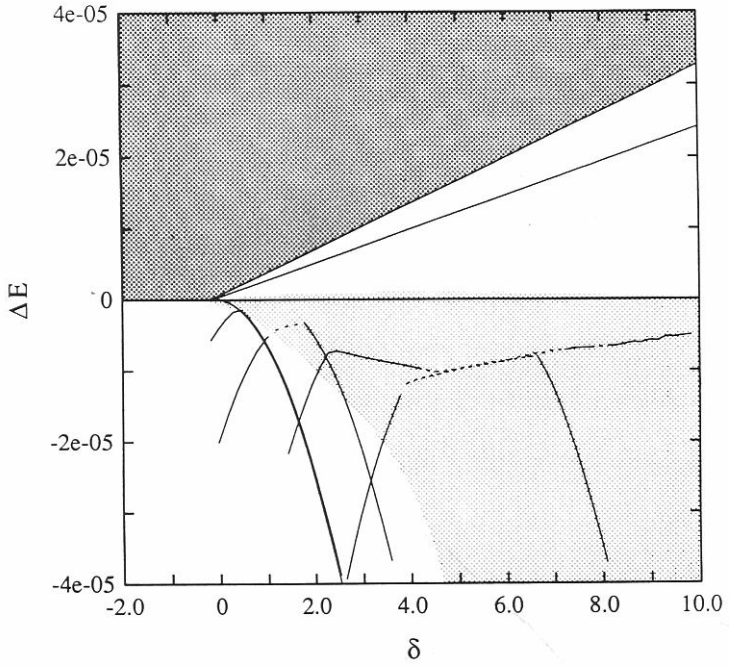

FIG. 18. This plot shows the evolution in $\delta, \Delta E$ parameter space of selected trajectories from Runs 2 to 5 as they evolve through the 5:3 mean-motion commensurability. The corresponding behavior of the eccentricities of Ariel and Umbriel for these trajectories during resonance passage can be seen in Figs. 19–22.

the same evolution in ΔE until they first become chaotic. This can be understood in terms of the first-order adiabatic invariance of the actions of the trajectories while they are quasiperiodic. The paths begin to diverge in the chaotic region.

Sample trajectories from each of Runs 2–5 have been plotted in Fig. 18. Figure 19–22 show the eccentricity variations of Ariel and Umbriel for these trajectories. The maximum and minimum eccentricities in small intervals of δ (Fig. 19: $\Delta\delta \approx 0.0007$, Fig. 20: $\Delta\delta \approx 0.001$, Fig. 21: $\Delta\delta \approx 0.003$, and Fig. 22: $\Delta\delta \approx 0.002$) are plotted versus δ. These "envelopes" are smooth when the trajectory is quasiperiodic, but the maxima and minima vary in an irregular fashion in the chaotic zone. In each case, the maximum eccentricity in the chaotic zone is higher than the initial eccentricity. Note that in some cases, the average eccentricity of Umbriel after escape from the resonance is higher than the average eccentricity before the resonance is encountered (e.g., Fig. 20b), a phenomenon not possible in the standard theory of evolution through isolated mean-motion resonances

Figure 23 shows the eccentricity variations of a trajectory from Run 5 integrated with $\mathcal{Q} = 3300$, which is close to the maximum dynamically allowed tidal dissipation rate in Uranus. The plot was produced in the same manner as Figs. 19–22, showing the maximum and minimum eccentricities in intervals of $\Delta\delta \approx 0.003$. The decrease of effective dissipation rate by a factor of 30 does not dramatically affect the dynamics—features which are seen in this figure are similar to those seen in the previous figures. This trajectory was captured into the resonance.

Figure 24 shows the chaotic variations in eccentricity of part of the trajectory shown in Fig. 22, with the scale of δ greatly enlarged. The eccentricities of the satellites vary in an irregular manner. This behavior is similar to that observed for asteroid motion in the chaotic zone associated with the 3 : 1 Kirkwood gap (Wisdom 1982, 1983). Note that for $6.008 < \delta < 6.017$ the mean eccentricity of Ariel is relatively high while the mean eccentricity of Umbriel is relatively low. There are relatively sudden changes in the eccentricities at the boundaries of this range in δ. Outside of this range of δ, the mean eccentricity of Ariel is relatively low, while the mean eccentricity of Umbriel is relatively high. This behavior is typical for trajectories in the chaotic zone: there are time intervals during which the mean eccentricity of Ariel is relatively high while that of Umbriel is relatively low, during other time intervals the mean eccentricity of Umbriel is high while that of Ariel is low, with relatively sudden transitions between these intervals. This behavior results in the erratic alternations between high and low maximum eccentricity seen in Figs. 19–23.

Since the tidal dissipation is small, the change in energy over a short time interval is also small, and the system can be considered approximately Hamiltonian. It is possible to study the qualitative behavior of a trajectory by "freezing" the value of δ and computing surfaces of section. This allows us to determine which regions of phase space are accessible to a trajectory at particular values of δ and ΔE, and the types of behavior that are possible in each region.

As discussed in Section 4.1, for chaotic trajectories points appear in an irregular manner on the sections corresponding to all four root families. The trajectories are observed to spend some time with low values of both e_U and e_A, during which time points appear on sections I*b*, I*c*, II*b*, and II*c*. Trajectories may jump back and forth between regions near to and far from the origin, during which time points appear on all sections corresponding to all four root families. They may also spend time with high values of both e_U and e_A, during which time points appear on sections I*a*, I*d*, II*a*, and II*d*.

During the periods of time when points appear on sections corresponding only to either the outer root families or the inner root families, there is a correlation between the eccentricities of Ariel and Umbriel. At

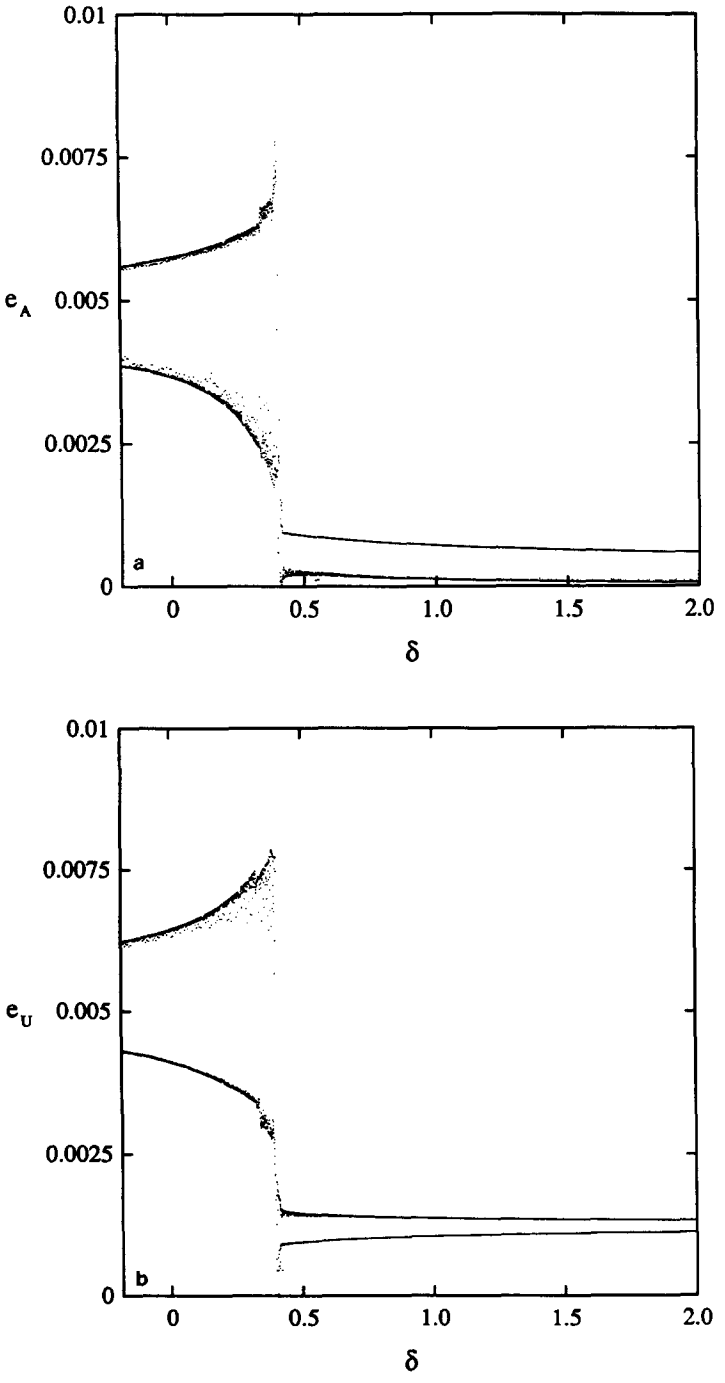

FIG. 19. Eccentricity variations of the trajectory from Run 2 which escaped from the resonance. Shown are the maximum and minimum eccentricities of Ariel (a) and Umbriel (b) in intervals of $\Delta\delta \approx 0.0007$.

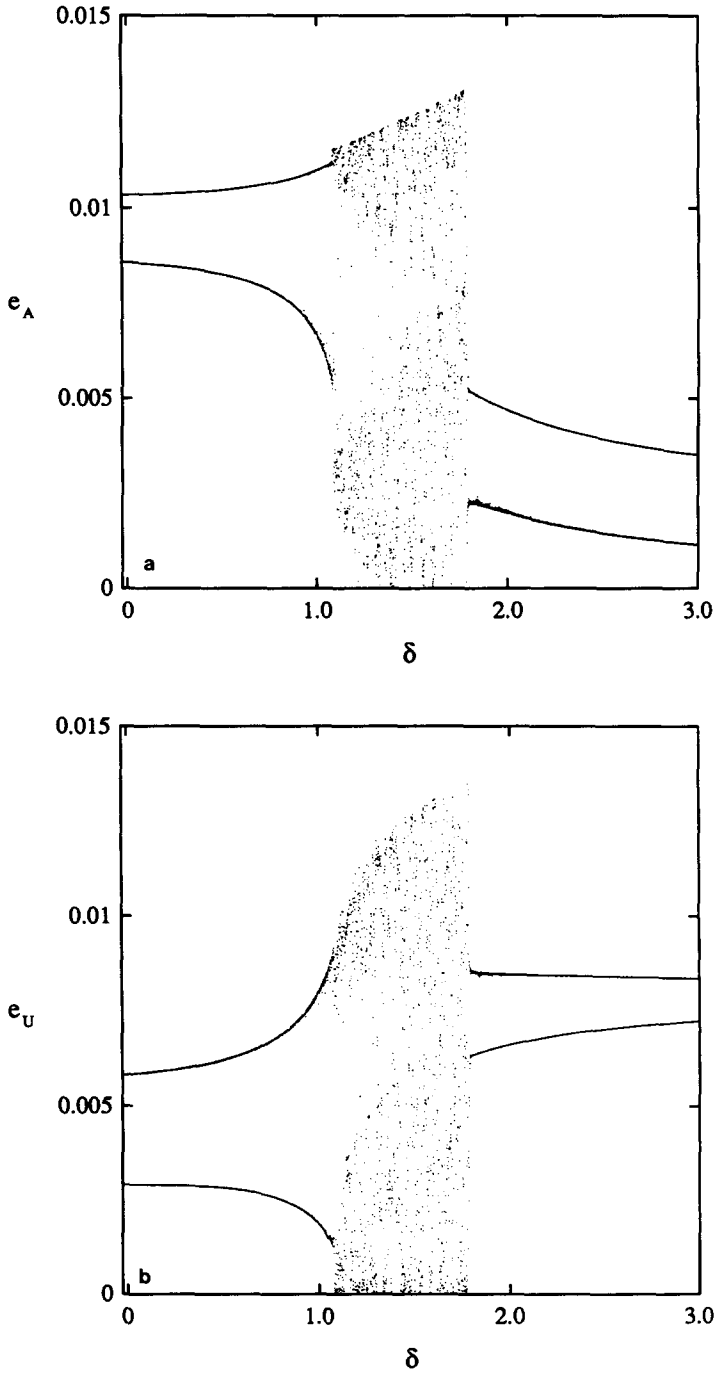

FIG. 20. Eccentricity variations of a trajectory from Run 3 which escapes from the resonance. Shown are the maximum and minimum eccentricities of Ariel (a) and Umbriel (b) in intervals of $\Delta\delta \approx 0.001$. In this example, the average eccentricity of Umbriel after escape from the resonance is higher than the average value before the resonance is encountered.

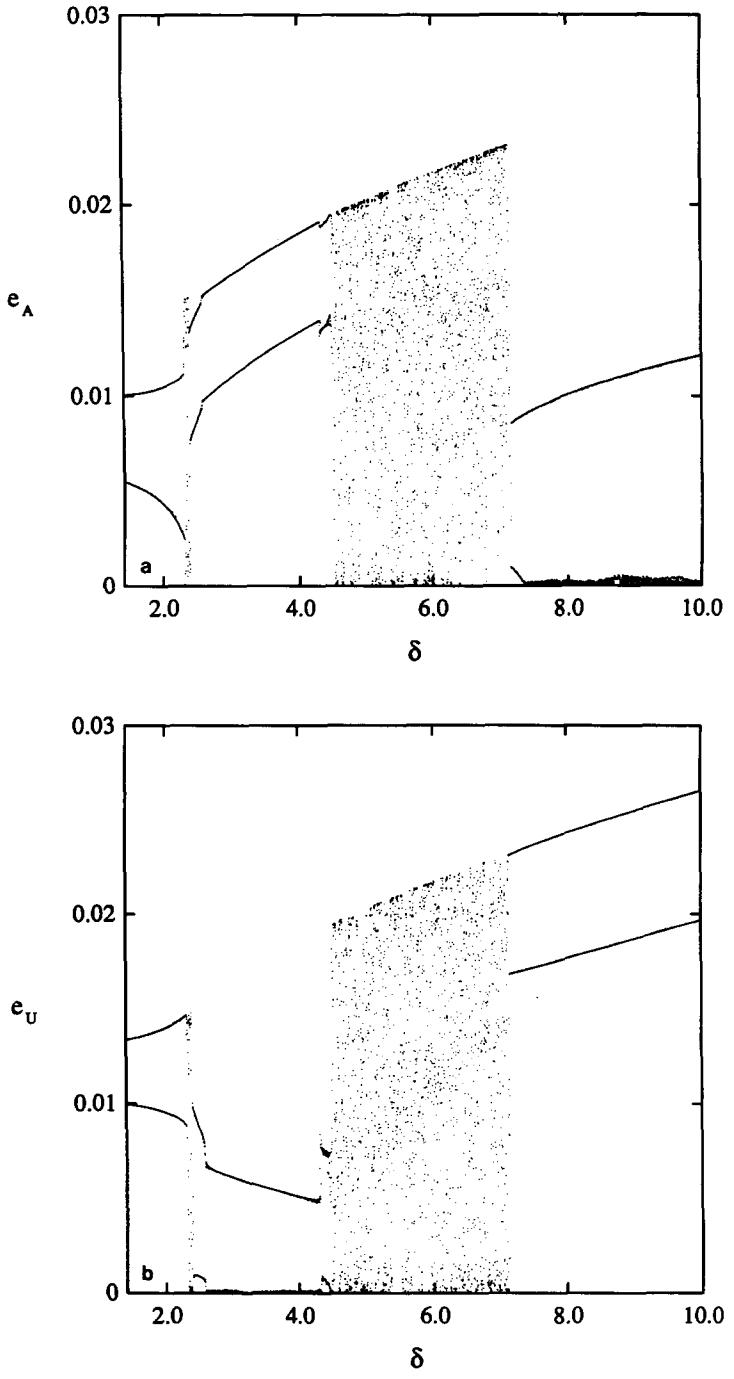

FIG. 21. Eccentricity variations of a trajectory from Run 4 which is temporarily captured into a resonant island. Shown are the maximum and minimum eccentricities of Ariel (a) and Umbriel (b) in intervals of $\Delta\delta \approx 0.003$. Between $\delta \approx 2.5$ and $\delta \approx 4.5$, the eccentricity of Ariel increases during quasiperiodic libration of σ_A. After entering the chaotic region again, the trajectory is ultimately captured into the resonance.

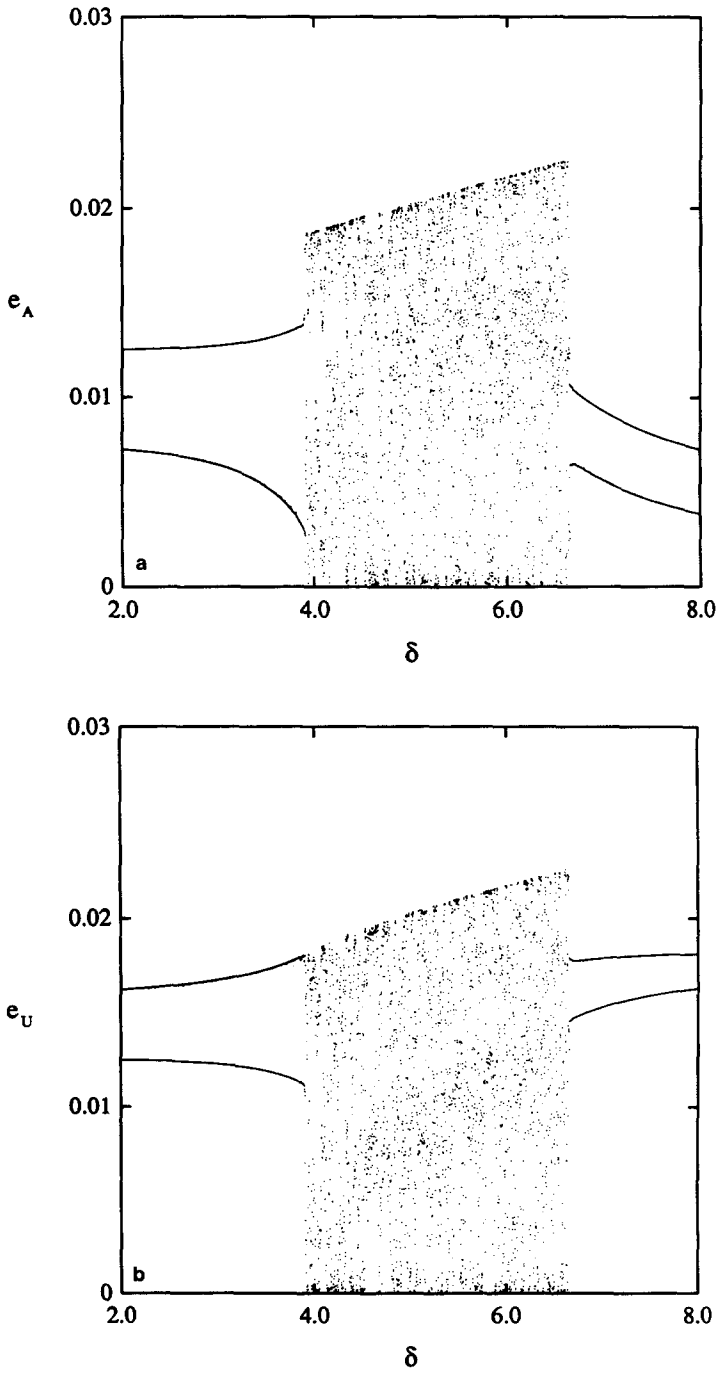

FIG. 22. Eccentricity variations of a trajectory from Run 5. Shown are the maximum and minimum eccentricities of Ariel (a) and Umbriel (b) in intervals of $\Delta\delta \approx 0.002$. For this trajectory, the average eccentricity of Umbriel after escape from the resonance is also higher than the average value before the resonance is encountered.

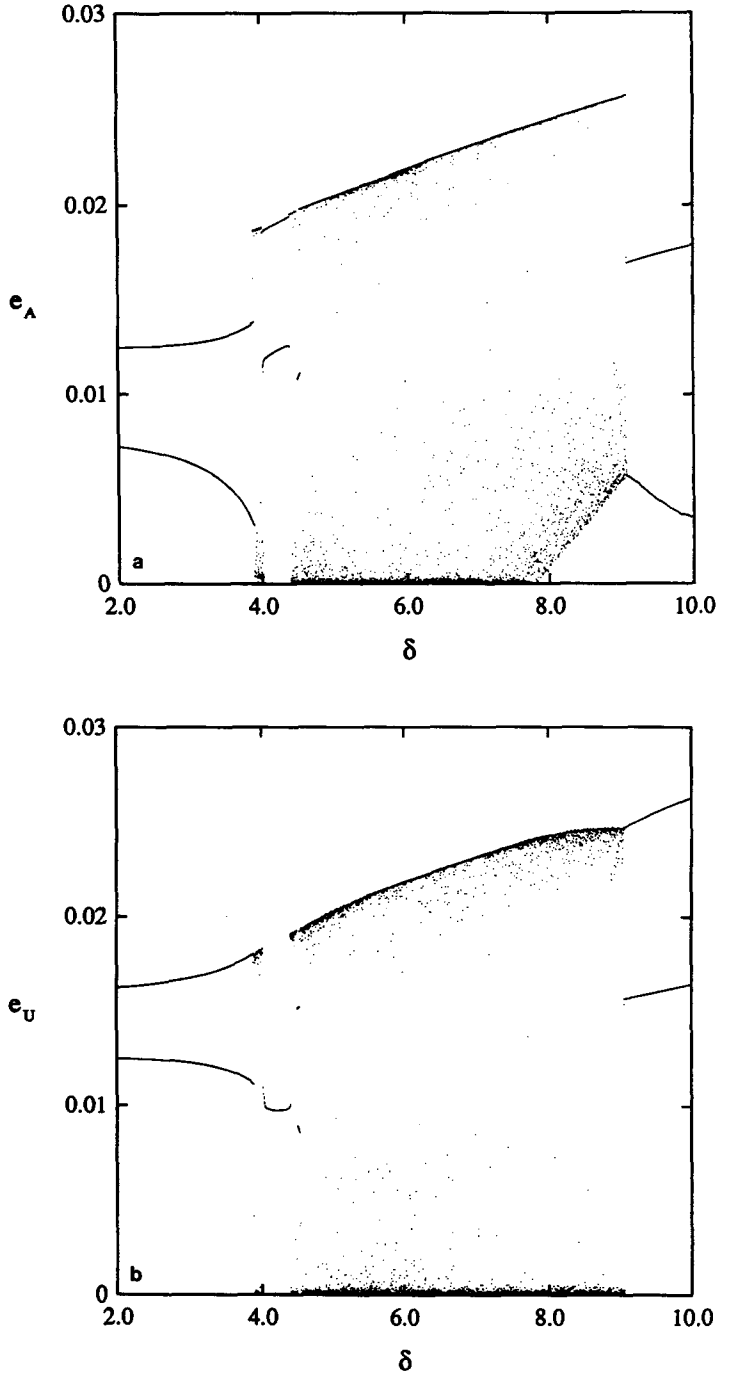

FIG. 23. Eccentricity variations of a trajectory with the same initial conditions as the trajectory shown in Fig. 22, but with the tidal dissipation rate 30 times smaller. Shown are the maximum and minimum eccentricities of Ariel (a) and Umbriel (b) in intervals of $\Delta\delta \approx 0.003$. Between $\delta \approx 4$ and $\delta \approx 4.4$, σ_A was captured into temporary quasiperiodic libration. This trajectory is ultimately captured into the resonance.

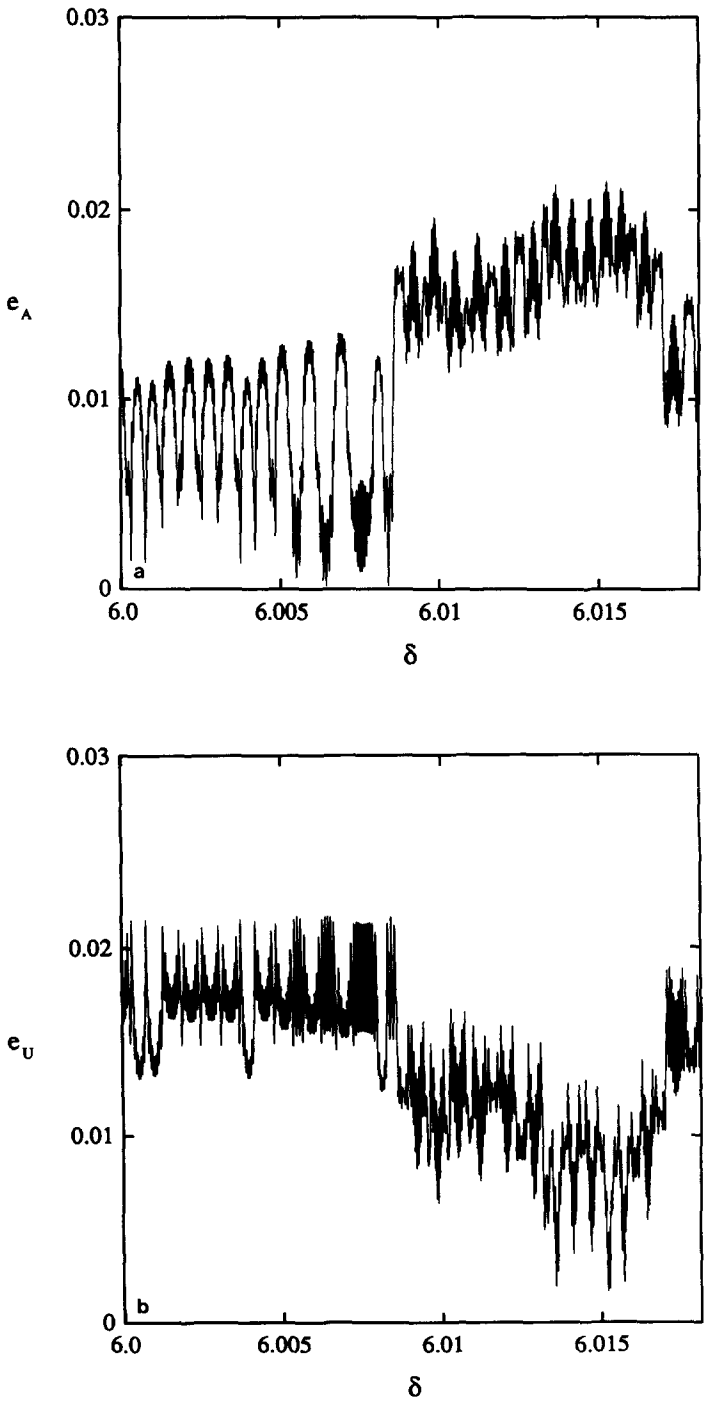

FIG. 24. The eccentricity variations of Ariel (a) and Umbriel (b) in the chaotic zone for the trajectory shown in Fig. 22 are shown at a greatly expanded scale. The time resolution of this plot is one mapping period ($\Delta t = 2\pi/20$ years). The eccentricities of both satellites vary in an irregular manner. At $\delta \approx 6.008$, the average eccentricity of Ariel increases suddenly, while the average eccentricity of Umbriel decreases. At $\delta \approx 6.017$, the average eccentricity of Ariel decreases suddenly, while the average eccentricity of Umbriel increases.

such times, a relatively high eccentricity for Ariel requires a relatively low eccentricity for Umbriel, and vice versa. This results in the interesting behavior of the eccentricities displayed in Fig. 24: over relatively short time scales, the mean eccentricity of one satellite is high while that of the other satellite is low. The eccentricities alternate between high and low mean values in an irregular manner. Eccentricities tend to be higher when points are appearing on the outer root sections.

While the trajectory is chaotic, ΔE evolves in a surprisingly regular manner to higher values with increasing δ, provided that the rate of tidal evolution is slow. Qualitative changes in the evolution of ΔE have been associated with temporary capture onto the librating island surrounding the Mode II fixed point, or with the trajectory "sticking" to a quasiperiodic island for a period of time.

Figure 21 shows some of this interesting behavior: after becoming chaotic, the trajectory apparently becomes quasiperiodic again, during which time the eccentricity of Ariel increases considerably. It then becomes chaotic again, exhibiting eccentricity behavior similar to that of the other trajectories plotted. By plotting surfaces of section along this "quasiperiodic interlude," it was found that the trajectory was on one of the islands in the chaotic zone and on which σ_A librates in the full phase space. The trajectory became unstable again at a later time, possibly due to a change in the size of the island. It may also have been a case of "sticking," where the trajectory spent time near an island, and exhibited behavior which only appeared to be quasiperiodic (e.g., Wisdom 1983). The fact that two of the trajectories in Fig. 16 which exhibit this behavior become unstable at similar values of δ indicates that the phenomenon is not extremely sensitive to initial conditions, suggesting that the trajectory actually was captured onto the quasiperiodic island and not stuck to it. Temporary quasiperiodic libration has served as a conduit to higher eccentricity for Ariel, resulting in maximum eccentricities more like those of the system shown in Fig. 22, which has higher initial eccentricities. The energy evolution of these two trajectories in the chaotic zone further indicates the similarity. This particular trajectory is eventually captured, but examination of the trajectory in Fig. 18 indicates that escape is possible for similar trajectories. The trajectory from Run 5 in Fig. 18, which escapes to large negative ΔE, overlaps the trajectory from Run 4, indicating a period in which evolution through the chaotic zone occurred in the same region of phase space. This mechanism of temporary quasiperiodic libration allows for the possibility that trajectories approaching the resonance with relatively low eccentricities could be driven to much higher eccentricities than they would with the evolution in the chaotic zone alone, and the satellites might escape from the resonance with higher eccentricities than they had approaching the resonance. The trajectory shown in Fig. 23 also shows this phenomenon of temporary capture.

Trajectories may escape from the resonance almost immediately, or may spend a considerable period of time in the chaotic zone before they escape, during which time the maximum eccentricities can be driven to relatively high values.

Eventually, the trajectories become quasiperiodic again. The final states of the trajectories fall into two major categories: trajectories which escape from the resonance and trajectories which are captured into resonance. For trajectories which are captured ΔE increases and ends up in the upper half of the parameter space; for trajectories which escape ΔE decreases to large negative values.

Those trajectories which evolve to large negative ΔE escape into the large quasiperiodic region on the sections corresponding to root families b and c, in which both resonant arguments circulate. This requires that both eccentricities have low mean values in the chaotic zone (with points appearing only on sections Ib,c and IIb,c) for a period of time long enough to allow evolution into

this quasiperiodic zone. Then, as δ evolves to higher values, the system moves away from the resonance region, and the dynamics of the system are dominated by the secular interactions between the satellites, as they were before the system encountered the commensurability.

Examination of section II for $\Delta E \geq 0$ (see Fig. 7) indicates that capture into resonance occurs when the two regions of the section defined by the energy surface boundary separate. Trajectories appear to be confined to one region of phase space or the other, and σ_U must librate. We therefore have capture into resonance through evolution of the energy surface. There is a relatively small region of parameter space for ΔE just larger than zero where the trajectory can still be chaotic (see Fig. 1). A trajectory can therefore be captured into resonance, yet still be chaotic. This phenomenon is a novel feature of our problem. As the system continues to evolve, the two "bubbles" move apart on sections II, and the eccentricity of Umbriel increases. In addition, the large chaotic zone disappears, and trajectories become quasiperiodic, indicating permanent capture into the resonance involving the longitude of pericenter of Umbriel's orbit. If further evolution of the trajectory results in $\Delta E > E_1 - E_2$, the energy surface also divides Sections I into two regions in which σ_A must librate (see Section 3.1). As the system continues to evolve, these two "bubbles" also move apart on sections I, and the eccentricity of Ariel increases. The orbits of both satellites are trapped into quasiperiodic libration.

The island surrounding the Mode II fixed point could provide another mechanism of capture, although the ultimate stability of the island is unknown.

The observed spread in outcomes contrasts with the behavior of trajectories in the single resonance approximation (see, e.g., Borderies and Goldreich 1984), in which the outcomes are probabilistic due to an unknown phase, but are otherwise quite predictable. The presence of a chaotic zone in this problem indicates that the outcome is inherently unpredictable (though still deterministic), due to the extreme sensitivity of the motion to initial conditions. Two trajectories entering the chaotic zone with even very similar phases will diverge exponentially, making it impossible to predict their comparative evolutions over the long term. The width of the chaotic zone when a trajectory enters it may be important. The probability of escape may be much larger for a trajectory if the chaotic zone is narrow and the quasiperiodic region of escape on sections corresponding to root families b and c occupies a majority of the phase space. This is inferred from observations that most escapes occur very shortly after the trajectories become chaotic, when the chaotic zone occupies a relatively small region of phase space.

The trajectories in each of the runs described so far in this paper originally all have the same actions. The actions depend on the positions of the invariant curves on a section. There appears to be a dependence of the probability of escape on the initial distribution of energy between the normal modes, and therefore on the actions. Figure 25 shows the energy evolution of trajectories with the same δ's and ΔE's as the five runs in Fig. 13–17, but the trajectory on which the initial points are computed generates invariant curves on sections I and II which are now very close to the fixed point associated with Mode I. Ten trajectories were integrated for each run. For these trajectories, the evolution of energy is markedly different from the evolution of the corresponding trajectories in Figs. 13–17: the trajectories all evolve to much higher values of ΔE before becoming chaotic. All of the trajectories were captured into resonance. The details of the secular interactions between the satellites before the resonance is encountered have a significant effect on the outcome of the passage through the resonance.

4.3. Statistics of Escape

Overall escape statistics are given in Table III. There is a trend toward higher prob-

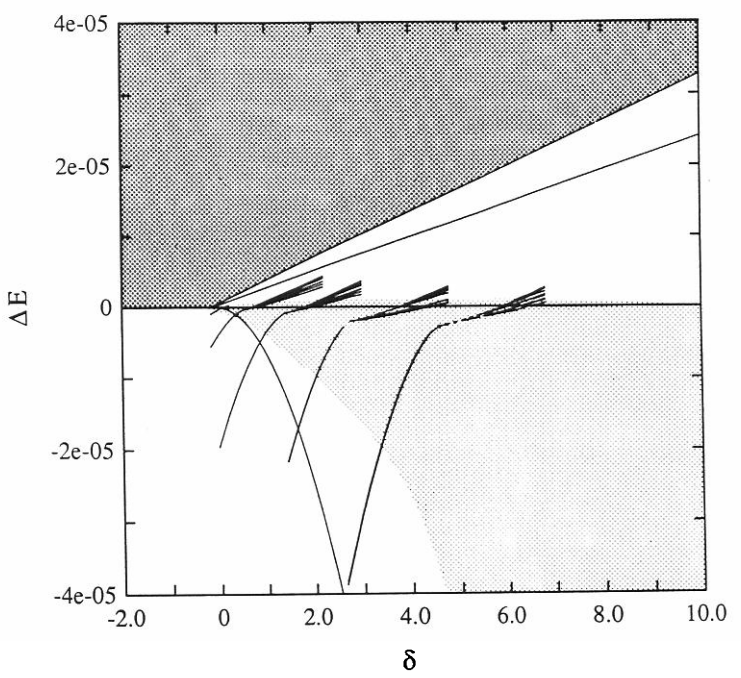

FIG. 25. Trajectories in $\delta, \Delta E$ parameter space with initial coordinates near the Mode I fixed point. The initial values of δ and ΔE for each set of 10 trajectories are the same as the initial values of δ and ΔE for the corresponding sets of trajectories in Runs 1–5 (Figs. 13–17). Note that the trajectories become chaotic much closer to $\Delta E = 0$ than the corresponding trajectories in Figs. 13–17. None of the trajectories shown escaped from the resonance.

TABLE III

ESCAPE STATISTICS

Run	δ_0	$\langle e_{A0}\rangle^a$ $\langle e_{U0}\rangle$		$\langle\delta_{esc}\rangle$	$\langle e_{Amax}\rangle$ $\langle e_{Umax}\rangle$	$P_{esc}{}^b$	δ_f	$\langle e_{Af}\rangle$ $\langle e_{Uf}\rangle$
2	−0.187	0.00493	$^{+0.00066}_{-0.00108}$	0.412	0.0078	0.01	3.000	0.00034
		0.00503	$^{+0.00120}_{-0.00073}$		0.0074			0.00123
3	−0.028	0.00960	$^{+0.00064}_{-0.00110}$	1.182 ± 0.301	0.01170 ± 0.00052	0.29 ± 0.046	10.000	0.00345 ± 0.00101
		0.00417	$^{+0.00172}_{-0.00117}$		0.01071 ± 0.00143			0.00365 ± 0.00220
4	1.426	0.00837	$^{+0.00168}_{-0.00288}$	2.841 ± 0.463	0.01546 ± 0.00139	0.28 ± 0.036	8.114	0.00378 ± 0.00073
		0.01116	$^{+0.00218}_{-0.00122}$		0.01577 ± 0.00100			0.00937 ± 0.00161
5	2.000	0.01037	$^{+0.00215}_{-0.00315}$	4.757 ± 0.812	0.01916 ± 0.00216	0.39 ± 0.048	10.000	0.00541 ± 0.00092
		0.01401	$^{+0.00223}_{-0.00153}$		0.01953 ± 0.00136			0.01285 ± 0.00210

[a] Time average and range of eccentricity on initial trajectory.
[b] Error for P_{esc} is standard deviation of the mean. All other standard deviations for single value.

ability of escape from the resonance as the mean eccentricities of the satellites before the resonance is encountered are increased.

For both satellites, the maximum eccentricities in the chaotic zone are higher than the initial maximum eccentricities. The mean of the time-averaged final eccentricities for each satellite after escape from the resonance (last column in Table III) is comparable to or lower than the mean initial eccentricity (third column). Figure 26 shows the distribution of time-averaged fi-

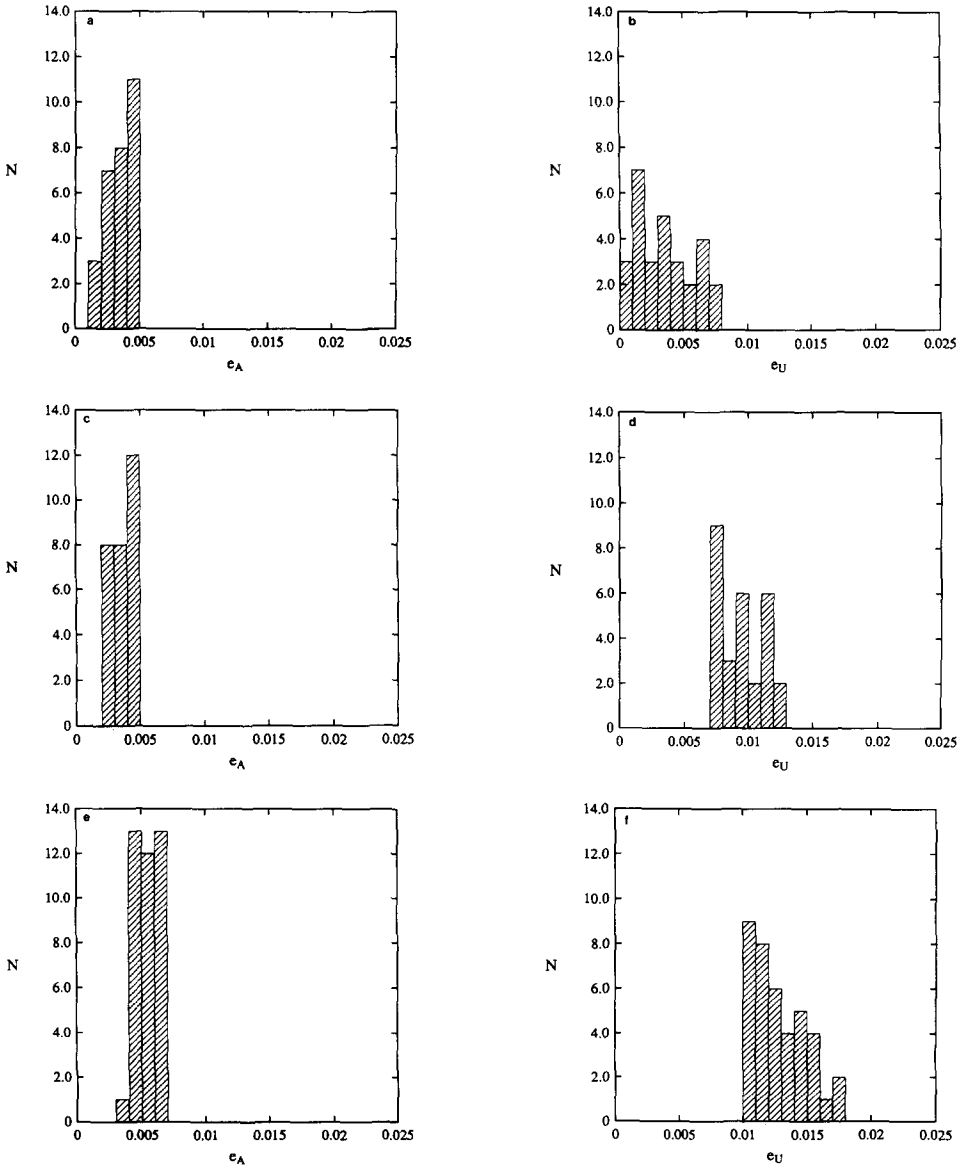

FIG. 26. Average final escape eccentricities. (a) and (b) refer to Run 3, (c) and (d) to Run 4, and (e) and (f) to Run 5. The average final eccentricity of Umbriel tends to be higher than the average final eccentricity of Ariel. Compare with average initial eccentricities, given in Table III. It is possible for the average final eccentricity of Umbriel to be higher than the average value before the resonance is encountered.

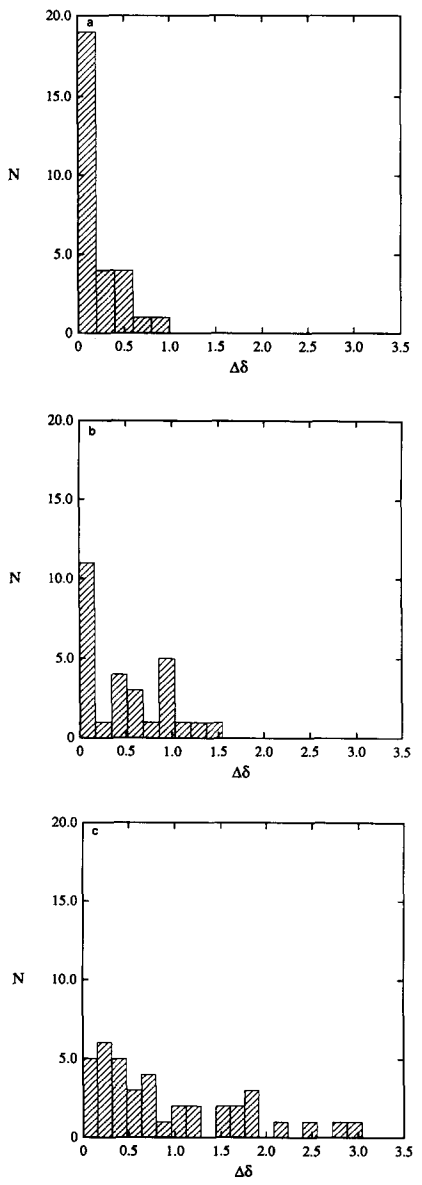

FIG. 27. $\Delta\delta$ spent in the chaotic zone for escaping trajectories. (a)–(c) refer to Runs 3–5, respectively. $\Delta\delta = 1.0$ corresponds to 6.9×10^6 years of evolution for $Q = 6600$. Trajectories with higher initial eccentricities tend to spend more time in the chaotic zone.

nal eccentricities after escape from the resonance. Note that in some cases the average final eccentricity of Umbriel after escape from the resonance is higher than the value before the resonance was encountered. This may be contrasted with the single resonance model in which the eccentricity after escape is always lower than the initial eccentricity.

There is a tendency for the average final eccentricity of Ariel to be lower than that of Umbriel. This can be understood by examining the structure of the sections corresponding to root families *b* and *c* (see Figs. 4b,c and 5b,c). The trajectories escape into the quasiperiodic regions surrounding the fixed point associated with Mode I, which is near the origin in Ariel variables and near the boundary in Umbriel variables determined by the energy integral.

Figure 27 shows the distribution of times spent in the chaotic zone in terms of δ for the escaping trajectories. For $Q = 6600$, $\Delta\delta = 1.0$ corresponds to about 6.9×10^6 years. There is a trend, with increasing initial eccentricity, for the distribution to spread out and for escaping trajectories to spend more time in the chaotic zone.

Figure 28 shows the distributions of maximum eccentricities in the chaotic zone for the escaping trajectories. There is a correlation between the length of time spent in the chaotic zone and the maximum eccentricity achieved—corresponding essentially to the upper "envelope" of eccentricity in the chaotic zones in Figs. 19–23. The trajectories travel up the chaotic zone to higher and higher eccentricities. The largest eccentricity reached in any of the escaping trajectories was the maximum of the trajectory in Fig. 22, approximately 0.023.

Note that some of the trajectories in Runs 4 and 5 (see Figs. 16 and 17) are still chaotic at the end of the run. When further evolved, none of these trajectories escaped.

5. DISCUSSION

Well before they encounter the 5:3 resonance, the orbital evolution of Ariel and Umbriel is dominated by their mutual secular perturbations. The eccentricities of the satellites oscillate between minimum and

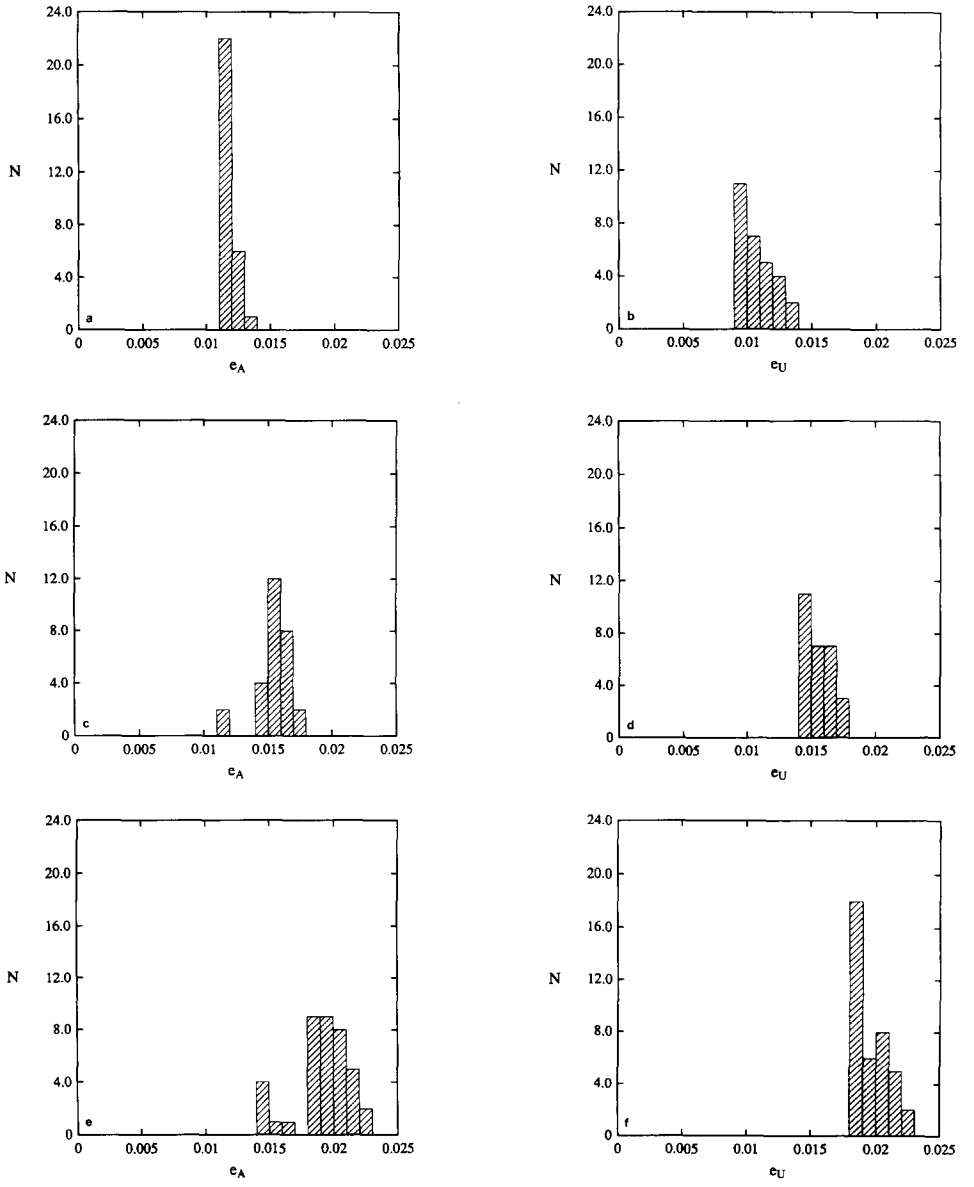

FIG. 28. Maximum eccentricities in chaotic zone. (a) and (b) refer to Run 3, (c) and (d) to Run 4, and (e) and (f) to Run 5. The maximum eccentricities of the two satellites in the chaotic zone tend to be comparable.

maximum values determined by the relative strengths of the two normal modes. The variations are quasiperiodic, with two fundamental frequencies associated with the modes, and with high-frequency perturbations superimposed. The semimajor axes slowly increase due to tidal dissipation in Uranus. The orbit of Ariel expands more rapidly than that of Umbriel, and as they approach the 5:3 mean-motion commensurability resonant perturbations become stronger. One of the secular modes eventually becomes unstable, and the system enters a large chaotic zone. Further tidal dissipation within Uranus may drive the eccentricities up the chaotic zone to rela-

tively high values. They may then either escape or be captured into resonance.

When the system enters the chaotic zone, a new low-eccentricity region of phase space is made accessible to the system. While in the chaotic zone, the system spends time in both regions of phase space, and the eccentricities irregularly alternate between high and low values. If the system is caught in the circulating quasiperiodic region in the low eccentricity region of phase space, it escapes from the resonance, and the orbits continue to differentially expand due to dissipation in Uranus. The average eccentricities after escape from the resonance tend to be lower than the values before the resonance is encountered, but in some cases the average eccentricity of Umbriel increases, a phenomenon not predicted by the standard single resonance theory of evolution through resonances. It may also be possible for the system to be temporarily captured into a librating island during passage through the resonance (see Section 4.2), with the result that the average eccentricities after escape from the resonance could be significantly higher than the values before the resonance is encountered. After escaping from the resonance, the evolution of the orbits is again dominated by their mutual secular perturbations, and the eccentricities slowly damp due to tidal dissipation within the satellites.

If the system does not escape, the energy surface divides into two separate regions. When this happens, the system is captured into resonance, even though the trajectory may still be chaotic. Initially, only σ_U librates, and tidal dissipation drives the orbit of Umbriel to higher eccentricity. The trajectory becomes quasiperiodic at some point. Eventually, σ_A may also be trapped into a librating state, and the eccentricity of Ariel is also driven to high values. Both orbits are then captured into the resonance.

The outcome of resonance passage does not depend simply on the mean eccentricities; the individual amplitudes of the secular modes appear to play a significant role. The probability of escape is higher for larger initial average eccentricities, but also depends on which secular mode is stronger. Since the satellites are not presently in the resonance, they must have escaped. It appears that in order for the probability of escape to have been significant, the average eccentricities before the resonance was encountered were probably higher than current values. The largest increases in eccentricity occur when the trajectory is temporarily captured into quasiperiodic libration during evolution through the resonance.

The relatively high current eccentricities must be explained. For the highest dynamically allowed rate of tidal dissipation in Uranus ($Q = 6600$), the time since resonance passage is about 3×10^8 years. For the lowest rate of tidal dissipation in Uranus which allows Ariel and Umbriel to encounter this commensurability, the time since resonance passage is of order 4×10^9 years. As discussed in Section 4.1, the time scales of direct tidal damping of the satellite eccentricities are about 10^8 years for Ariel and about 10^9 years for Umbriel. After escape from the resonance, the eccentricity of Ariel tends to be smaller than that of Umbriel, which is also the case at the present time. If the rate of tidal dissipation is near the maximum dynamically allowed value, the damping time scale for Umbriel is about a factor of 3 longer than the time since resonance passage, and that of Ariel is about a factor of 3 smaller. This indicates that the eccentricity of Umbriel has probably not changed significantly since resonance passage, and that the eccentricity of Ariel, which was probably lower than that of Umbriel immediately after escape from the resonance, has damped to still lower values, but not necessarily to negligible values, which is consistent with the current observations. The run with outcomes most closely resembling the current physical configuration is Run 3 (Fig. 15). The current relatively high eccentricities, then, are remnants of relatively high eccentricities after

passage through the resonance. Of course, the average eccentricities of the satellites for the initial conditions of Run 3 ($e_A \simeq 0.01$ and $e_U \simeq 0.003$) are quite high, so the problem is not really solved. We still require some mechanism to provide the satellites with high eccentricities before the resonance is encountered, unless the temporary capture into a quasiperiodic librating state occurred. In this case a trajectory approaching the resonance with low eccentricities could escape from the resonance with significantly higher eccentricities. It is difficult to determine if this happened to Ariel and Umbriel, but it is a tantalizing possibility. On the basis of our numerical experiments, temporary quasiperiodic capture seems to occur with relatively low probability. We point out, though, that our single run with $\mathcal{Q} = 3300$ showed this phenomenon.

If the rate of tidal dissipation in Uranus is near the minimum value which allows passage through this resonance ($Q = 100{,}000$), then the damping time scale for Umbriel is about a factor of 4 smaller than the time since resonance passage, and that of Ariel is about a factor of 40 smaller. In this case, the eccentricities would have damped significantly since passage through the resonance. Since the present eccentricities are high, this seems to argue for a Q of Uranus closer to the minimum allowed value.

Although Ariel and Umbriel have similar masses and radii (see Table I), the surfaces of the two satellites are quite different. Ariel has had a geologically active past (Smith *et al.* 1986, Plescia 1987), with faults, fractures, and flow features remaining on its surface. Umbriel presents a bland, heavily cratered, primitive surface. The density of Ariel is 1.66 ± 0.30 g cm^{-1} (Stone and Miner 1986). If the interior is differentiated, it will have a rocky core ($\rho \approx 3.0$ g cm^{-1}) about $0.7R_A$ in radius, surrounded by an icy mantle. If the mantle is solid, the rate of heat conduction through the mantle can be approximated by

$$\frac{dE}{dt} = -k4\pi R_A^2 \frac{\Delta T}{\Delta R}, \tag{25}$$

where k is the thermal conductivity of ice, R_A is the radius of Ariel, ΔT is the difference in temperature between the base of the mantle and the surface, and ΔR is the mantle thickness. If the bottom of the mantle is maintained just below the melting temperature of 273° K, conduction through a rigid ice mantle can remove approximately 10^{17} ergs/sec of thermal energy. This is approximately the thermal energy that would be released by radioactive decay of materials in the core with chondritic abundances, with an energy production of about 10^{-7} ergs g^{-1} sec^{-1} (Kaula 1968). It is also equivalent to the tidal heating produced if the eccentricity of Ariel is about 0.03, using the expression for the energy dissipation in a synchronously rotating satellite (e.g. Peale 1988):

$$\frac{dE_i}{dt} = -\frac{21}{2} \frac{k_{2i} M n_i^3 R_i^5}{a_i^3 Q_i} e_i^2 \tag{26}$$

with reasonable physical parameters for Ariel (see Table I). If the energy input to the interior exceeds this rate, the temperature at the base of the mantle can exceed the melting temperature. The mantle can become unstable to solid state convection (see Reynolds and Cassen 1979). The steady state configuration for the mantle in this case is a convecting solid layer topped by a rigid surface layer. This configuration is capable of removing heat at a significantly higher rate than the conducting configuration, and can still remain mostly solid.

Peale (1988) estimates that the solid state convection process could remove up to approximately 7×10^{17} ergs/sec of thermal energy from the interior of Ariel. The equivalent tidal dissipation rate in the satellite would result if the eccentricity of Ariel was about 0.09 at the 5 : 3 resonance, not taking into consideration possible enhancement due to radioactive decay in the interior. A higher eccentricity would result in large-scale melting of the interior of Ariel. The

maximum eccentricity reached by Ariel in this study for an escaping trajectory is approximately 0.023. Considering our results in the planar approximation, it seems unlikely that passage through the 5:3 resonance alone could have melted the interior of Ariel. Furthermore, the rate of energy dissipation in Ariel equals the energy input to the orbit due to dissipation in Uranus for an eccentricity of about 0.05 (for $Q = 6600$). This provides an upper limit on the eccentricity that can be maintained through tidal evolution of the orbit, assuming that an equilibrium configuration is achieved by the system. Since this eccentricity is lower than that estimated for the melting of the interior of Ariel, the eccentricity of Ariel may never reach the value required for melting. Umbriel is clearly not thermally affected by passage through the resonance—it requires an eccentricity of about four times that of Ariel for an equivalent tidal thermal input.

The Hamiltonian studied in this project neglects dissipation in the satellite during the relatively brief period of resonance passage. The damping of the eccentricities can slow down the rate of evolution of δ, as well as directly affecting the x_i and y_i. A possible consequence is that the system could have remained in the chaotic zone for a longer period of time and may have reached higher eccentricities before escaping.

The inclinations were also neglected. Lowest order terms in the disturbing function for inclination involve terms of order $\sin^2(I/2)$, where I is the mutual inclination of the two orbits. For current values of the inclinations, this quantity is of the same order as e^2. Therefore, the inclination terms could have contributed significantly to the evolution of the system. It has been found (Wisdom 1983, 1987) that in the case of resonant asteroid motion, including inclination terms can lead to much higher eccentricities than in the planar case. A similar qualitative change in the behavior of this system may result.

The passage of Ariel and Umbriel through the 5:3 mean-motion commensurability is significantly affected by the presence of a large chaotic zone. The mechanism of capture is qualitatively different from the isolated resonance capture mechanism. Relatively large eccentricities are obtained while the trajectory is chaotic even if the trajectory ultimately escapes. Peak eccentricities for escaping trajectories are typically of order two to three times the initial eccentricities. Eccentricity increases large enough to have a significant affect on the thermal history of Ariel have not been found in this study.

6. APPENDIX I

6.1. *Averaged Planar Hamiltonian*

The problem to be considered is the planar Ariel–Umbriel system near the 5:3 mean-motion commensurability. The Hamiltonian of this system can be written

$$\mathcal{H} = \mathcal{H}_K + \mathcal{H}_O + \mathcal{H}_S + \mathcal{H}_R, \quad (27)$$

where $\mathcal{H}_K$ is the sum of the unperturbed Keplerian terms, $\mathcal{H}_O$ is the perturbation due to the oblateness of Uranus, $\mathcal{H}_S$ is the perturbation due to the secular interaction between the satellites, and $\mathcal{H}_R$ is the perturbation due to the resonant interaction between the satellites. In the following development, subscript A refers to Ariel and subscript U to Umbriel.

Expressing the contributions in terms of Keplerian elements, were a_i is the semimajor axis, e_i is the eccentricity, λ_i is the mean longitude, and $\bar{\omega}_i$ is the longitude of perihelion,

$$\mathcal{H}_K = -\frac{GMm_A}{2a_A} - \frac{GMm_U}{2a_U}. \quad (28)$$

Keeping only the J_2 terms to second order in eccentricity in the expression of the potential for an oblate planet,

$$\mathcal{H}_O = -\frac{GMm_A}{2a_A} J_2 \left(\frac{R}{a_A}\right)^2 \left[1 + \frac{3}{2} e_A^2\right] - \frac{GMm_U}{2a_U} J_2 \left(\frac{R}{a_U}\right)^2 \left[1 + \frac{3}{2} e_U^2\right], \quad (29)$$

and from the expression for the disturbing function,

$$\mathcal{H}_S = -\frac{Gm_A m_U}{a_U}\left[(1)^{(0)} + (2)^{(0)}\left(\frac{e_A}{2}\right)^2 + (3)^{(0)}\left(\frac{e_U}{2}\right)^2 + (21)^{(-1)}\frac{e_A}{2}\frac{e_U}{2}\cos(\tilde{\omega}_A - \tilde{\omega}_U)\right] \quad (30)$$

and

$$\mathcal{H}_R = -\frac{Gm_A m_U}{a_U} \times \left[(172)^{(5)}\left(\frac{e_A}{2}\right)^2 \cos(5\lambda_U - 3\lambda_A - 2\tilde{\omega}_A) + (182)^{(4)}\frac{e_A}{2}\frac{e_U}{2}\cos(5\lambda_U - 3\lambda_A - \tilde{\omega}_A - \tilde{\omega}_U) + (192)^{(3)}\left(\frac{e_U}{2}\right)^2 \cos(5\lambda_U - 3\lambda_A - 2\tilde{\omega}_U)\right], \quad (31)$$

where (see Leverrier 1855)

$$(1)^{(0)} = \frac{1}{2}b^0_{1/2}(\alpha)$$

$$(2)^{(0)} = \alpha\frac{d}{d\alpha}b^0_{1/2}(\alpha) + \frac{1}{2}\alpha^2\frac{d^2}{d\alpha^2}b^0_{1/2}(\alpha)$$

$$(3)^{(0)} = (2)^{(0)}$$

$$(21)^{(-1)} = 2b^1_{1/2}(\alpha) - 2\alpha\frac{d}{d\alpha}b^1_{1/2}(\alpha) - \alpha^2\frac{d^2}{d\alpha^2}b^1_{1/2}(\alpha)$$

$$(172)^{(5)} = \frac{75}{2}b^5_{1/2}(\alpha) + 9\alpha\frac{d}{d\alpha}b^5_{1/2}(\alpha) + \frac{1}{2}\alpha^2\frac{d^2}{d\alpha^2}b^5_{1/2}(\alpha)$$

$$(182)^{(4)} = -72b^4_{1/2}(\alpha) - 18\alpha\frac{d}{d\alpha}b^4_{1/2}(\alpha) - \alpha^2\frac{d^2}{d\alpha^2}b^4_{1/2}(\alpha)$$

$$(192)^{(3)} = \frac{67}{2}b^3_{1/2}(\alpha) + 9\alpha\frac{d}{d\alpha}b^3_{1/2}(\alpha) + \frac{1}{2}\alpha^2\frac{d^2}{d\alpha^2}b^3_{1/2}(\alpha) \quad (32)$$

and α is the ratio of semimajor axes, and $b^j_s(\alpha)$ are Laplace coefficients.

Near the resonance, the evolution of e_i and $\tilde{\omega}_i$ is dominated by the low-frequency perturbations, with frequencies associated with changes in the resonant combination of mean longitudes $5\lambda_U - 3\lambda_A$ and the longitudes of pericenter $\tilde{\omega}_i$. The high-frequency contributions associated with the motions of the mean anomalies and with other nonresonant combinations of the mean anomalies are removed by averaging. The Delaunay momenta $L_i \approx m_i\sqrt{GMa_i}$ and $G_i = L_i\sqrt{1 - e_i^2}$ are conjugate to the mean anomalies and arguments of pericenter, respectively. Canonical Poincaré elements are defined as the coordinate angles $\lambda_i = l_i + \tilde{\omega}_i$, which are conjugate to $L'_i = L_i$, and $\omega_{1i} = -\tilde{\omega}_i$, which are conjugate to $\rho_{1i} = L_i - G_i$. We use the generating function

$$F = \frac{1}{2}(5\lambda_U - 3\lambda_A + 2\omega_{1A})\Sigma_A + \frac{1}{2}(5\lambda_U - 3\lambda_A + 2\omega_{1U})\Sigma_U + \lambda_A\Gamma_A + \lambda_U\Gamma_U \quad (33)$$

to obtain the new resonance coordinates

$$\sigma_A = \frac{1}{2}(5\lambda_U - 3\lambda_A + 2\omega_{1A})$$

$$\sigma_U = \frac{1}{2}(5\lambda_U - 3\lambda_A + 2\omega_{1U}) \quad (34)$$

which together with $\gamma_A = \lambda_A$ and $\gamma_U = \lambda_U$ form a complete set of generalized coordinates.

The momenta conjugate to σ_A and σ_U are

$$\Sigma_A = \rho_{1A} = L'_A - G_A$$

$$\Sigma_U = \rho_{1U} = L'_U - G_U. \quad (35)$$

The momenta conjugate to γ_A and γ_U form two integrals of motion, since in the new variables the resonant Hamiltonian is cyclic in these variables. These resonance integrals are

$$\Gamma_A = L'_A + \frac{3}{2}(\Sigma_A + \Sigma_U)$$

$$\Gamma_U = L'_U - \frac{5}{2}(\Sigma_A + \Sigma_U). \quad (36)$$

Note that $\Sigma_i \approx \Gamma_i e_i^2/2$. The lowest order terms in the disturbing function which influence the evolution of the eccentricities and pericenter longitudes are of order e_i^2. The Hamiltonian is now expanded in powers of Σ_i/Γ_i to this order, and constant terms are removed. The resulting expression in terms of the new coordinates is

$$\begin{aligned}\mathcal{H} = {} & 2A(\Sigma_A + \Sigma_U) + 4B(\Sigma_A + \Sigma_U)^2 \\ & + 2C\Sigma_A + 2D\Sigma_U \\ & + 2E\sqrt{\Sigma_A\Sigma_U}\cos(\sigma_A - \sigma_U) \\ & + 2F\Sigma_A \cos(2\sigma_A) \\ & + 2G\sqrt{\Sigma_A\Sigma_U}\cos(\sigma_A + \sigma_U) \\ & + 2H\Sigma_U \cos(2\sigma_U),\end{aligned} \tag{37}$$

where

$$A = -\frac{3}{4}\frac{G^2M^2m_A^2m_A'}{\Gamma_A^3} + \frac{5}{4}\frac{G^2M^2m_U^2m_U'}{\Gamma_U^3}$$

$$B = -\frac{27}{32}\frac{G^2M^2m_A^2m_A'}{\Gamma_A^4} - \frac{75}{32}\frac{G^2M^2m_U^2m_U'}{\Gamma_U^4}$$

$$\begin{aligned}C = {} & \frac{1}{2}G^4M^4R^2J_2\left[\frac{15m_U^4m_U'^3}{2\Gamma_U^7} - \frac{6m_A^4m_A'^3}{\Gamma_A^7}\right] \\ & + \frac{G^2Mm_Am_U^2m_U'}{4\Gamma_U^2}\left[\frac{5}{\Gamma_U}b_{1/2}^0(\alpha)\right. \\ & \left. + \frac{d}{d\alpha}b_{1/2}^0(\alpha)\frac{m_U}{m_A}\frac{m_U'}{m_A'}\left(\frac{3\Gamma_A}{\Gamma_U^2} + \frac{5\Gamma_A^2}{\Gamma_U^3}\right) - \frac{(2)^{(0)}}{\Gamma_A}\right]\end{aligned}$$

$$\begin{aligned}D = {} & \frac{1}{2}G^4M^4R^2J_2\left[\frac{6m_U^4m_U'^3}{\Gamma_U^7} - \frac{9m_A^4m_A'^3}{2\Gamma_A^7}\right] \\ & + \frac{G^2Mm_Am_U^2m_U'}{4\Gamma_U^2}\left[\frac{5}{\Gamma_U}b_{1/2}^0(\alpha)\right. \\ & \left. + \frac{d}{d\alpha}b_{1/2}^0(\alpha)\frac{m_U}{m_A}\frac{m_U'}{m_A'}\left(\frac{3\Gamma_A}{\Gamma_U^2} + \frac{5\Gamma_A^2}{\Gamma_U^3}\right) - \frac{(3)^{(0)}}{\Gamma_U}\right]\end{aligned}$$

$$E = -\frac{G^2Mm_Am_U^2m_U'}{4\Gamma_U^2\sqrt{\Gamma_A\Gamma_U}}(21)^{(-1)}$$

$$F = -\frac{G^2Mm_Am_U^2m_U'}{4\Gamma_U^2\Gamma_A}(172)^{(5)}$$

$$G = -\frac{G^2Mm_Am_U^2m_U'}{4\Gamma_U^2\sqrt{\Gamma_A\Gamma_U}}(182)^{(4)}$$

$$H = -\frac{G^2Mm_Am_U^2m_U'}{4\Gamma_U^3}(192)^{(3)} \tag{38}$$

where the m_i' are reduced masses in the Jacobi coordinate system (see, e.g., Plummer 1960).

Finally, the transformation to canonical coordinates

$$y_i = \sqrt{2\Sigma_i}\sin(\sigma_i) \approx e_i\sqrt{\Gamma_i}\sin(\sigma_i) \tag{39}$$

and the conjugate momenta

$$x_i = \sqrt{2\Sigma_i}\cos(\sigma_i) \approx e_i\sqrt{\Gamma_i}\cos(\sigma_i) \tag{40}$$

is made, resulting in the final form of the Hamiltonian,

$$\begin{aligned}\mathcal{H} = &\frac{1}{4}(\delta - 2(C + D))(x_A^2 + y_A^2 + x_U^2 + y_U^2) \\ &+ B(x_A^2 + y_A^2 + x_U^2 + y_U^2)^2 \\ &+ C(x_A^2 + y_A^2) + D(x_U^2 + y_U^2) \\ &+ E(x_A x_U + y_A y_U) + F(x_A^2 - y_A^2) \\ &+ G(x_A x_U - y_A y_U) + H(x_U^2 - y_U^2),\end{aligned} \tag{41}$$

which has 2 degrees of freedom.

The units chosen are as follows: distance is measured in units of the radius of Uranus R, mass is measured in units of the mass of Uranus M, and time is measured in years. The coefficients were evaluated at $\delta = 0$ for $e_i = 0$ and $a_U = 10.0703R$. (The semimajor axis at resonance encounter is $a_U = 10.1353$. This should properly have been used in the evaluation of the coefficients; the differences are not significant.) The numerical values for the coefficients thus obtained are

$$\begin{aligned}B &= -2632.82 \\ C &= -0.0803237 \\ D &= -0.0477658 \\ E &= 0.0109693 \\ F &= -0.0319666 \\ G &= 0.0797229 \\ H &= -0.0493825\end{aligned} \tag{42}$$

and the integrals of motion are

$$\begin{aligned}\Gamma_A &= 0.742492 \\ \Gamma_U &= 0.834860.\end{aligned} \tag{43}$$

The state of a system is determined by its coordinates x_i and y_i and the two parameters δ and the numerical value of the Hamiltonian $\mathcal{E}$.

7. APPENDIX II

Planar Mapping

In developing the algebraic mapping, Eq. (37) is rewritten

$$\begin{aligned}\mathcal{H} = &2A(\Sigma_A + \Sigma_U) + 4B(\Sigma_A + \Sigma_U)^2 + 2C\Sigma_A + 2D\Sigma_U \\ &+ 2E\sqrt{\Sigma_A\Sigma_U}\cos(\sigma_A - \sigma_U)\sum_{n=-\infty}^{\infty}\cos n(\Omega t - \phi_1) \\ &+ 2F\Sigma_A\cos(2\sigma_A)\sum_{n=-\infty}^{\infty}\cos n(\Omega t - \phi_2) \\ &+ 2G\sqrt{\Sigma_A\Sigma_U}\cos(\sigma_A + \sigma_U)\sum_{n=-\infty}^{\infty}\cos n(\Omega t - \phi_3) \\ &+ 2H\Sigma_U\cos(2\sigma_U)\sum_{n=-\infty}^{\infty}\cos n(\Omega t - \phi_4).\end{aligned} \tag{44}$$

Expressing the cosine terms using the Fourier representation of the Dirac delta function yields

$$\begin{aligned}\mathcal{H} = &2A(\Sigma_A + \Sigma_U) + 4B(\Sigma_A + \Sigma_U)^2 + 2C\Sigma_A + 2D\Sigma_U \\ &+ 2E\sqrt{\Sigma_A\Sigma_U}\cos(\sigma_A - \sigma_U)2\pi\delta_T(\Omega t - \phi_1) \\ &+ 2F\Sigma_A\cos(2\sigma_A)2\pi\delta_T(\Omega t - \phi_2) \\ &+ 2G\sqrt{\Sigma_A\Sigma_U}\cos(\sigma_A + \sigma_U)\,2\pi\delta_T(\Omega t - \phi_3) \\ &+ 2H\Sigma_U\cos(2\sigma_U)2\pi\delta_T(\Omega t - \phi_4).\end{aligned} \tag{45}$$

This form allows us to integrate the angle-dependent terms at singular points, and integrate the contributions from the other terms between them. The delta functions are periodic in $T = 2\pi/\Omega$, which becomes one cycle of the mapping. During one mapping cycle, the delta functions are integrated at times related to the phases ϕ_i, and between them the secular terms are integrated. These integrations are all performed analytically.

Since the new high-frequency terms are not directly related to those removed by averaging, the choice of the mapping frequency Ω and the phases ϕ_i is largely arbitrary. However, for the mapping to be valid, Ω must be much higher than the long-period frequencies, which are of order 10^{-4} of the orbital frequencies. An $\Omega = 20$ year^{-1} has been found to be suitable for most purposes. This is of order a few hundred times the secular frequencies in this problem. We have chosen $\phi_1 = 0$, $\phi_2 = \phi_4 = \pi/4$ (since these two are independent), and $\phi_s = \pi/2$.

A full mapping cycle involves the following steps, starting with coordinates $x_A^{(0)}$, $y_A^{(0)}$, $x_U^{(0)}$, and $y_U^{(0)}$:

Step 1. Integrate across first delta function at $t = t_1$

$$\begin{aligned}
x_A^{(1)} &= x_A^{(0)} \cos\left(\frac{2\pi E}{\Omega}\right) - y_U^{(0)} \sin\left(\frac{2\pi E}{\Omega}\right) \\
y_A^{(1)} &= y_A^{(0)} \cos\left(\frac{2\pi E}{\Omega}\right) + x_U^{(0)} \sin\left(\frac{2\pi E}{\Omega}\right) \\
x_U^{(1)} &= x_U^{(0)} \cos\left(\frac{2\pi E}{\Omega}\right) - y_A^{(0)} \sin\left(\frac{2\pi E}{\Omega}\right) \\
y_U^{(1)} &= y_U^{(0)} \cos\left(\frac{2\pi E}{\Omega}\right) + x_A^{(0)} \sin\left(\frac{2\pi E}{\Omega}\right).
\end{aligned} \tag{46}$$

Step 2. Integrate secular part from $t = t_1$ to $t = t_2 = t_1 + \phi_2/\Omega$

$$\begin{aligned}
x_A^{(2)} &= x_A^{(1)} \cos\left\{\left[\frac{\delta}{2} + (C - D) + 4B(x_A^{(1)2} + y_A^{(1)2} + x_U^{(1)2} + y_U^{(1)2})\right]\left(\frac{\phi_2 - \phi_1}{\Omega}\right)\right\} \\
&\quad - y_A^{(1)} \sin\left\{\left[\frac{\delta}{2} + (C - D) + 4B(x_A^{(1)2} + y_A^{(1)2} + x_U^{(1)2} + y_U^{(1)2})\right]\left(\frac{\phi_2 - \phi_1}{\Omega}\right)\right\} \\
y_A^{(2)} &= y_A^{(1)} \cos\left\{\left[\frac{\delta}{2} + (C - D) + 4B(x_A^{(1)2} + y_A^{(1)2} + x_U^{(1)2} + y_U^{(1)2})\right]\left(\frac{\phi_2 - \phi_1}{\Omega}\right)\right\} \\
&\quad - x_A^{(1)} \sin\left\{\left[\frac{\delta}{2} + (C - D) + 4B(x_A^{(1)2} + y_A^{(1)2} + x_U^{(1)2} + y_U^{(1)2})\right]\left(\frac{\phi_2 - \phi_1}{\Omega}\right)\right\} \\
x_U^{(2)} &= x_U^{(1)} \cos\left\{\left[\frac{\delta}{2} - (C - D) + 4B(x_A^{(1)2} + y_A^{(1)2} + x_U^{(1)2} + y_U^{(1)2})\right]\left(\frac{\phi_2 - \phi_1}{\Omega}\right)\right\} \\
&\quad - y_U^{(1)} \sin\left\{\left[\frac{\delta}{2} - (C - D) + 4B(x_A^{(1)2} + y_A^{(1)2} + x_U^{(1)2} + y_U^{(1)2})\right]\left(\frac{\phi_2 - \phi_1}{\Omega}\right)\right\} \\
y_U^{(2)} &= y_U^{(1)} \cos\left\{\left[\frac{\delta}{2} - (C - D) + 4B(x_A^{(1)2} + y_A^{(1)2} + x_U^{(1)2} + y_U^{(1)2})\right]\left(\frac{\phi_2 - \phi_1}{\Omega}\right)\right\} \\
&\quad + x_U^{(1)} \sin\left\{\left[\frac{\delta}{2} - (C - D) + 4B(x_A^{(1)2} + y_A^{(1)2} + x_U^{(1)2} + y_U^{(1)2})\right]\left(\frac{\phi_2 - \phi_1}{\Omega}\right)\right\}.
\end{aligned} \tag{47}$$

Step 3. Integrate across second and fourth delta function at $t = t_2 = \phi_2/\Omega$

$$\begin{aligned}
x_A^{(3)} &= x_A^{(2)} \frac{1}{2}(e^{4\pi F/\Omega} + e^{-4\pi F/\Omega}) + y_A^{(2)} \frac{1}{2}(e^{4\pi F/\Omega} - e^{-4\pi F/\Omega}) \\
y_A^{(3)} &= y_A^{(2)} \frac{1}{2}(e^{4\pi F/\Omega} + e^{-4\pi F/\Omega}) + x_A^{(2)} \frac{1}{2}(e^{4\pi F/\Omega} - e^{-4\pi F/\Omega}) \\
x_U^{(3)} &= x_U^{(2)} \frac{1}{2}(e^{4\pi H/\Omega} + e^{-4\pi H/\Omega}) + y_U^{(2)} \frac{1}{2}(e^{4\pi H/\Omega} - e^{-4\pi H/\Omega}) \\
y_U^{(3)} &= y_U^{(2)} \frac{1}{2}(e^{4\pi H/\Omega} + e^{-4\pi H/\Omega}) + x_U^{(2)} \frac{1}{2}(e^{4\pi H/\Omega} - e^{-4\pi H/\Omega}).
\end{aligned} \tag{48}$$

Step 4. Integrate secular part between t_2 and $t = t_3 = t_2 + (\phi_3 - \phi_2)/\Omega$.

Step 5. Integrate across third delta function at $t = t_3 = \phi_3/\Omega$

$$
\begin{aligned}
x_A^{(5)} &= x_A^{(4)} \frac{1}{2}(e^{4\pi G/\Omega} + e^{-4\pi G/\Omega}) + y_U^{(4)} \frac{1}{2}(e^{4\pi G/\Omega} - e^{-4\pi G/\Omega}) \\
y_A^{(5)} &= y_A^{(4)} \frac{1}{2}(e^{4\pi G/\Omega} + e^{-4\pi G/\Omega}) + x_U^{(4)} \frac{1}{2}(e^{4\pi G/\Omega} - e^{-4\pi G/\Omega}) \\
x_U^{(5)} &= x_U^{(4)} \frac{1}{2}(e^{4\pi G/\Omega} + e^{-4\pi G/\Omega}) + y_A^{(4)} \frac{1}{2}(e^{4\pi G/\Omega} - e^{-4\pi G/\Omega}) \\
y_U^{(5)} &= y_U^{(4)} \frac{1}{2}(e^{4\pi G/\Omega} + e^{-4\pi G/\Omega}) + x_A^{(4)} \frac{1}{2}(e^{4\pi G/\Omega} - e^{-4\pi G/\Omega}). \qquad (49)
\end{aligned}
$$

Step 6. Integrate secular part between t_3 and $t = t_4 = t_0 + 2\pi/\Omega$. This full cycle of the mapping iterates all coordinates forward in time by one mapping period $T = 2\pi/\Omega$.

If tidal dissipation is included, the mapping becomes explicitly time dependent through $\delta(t)$ and also through a slightly more complicated secular evolution. The secular evolution is integrated assuming a linear dependence of δ on time.

Since the mapping includes high-frequency perturbations, the averaged Hamiltonian is no longer a conserved quantity. We require a conserved quantity corresponding to the energy for the analysis of Section 4.2. In addition, if the mapping is used to compute a surface of section according to the standard criteria for the averaged Hamiltonian, there will be a slight distortion due to the difference between the mapping coordinates and the averaged coordinates. For these reasons, we have used perturbation theory to transform from mapping coordinates to averaged coordinates, by removing the new high-frequency perturbations (see Wisdom and Tittemore 1987).

We use a Von Zeipel transformation to go from mapping coordinates to averaged coordinates, using the generating function

$$F = \sum_i \Sigma_i' \sigma_i + \mu S(\Sigma_i', \sigma_i, t) \qquad (50)$$

and the transformation to first order in μ

$$
\begin{aligned}
\Sigma_i &= \Sigma_i' + \mu \frac{\partial S}{\partial \sigma_i} \\
\sigma_i' &= \sigma_i + \mu \frac{\partial S}{\partial \Sigma_i'} \qquad (51)
\end{aligned}
$$

The Hamiltonian (44) can be expressed

$$\mathcal{H} = \mathcal{H}_0(\Sigma_i) + \mu \bar{\mathcal{H}}_1(\Sigma_i, \sigma_i) + \mu \tilde{\mathcal{H}}_1(\Sigma_i, \sigma_i, t), \qquad (52)$$

where $\tilde{\mathcal{H}}_1$ contains time-dependent terms ($n \neq 0$) in Eq. (44).

To first order in μ, this Hamiltonian becomes

$$
\begin{aligned}
\mathcal{H}' &= \mathcal{H}_0(\Sigma_i(\Sigma_i')) + \mu \bar{\mathcal{H}}_1(\Sigma_i', \sigma_i') + \mu \tilde{\mathcal{H}}_1(\Sigma_i', \sigma_i', t) + \mu \frac{\partial S}{\partial t} \\
&= \mathcal{H}_0(\Sigma_i') + \mu \bar{\mathcal{H}}_1(\Sigma_i', \sigma_i') + \mu \tilde{\mathcal{H}}_1(\Sigma_i', \sigma_i', t) + \mu \frac{\partial S}{\partial t} \\
&\quad + \mu \frac{\partial S}{\partial \sigma_A'} \left[\frac{\delta}{2} + (C - D) + 8B(\Sigma_A' + \Sigma_U') \right] \\
&\quad + \mu \frac{\partial S}{\partial \sigma_U'} \left[\frac{\delta}{2} - (C - D) + 8B(\Sigma_A' + \Sigma_U') \right]. \qquad (53)
\end{aligned}
$$

S is chosen to eliminate time-dependent terms, so that

$$\mu\mathcal{H}_1(\Sigma_i',\sigma_i',t) + \mu\frac{\partial S}{\partial t} + \mu\frac{\partial S}{\partial \sigma_A'}\left[\frac{\delta}{2} + (C-D) + 8B(\Sigma_A' + \Sigma_U')\right] + \mu\frac{\partial S}{\partial \sigma_U'}\left[\frac{\delta}{2} - (C-D) + 8B(\Sigma_A' + \Sigma_U')\right] = 0. \tag{54}$$

Since

$$\mathcal{H}_1 = \sum_{ij} A_{ij}\cos(i\sigma_A + j\sigma_U)\sum_{n\neq 0}\cos n(\Omega t - \phi_{ij})$$

$$= \sum_{ij} A_{ij}\sum_{n\neq 0}\cos(i\sigma_A + j\sigma_U) + n(\Omega t - \phi_{ij})) \tag{55}$$

then

$$S = -\sum_{ij} A_{ij}\sum_{n\neq 0}\frac{\sin(i\sigma_A + j\sigma_U + n(\Omega t + \phi_{ij}))}{Z + n\Omega} \tag{56}$$

or

$$\begin{aligned} S = &-2E\sqrt{\Sigma_A'\Sigma_U'}\,[K(1,-1)\sin(\sigma_A' - \sigma_U') + L(1,-1)\cos(\sigma_A' - \sigma_U')] \\ &-2F\Sigma_A'\,[K(2,0)\sin(2\sigma_A') + L(2,0)\cos(2\sigma_A')] \\ &-2G\sqrt{\Sigma_A'\Sigma_U'}\,[K(1,1)\sin(\sigma_A' + \sigma_U') + L(1,1)\cos(\sigma_A' + \sigma_U')] \\ &-2H\Sigma_U'\,[K(0,2)\sin(2\sigma_U') + L(0,2)\cos(2\sigma_U')] \end{aligned} \tag{57}$$

with the functions

$$K(i,j) = \frac{\pi}{\Omega}\frac{\cos(z/\Omega)(\Omega t - \phi_{ij} - \pi)}{\sin(Z/\Omega)\pi} - \frac{1}{Z}$$

$$L(i,j) = -\frac{\pi}{\Omega}\frac{\sin(z/\Omega)(\Omega t - \phi_{ij} - \pi)}{\sin(Z/\Omega)\pi} \tag{58}$$

evaluated at $t = 2\pi/\Omega$, where

$$Z = i\left[\frac{\delta}{2} + (C-D) + 8B(\Sigma_A' + \Sigma_U')\right] - j\left[\frac{\delta}{2} - (C-D) + 8B(\Sigma_A' + \Sigma_U')\right] \tag{59}$$

and i and j refer, respectively, to the coefficients of σ_A and σ_U. ϕ_{ij} are the phases from Eq. (44).

To first order in μ, the transformation from map coordinates to averaged coordinates is just

$$x_i^{av} = \left(1 - \frac{1}{2}\mu\frac{\partial S/\partial\sigma_i}{\Sigma_i}\right)\left[x_i^m\cos\left(\mu\frac{\partial S}{\partial\Sigma_i}\right) - y_i^m\sin\left(\mu\frac{\partial S}{\partial\Sigma_i}\right)\right]$$

$$y_i^{av} = \left(1 - \frac{1}{2}\mu\frac{\partial S/\partial\sigma_i}{\Sigma_i}\right)\left[y_i^m\cos\left(\mu\frac{\partial S}{\partial\Sigma_i}\right) + x_i^m\sin\left(\mu\frac{\partial S}{\partial\Sigma_i}\right)\right] \tag{60}$$

which is a slight rotation and change of scale.

8. APPENDIX III

STANDARD THEORY OF EVOLUTION THROUGH RESONANCES

In this appendix we shall examine evolution into two of the second-order resonances at the 5 : 3 Ariel–Umbriel commensurability. We treat for the moment these resonances as isolated resonances in order to verify that our numerical methods are in satisfactory agreement with the results of the isolated single resonance model when the model is applicable. We emphasize that this is being undertaken only to verify our methods; the actual dynamics near the 5 : 3 commensurability are much more complicated, with the presence of large chaotic zones in the phase space, and the single resonance model is not applicable.

8.1. Adiabatic Invariance

The theory of adiabatic invariance can be used to completely specify the evolution of a one degree of freedom Hamiltonian problem with a slowly varying parameter δ, in the absence of infinite period orbits (separatrices) and/or chaotic zones. (Because of the time dependence of the parameter δ the problem is nonautonomous and separatrices and chaotic zones are strictly speaking practically everywhere, though most are too small to be important (see Chirikov 1979).) For a one degree of freedom problem the adiabatic invariant is, to first order, the action J, which is defined for fixed δ in terms of generalized canonical coordinates p and q as

$$J = \oint p dq \tag{61}$$

or the area on the phase plane enclosed by the trajectory. For fixed δ the action is strictly conserved since trajectories follow level curves of the Hamiltonian for a one degree of freedom system. In action angle variables, the Hamiltonian is cyclic in the angle conjugate to the action:

$$\mathcal{H}(p,q;\delta) \Rightarrow \mathcal{H}(J;\delta). \tag{62}$$

Evolution of the parameter δ at some slow rate $\dot{\delta} = \varepsilon$ can be considered a perturbation on the motion. By transforming to action-angle coordinates and averaging over the period of motion on the trajectory, which is in general much shorter than the time scale of the evolution of δ, it can be shown that the action is to first order invariant (see, e.g., Born 1960, Arnold 1978, Landau and Lifshitz 1978). It has also been shown that there is an adiabatic invariant to all orders in ε, if ε is sufficiently small (Lenard 1959, Kruskal 1962, Arnold 1963). To first order then the evolution of the energy depends only on the form in which δ appears in the Hamiltonian in action angle variables:

$$\mathcal{H}(t) = \mathcal{H}(\delta(t)). \tag{63}$$

The evolution of trajectories defined by the Hamiltonian as δ varies can be viewed as slow changes in the level curves of $\mathcal{H}$, maintaining constant area on the phase plane.

The standard theory of evolution through resonances (Goldreich and Peale 1966, Yoder 1979, Henrard 1982, 1987, Henrard and Lemaitre 1983, Borderies and Goldreich 1984, Lemaitre 1984, Peale 1986) treats the resonances arising from a commensurability independently. This approximation may be valid for mean-motion resonances, for instance, if the J_2 of the planet is large, and has been successfully applied to $J : J + 1$ resonant motions in the satellite system of Saturn (Yoder 1979, Peale 1976, Henrard and Lemaitre 1983).

We consider here two of the second-order eccentricity resonances at the 5 : 3 Ariel–Umbriel commensurability: the resonance proportional to the square of the eccentricity of Ariel and the resonance proportional to he square of the eccentricity of Umbriel. The Hamiltonians for these two resonances, artificially treated as though they are isolated, are

$$\mathcal{H}_A = \left[\frac{\delta}{2} + (C - D)\right] \Sigma_A + 4B\Sigma_A^2 + 2F\Sigma_A \cos(2\sigma_A)$$
$$= \frac{1}{2}\left[\frac{\delta}{2} + (C - D)\right](x_A^2 + y_A^2) + B(x_A^2 + y_A^2)^2 + F(x_A^2 - y_A^2) \quad (64)$$

and

$$\mathcal{H}_U = \left[\frac{\delta}{2} - (C - D)\right] \Sigma_U + 4B\Sigma_U^2 + 2H\Sigma_U \cos(2\sigma_U)$$
$$= \frac{1}{2}\left[\frac{\delta}{2} - (C - D)\right](x_U^2 + y_U^2) + B(x_U^2 + y_U^2)^2 + H(x_U^2 - y_U^2) \quad (65)$$

These can be derived by removing the coupling terms from the full Hamiltonian (6) and (9). These are both one degree of freedom problems, and are therefore integrable. The mixed second-order resonance could of course be treated in a similar manner, but will not be considered here.

The structure of the level curves of the Hamiltonian for second-order resonances is well known. Figure 29 illustrates the level curves of these systems for various fixed values of δ, computed with the mapping. For large negative δ, or before the resonance is encountered, the curves in x_i, y_i space are approximately concentric circles surrounding a stable fixed point at the origin, and the eccentricity is approximately constant. As the value of δ is increased, curves near the origin become distorted in the y-direction. At a critical value of δ_{c1} a period-2 bifurcation of the fixed point occurs, and it becomes unstable. There are now two librating islands surrounding stable fixed points on the y-axis, bounded by a separatrix with a "figure 8" shape. As δ increases, these islands become larger. At a second critical value of δ_{c2}, another bifurcation occurs at the origin. The fixed point at the origin becomes stable again and is surrounded by concentric level curves. Two unstable equilibria are emitted from the origin. The separatrix now resembles two "bananas" joined at the "ends." Further evolution of δ results in these islands moving further from the origin, and the trajectories near the origin become more circular. Critical values of δ and coordinates of stable and unstable fixed points are summarized in Table IV.

For the physical system trajectories encounter the resonance as δ passes from large negative values through values near zero. The semimajor axis of the inner satellite Ariel is increasing more rapidly than that of Umbriel. The ratio of their semimajor axes, a_A/a_U is increasing. For this direction of passage through an isolated second-order resonance the trajectory may be either captured into resonance or escape

TABLE IV

SINGLE RESONANCES

Ariel resonance

$\delta_{c1} = -2(C - D) + 4F = -0.065$
$\delta_{c2} = -2(C - D) - 4F = 0.193$

Unstable equilibria:

$x_1^2 = 0.0,\ \delta_{c1} \leq \delta < \delta_{c2}$

$$x_1^2 = -\frac{[\delta + 2(C - D) + 4F]}{8B},\ \delta \geq \delta_{c2}$$

Stable equilibria:

$$y_1^2 = -\frac{[\delta + 2(C - D) - 4F]}{8B},\ \delta \geq \delta_{c1}$$

Umbriel resonance

$\delta_{c1} = 2(C - D) + 4H = -0.263$
$\delta_{c2} = 2(C - D) - 4H = 0.133$

Unstable equilibria:

$x_2^2 = 0.0,\ \delta_{c1} \leq \delta < \delta_{c2}$

$$x_2^2 = -\frac{[\delta - 2(C - D) + 4H]}{8B},\ \delta \geq \delta_{c2}$$

Stable equilibria:

$$y_2^2 = -\frac{[\delta - 2(C - D) - 4H]}{8B},\ \delta \geq \delta_{c1}$$

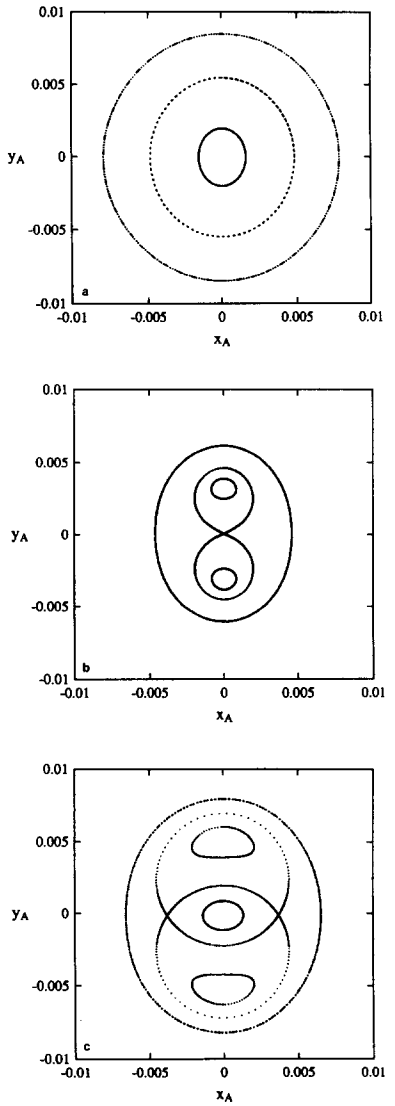

FIG. 29. Level curves for the Ariel (e_A^2) resonance, computed with the uncoupled mapping. (a) $\delta = -0.5$, (b) $\delta = 0.15$, (c) $\delta = 0.5$.

from resonance. If the separatrix is encountered with $\delta_{c1} \leq \delta \leq \delta_{c2}$ then capture is certain. This occurs for trajectories with small eccentricity. If the separatrix is encountered with larger values of δ then the trajectory may either be captured or escape. The adiabatic invariance theory breaks down as the trajectory approaches the separatrix, since the period of motion on the separatrix is infinite, and it is no longer proper to average the evolution over the libration period. The action (area inside a trajectory) changes discontinuously on passage through the separatrix, which can be seen on inspection of Fig. 29. Trajectories which escape have lower eccentricities than they had approaching the resonance. The eccentricities of captured trajectories increase until the damping rate due to tidal dissipation in the satellite becomes comparable to the input of energy to the orbits.

The evolution of the energy (the numerical value of the Hamiltonian) of a trajectory can be estimated from the eccentricity behavior of the various cases, summarized in Table IV. Interior to the resonance ($\delta \ll 0$), the level curves are roughly circular, and adiabatic invariance of the area enclosed by the curves results in the eccentricities remaining approximately constant as δ changes. Therefore $\mathcal{H}_A$ and $\mathcal{H}_U$ are linearly proportional to δ, and the energies increase linearly with time. The same is true for trajectories which escape. The change in eccentricity at the point of escape causes the slope of $\mathcal{H}_i$ to decrease discontinuously at the value of δ where the separatrix is crossed. For captured trajectories, the eccentricity increases approximately as $\sqrt{\delta}$. The functions $\mathcal{H}_A$ and $\mathcal{H}_U$ are quartic in eccentricity. Therefore, the energy increase is roughly quadratic in time.

Evolution of trajectories in δ, ΔE space for the single resonance Hamiltonians are much simpler than for the full resonant Hamiltonian. Since only two fates are possible, trajectories will follow one of only two branches in δ, ΔE space for values of δ larger than that at which the separatrix is crossed. If the trajectory is captured into the resonance, ΔE will increase linearly. If it escapes, ΔE will decrease quadratically.

The energies of the separatrices for $\mathcal{H}_A$ and $\mathcal{H}_U$ are shown in Fig. 1. Expressions for these energies have been obtained by substituting the coordinates of the unstable fixed points as a function of δ (see Table IV) in Eqs. (64) and (65).

8.2. Capture Probabilities

The determination of the fate of a given trajectory upon an encounter with an isolated resonance has been developed in a probabilistic approach based on the "balance of energy" as the trajectory crosses the separatrix (Goldreich and Peale 1966, Counselman and Shapiro 1970, Yoder 1979, Henrard 1982, 1987, Henrard and Lemaitre 1983, Borderies and Goldreich 1984, Lemaitre 1984). The balance of energy is defined as the difference between the change in energy of the trajectory and the change in energy of the separatrix in one cycle of the trajectory.

The analytic theory of capture into resonance assumes a uniform distribution of trajectory energies just before separatrix crossing. These energies lie within a range corresponding to the energy balance of the outer separatrix B_0. The probabilities of capture and escape depend on the magnitude of the energy balance before transition across the separatrix B_i. A trajectory loses energy relative to the separatrix as it approaches, since the separatrix gains energy quadratically with δ and the trajectory gains energy only linearly with δ. Therefore, B_0 is less than zero. B_i can be either positive or negative. If it is negative, the total relative change in energy is negative, and the trajectory continues losing energy with respect to the separatrix, and escapes. If $B_i > 0$, and $B_i + B_0 < 0$, the same thing happens. However, if $B_i + B_0 > 0$, and there is a net gain in relative energy, capture will occur. The outcome will depend on both the phase and energy of the trajectory relative to the separatrix just before crossing. Since these are generally unknown, only an estimate of the likelihood of various outcomes can be made. Probabilities are assigned under the assumption that the energy of the physical system is equally likely to have been anywhere within the balance of energy. Equivalently, probabilities are assigned by assuming the actual system belongs to an ensemble of similar systems whose energies are distributed uniformly over a range of energies comparable to the balance of energy. Probability of capture is then

$$P_c = \frac{B_0 + B_i}{B_0}, \tag{66}$$

where B_0 and B_i are estimated at a given value of δ by approximating the motion as motion on the separatrix. By distributing the energies of trajectories uniformly through the range B_0, one should obtain a representative sample of trajectories with both fates.

The balance of energy has been approximated by Henrard (1987) as the rate of increase of the area in phase space enclosed by the separatrix at the value of δ at which the trajectory crosses the separatrix:

$$B \simeq -\dot{\delta}\frac{\partial J^*}{\partial \delta}, \tag{67}$$

where J^* is the area enclosed by the separatrix. The probability of capture, then, is the ratio of the rate of increase of the combined area of the libration islands to the rate of increase of the area enclosed by the outer boundary of the separatrix. This has a nice intuitive interpretation in terms of Liouville's theorem.

When the standard theory is applied to the two $J:J+2$ resonances in our problem treated individually, the probabilities of capture are

$$P_A = \frac{2}{1 + \pi/(2 \sin^{-1}(-2F/\sqrt{-F(\delta + 2(C - D))}))} \tag{68}$$

for the Ariel resonance and

$$P_U = \frac{2}{1 + \pi/(2 \sin^{-1}(-2H/\sqrt{-H(\delta - 2(C - D))}))} \tag{69}$$

for the Umbriel resonance. The value of δ is that at which the trajectory crosses the separatrix.

For $-2(C - D) + 4F \leq \delta \leq -2(C - D) - 4F$, $P_A = 1$, and for $2(C - D) + 4H \leq \delta \leq 2(C - D) - 4H$, $P_U = 1$. For larger values of δ, the dependence of probability on eccentricity far from resonance can be found. The action of a trajectory is to first order adiabatically invariant until just before it crosses the separatrix. At this point, the action is approximately equal to the area enclosed by the outer separatrix, for which analytic expressions can be found,

$$J_A^* = 2\sqrt{\frac{-F(\delta + 2(C - D) - 4F^2)}{16B^2}} - \frac{(\delta + 2(C - D))}{4B}\left[\frac{\pi}{2} + \sin^{-1}\left(\frac{-2F}{\sqrt{-F(\delta + 2(C - D))}}\right)\right], \quad (70)$$

for the Ariel resonance and

$$J_U^* = 2\sqrt{\frac{-H(\delta - 2(C - D) - 4H^2)}{16B^2}} - \frac{(\delta - 2(C - D))}{4B}\left[\frac{\pi}{2} + \sin^{-1}\left(\frac{-2H}{\sqrt{-H(\delta + 2(C - D))}}\right)\right], \quad (71)$$

for the Umbriel resonance.

By considering the trajectories far from resonance to be approximately circular with actions $J_i \simeq 2\pi\Sigma_{io}$, and equating these with the above expressions, the dependence of capture probability on eccentricity far from resonance can be determined. Using the above expressions, $e_A < 0.00404$ and $e_U < 0.00474$ for certain capture, in agreement with the calculations of Peale (1988).

8.3. *Numerical Results*

We have applied the techniques used to study the full resonant problem to a numerical check of the formulas for the standard theory of passage through isolated resonances. We have numerically computed the probability function for a number of sets of 100 trajectories, the trajectories in each set having the same initial eccentricities, but different phases. Different sets have different initial eccentricities. The mapping (44) with all coupling terms set to zero was used. We have taken a number of steps to ensure that various sources of error are under control.

The values predicted for B_0 are estimates. In order to avoid possible "edge effects" by under- or oversampling ranges of B_0 which result in capture or escape, and to ensure that the distribution of phases just before crossing the separatrix is uniform, we have randomly distributed initial energies and phases far from resonance such that near the separatrix the spread in energy is uniform across approximately 100 times the energy balance of the outer separatrix at the value of δ at which it is predicted to cross. This has taken into consideration the approximately linear spread in energies of trajectories with slight initial differences over the range of δ between the initial value and the value at separatrix crossing.

This initial spread in energies corresponds to a spread of initial eccentricities. Because of the variation of capture probability with initial eccentricity in the single resonance model, trajectories at opposite ends of the range of initial eccentricity have slightly different capture probabilities. This contributes some error to the estimate of the probability:

$$\Delta P_c \simeq \Delta e_0 \times \left.\frac{\partial P_c}{\partial e}\right|_{\langle e_0 \rangle}. \quad (72)$$

Since the probability function is known, the expected statistical fluctuation at any point on the function can be estimated using binomial statistics:

$$\Delta P_c = \frac{\sigma}{N} = \sqrt{\frac{P_c(1 - P_c)}{N}}. \quad (73)$$

There is some uncertainty in exact values of energy due to fluctuations in the mapping integral, which are approximately inversely

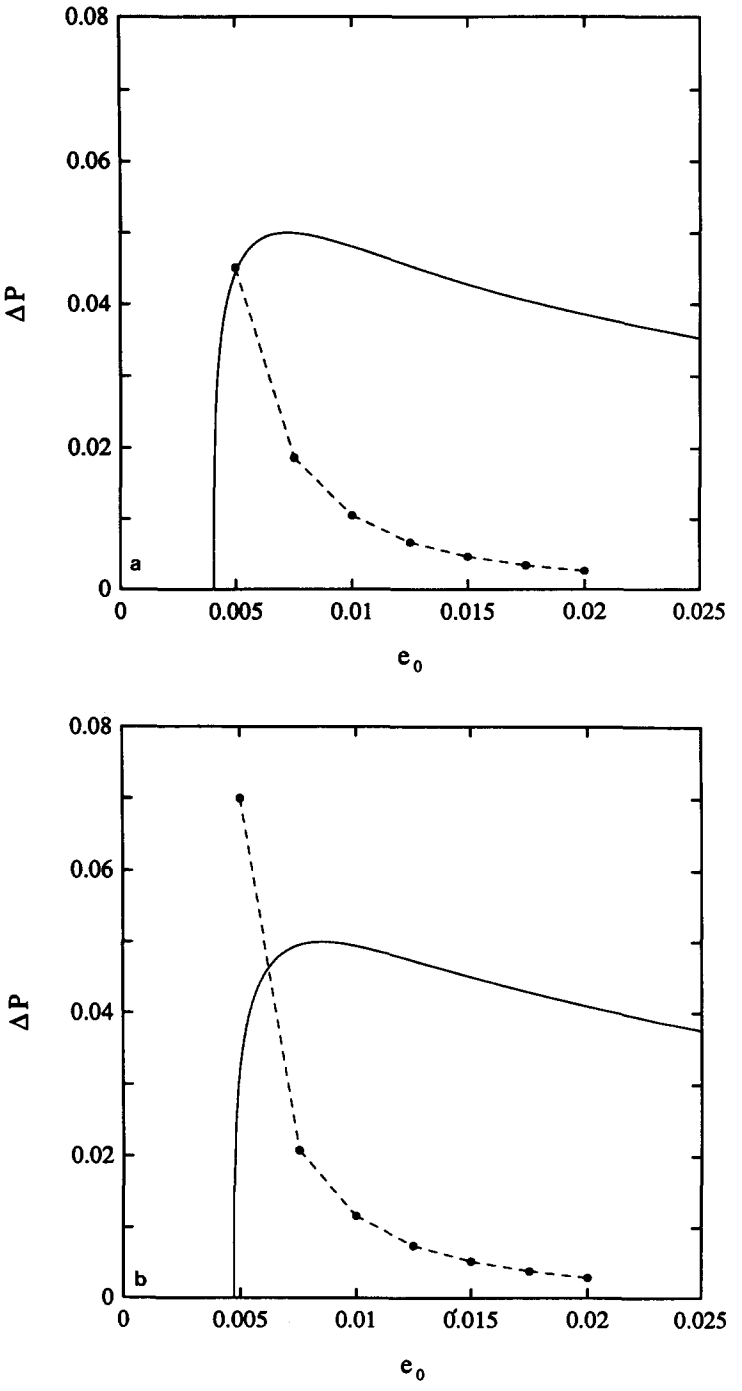

FIG. 30. Expected probability variations in single resonance capture probabilities. (a) Ariel (e_A^2) resonance, (b) Umbriel (e_U^2) resonance. Solid line: expected statistical fluctuation for 100 trajectories. Points: initial spread of eccentricities multiplied by the slope of the probability function.

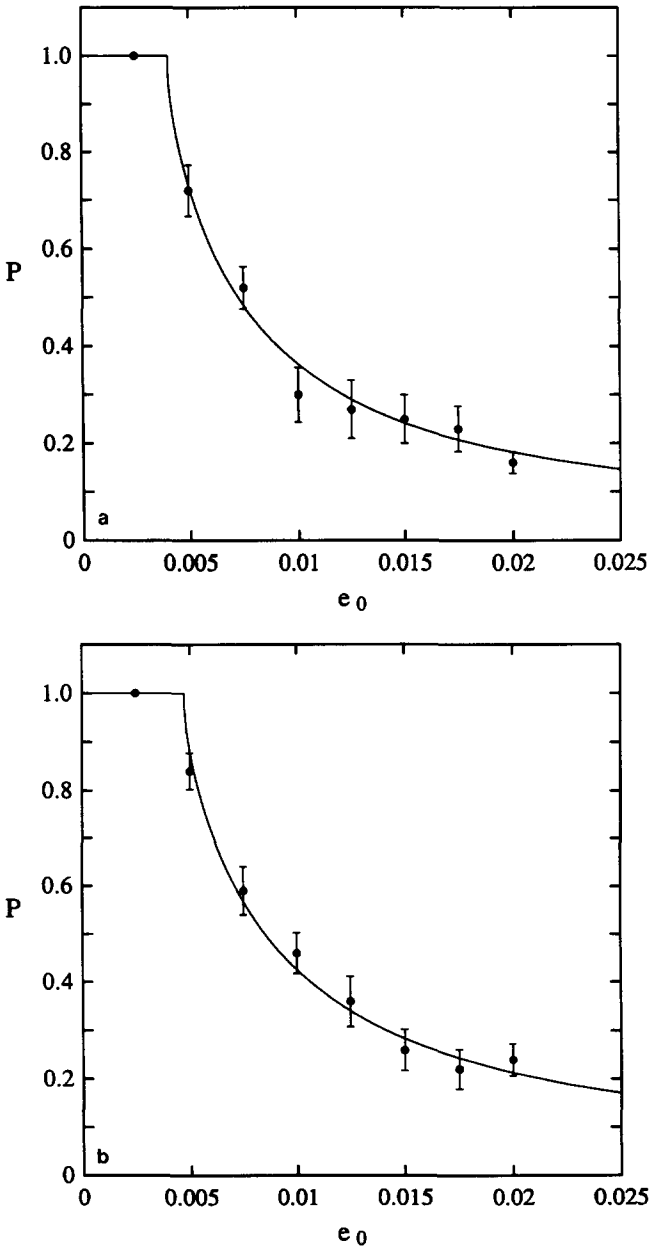

FIG. 31. Single resonance capture probabilities. (a) Ariel (e_A^2) resonance, (b) Umbriel (e_U^2) resonance. Solid lines are theoretical predictions from the single-resonance theory. Data points are measured capture probabilities for ensembles of 100 trajectories evolved through the resonance with the uncoupled mapping. The mapping method properly reproduces the capture probabilities within the range of eccentricities where the approximations concerning the tidal friction are valid (see Section 4.1).

proportional to Ω through the K and L functions (58). $\Omega = 80$ year^{-1} has been chosen to keep the error less than about 1%.

Based on the above discussion, the expected probability errors have been estimated. These are plotted in Fig. 30 for the variation over the probability functions and for the statistical fluctuations. The energy

error is less than about 1%. The statistical fluctuations dominate over most of the range except at the steepest parts of the probability functions.

Numerical measurements of the capture probabilities for both resonances were computed by running sets of 100 trajectories through the resonance using the map, each with the aforementioned energy and phase spreads and $\langle e_0 \rangle$ = 0.0025, 0.005, 0.0075, 0.01, 0.0125, 0.015, 0.0175, and 0.02. Results are plotted in Fig. 31, along with the predictions of the analytic theory. The agreement with the analytical predictions is very good. Measured errors are somewhat less than expected on the steep part of the probability function.

The agreement between our numerical results for these single resonance problems and the expectations from the single resonance model give us confidence that our methods can be used to reliably examine the passage through the more complicated resonances considered in this paper.

ACKNOWLEDGMENTS

It is a pleasure to thank S. J. Peale and G. J. Sussman for numerous friendly conversations and general encouragement, and S. J. Peale for a careful review of the manuscript. This research was supported in part by the NASA Planetary Geology and Geophysics Program under Grant NAGW-706.

REFERENCES

ALLAN, R. R. 1969. Evolution of Mimas–Tethys commensurability. *Astron. J.* **74,** 497–506.

ARNOLD, V. I. 1963. Small denominators and problems of stability of motion in classical and celestial mechanics. *Russian Math. Surv.* **18,** 85–91.

ARNOLD, V. I. 1978. *Mathematical Methods of Classical Mechanics*. Springer-Verlag, New York.

BENETTIN, G., L. GALGANI, AND J. STRELCYN 1976. Kolmogorov entropy and numerical experiments. *Phys. Rev. A* **14,** 2338–2345.

BORDERIES, N., AND P. GOLDREICH 1984. A simple derivation of capture probabilities for the $J + 1:J$ and $J + 2:J$ orbit–orbit resonance problems. *Celest. Mech.* **32,** 127–136.

BORN, M. 1960. *Mechanics of the Atom*. Ungar, New York.

BROUWER, D., AND G. M. CLEMENCE 1961. *Methods of Celestial Mechanics*. Academic Press, New York.

CHIRIKOV, B. V. 1979. A universal instability of many dimensional oscillator systems. *Phys. Rep.* **52,** 263–379.

COUNSELMAN, C. C., AND I. I. SHAPIRO, 1970. Spin–orbit resonance of Mercury. *Symposia Mathematica* **3,** 121–169.

DERMOTT, S. F. 1984. Origin and evolution of the Uranian and Neptunian satellites: Some dynamical considerations. In *Uranus and Neptune* (J. Bergstralh, Ed.), NASA Conference Publication 2330, pp. 377–404.

DERMOTT, S. F., AND P. D. NICHOLSON 1986. Masses of the satellites of Uranus. *Nature* **319,** 115–120.

FRENCH, R. G., J. L. ELLIOT, AND S. L. LEVINE 1985. Structure of the Uranian rings. II. Perturbations of the ring orbits and widths. *Icarus* **67,** 134–163.

GAVRILOV, S. V., AND V. N. ZHARKOV 1977. Love numbers of the giant planets. *Icarus* **32,** 443–449.

GOLDREICH, P. 1963. On the eccentricity of satellite orbits in the Solar System. *Mon. Not. R. Astron. Soc.* **126,** 257–268.

GOLDREICH, P. 1965. An explanation of the frequent occurrence of commensurable mean motions in the Solar System. *Mon. Not. R. Astron. Soc.* **130,** 159–181.

GOLDREICH, P., AND S. J. PEALE 1966. Spin–orbit coupling in the Solar System. *Astron. J.* **71,** 425–438.

HÉNON, M. 1966a. Exploration numérique du problème restreint. III. Masses égales, orbites non périodiques. *Bull. Astron. Paris* **1,** fasc. 1, 57.

HÉNON, M. 1966b. Exploration numérique du problème restreint. IV. Masses égales, orbites non périodiques. *Bull. Astron. Paris* **1,** fasc. 2, 49.

HÉNON, M. 1969. Numerical study of quadratic area-preserving mappings. *Quart. Appl. Math.* **26,** 291–311.

HÉNON, M. 1970. Numerical exploration of the restricted problem. VI. Hill's case: Nonperiodic orbits. *Astron. Astrophys.* **9,** 24–36.

HÉNON, M. 1983. Numerical exploration of Hamiltonian systems. In *Chaotic Behaviour of Dynamical Systems*. North-Holland, Amsterdam.

HÉNON, M., AND C. HEILES 1964. The applicability of the third integral of motion: Some numerical experiments. *Astron. J.* **69,** 73–79.

HENRARD, J. 1982. Capture into resonance: An extension of the use of adiabatic invariants. *Celest. Mech.* **27,** 3–22.

HENRARD, J. 1987. The adiabatic invariant. Submitted for publication.

HENRARD, J., AND A. LEMAITRE 1983. A second fundamental model for resonance. *Celest. Mech.* **30,** 197–218.

KAULA, W. M. 1968. *An Introduction to Planetary Physics: The Terrestrial Planets*. Wiley, New York.

KRUSKAL, M. 1962. Asymptotic theory of Hamiltonian and other systems with all solutions nearly periodic. *J. Math. Phys.* **3,** 806–828.

LANDAU AND LIFSHITZ 1978. *Mechanics*. Pergamon, Elmsford, NY.

LASKAR, J. 1986. A general theory for the Uranian satellites. *Astron. Astrophys.* **166,** 349–358.

LEMAITRE, A. 1984. High-order resonances in the restricted three-body problem. *Celest. Mech.* **32,** 109–126.

LENARD, A. 1959. Adiabatic invariance to all orders. *Ann. Phys.* **6,** 261–276.

LEVERRIER, U.-J. 1855. *Ann. Obs. Paris, Mém.* **1.**

MEYER, K. R. 1970. Generic bifurcation of periodic points. *Trans. Amer. Math. Soc.* **149,** 95–107.

PAUWELS, T. 1983. Secular orbit–orbit resonances between two satellites with non-zero masses. *Celest. Mech.* **30,** 229–247.

PEALE, S. J. 1976. Orbital resonances in the Solar System. *Ann. Rev. Astron. Astrophys.* **14,** 215–245.

PEALE, S. J. 1986. Orbital resonances, unusual configurations, and exotic rotation states among planetary satellites. In *Satellites* (J. Burns and M. Matthews, Eds.), pp. 159–223. Univ. of Arizona Press, Tucson.

PEALE, S. J. 1988. Speculative histories of the Uranian satellite system. *Icarus* **74,** 153–171.

PEALE, S. J., AND P. CASSEN 1978. Contribution of tidal dissipation to lunar thermal history. *Icarus* **36,** 245–269.

PEALE, S. J., P. CASSEN, AND R. T. REYNOLDS 1979. Melting of Io by tidal dissipation. *Science* **203,** 892–894.

PEALE, S. J., P. CASSEN, AND R. T. REYNOLDS 1980. Tidal dissipation, orbital evolution, and the nature of Saturn's inner satellites. *Icarus* **43,** 65–72.

PLESCIA, J. B. 1987. Geological terrains and crater frequencies on Ariel. *Nature* **327,** 201–204.

PLUMMER, H. C. 1960. *An Introductory Treatise on Dynamical Astronomy*. Dover, New York.

REYNOLDS, R. T., AND P. M. CASSEN 1979. On the internal structure of the major satellites of the outer planets. *Geophys. Res. Lett.* **6,** 121–124.

SINCLAIR, A. T. 1972. On the origin of the commensurabilities amongst the satellites of Saturn. *Mon. Not. R. Astron. Soc.* **160,** 169–187.

SINCLAIR, A. T. 1974. On the origin of the commensurabilities amongst the satellites of Saturn—II. *Mon. Not. R. Astron. Soc.* **166,** 165–179.

SMITH, B. A., L. A. SODERBLOM, R. BEEBE, D. BLISS, J. M. BOYCE, A. BRAHIC, G. A. BRIGGS, R. H. BROWN, S. A. COLLINS, A. F. COOK II, S. K. CROFT, J. N. CUZZI, G. E. DANIELSON, M. E. DAVIES, T. E. DOWLING, D. GODFREY, C. J. HANSEN, C. HARRIS, G. E. HUNT, A. P. INGERSOLL, T. V. JOHNSON, R. J. KRAUSS, H. MASURSKY, D. MORRISON, T. OWEN, J. B. PLESCIA, J. B. POLLACK, C. C. PORCO, K. RAGES, C. SAGAN, E. M. SHOEMAKER, L. A. SROMOVSKY, C. STOKER, R. G. STROM, V. E. SUOMI, S. P. SYNNOTT, R. J. TERRILE, P. THOMAS, W. R. THOMPSON, AND J. VEVERKA 1986. Voyager 2 in the Uranian system: Imaging science results. *Science* **233,** 43–64.

SQUYRES, S. W., R. T. REYNOLDS, AND J. J. LISSAUER 1985. The enigma of the Uranian satellites' orbital eccentricities. *Icarus* **61,** 218–233.

STONE, E. C., AND E. D. MINER 1986. The Voyager 2 encounter with the Uranian system. *Science* **233,** 39–43.

TITTEMORE, W. C., AND J. WISDOM 1988. Tidal evolution of the Uranian satellites. II. An explanation of the anomalously high orbital inclination of Miranda. Submitted for publication.

WALKER, G. H., AND J. FORD 1969. Amplitude instability and ergodic behavior for conservative nonlinear oscillator systems. *Phys. Rev.* **188,** 416–432.

WISDOM, J. 1980. The resonance overlap criterion and the onset of stochastic behavior in the restricted three-body problem. *Astron. J* **85,** 1122–1133.

WISDOM, J. 1982. The origin of the Kirkwood gaps: A mapping for asteroidal motion near the 3/1 commensurability. *Astron. J.* **87,** 577–593.

WISDOM, J. 1983. Chaotic behavior and the origin of the 3/1 Kirkwood gap. *Icarus* **56,** 51–74.

WISDOM, J. 1985a. A perturbative treatment of motion near the 3/1 commensurability. *Icarus* **63,** 272–289.

WISDOM, J. 1985b. Meteorites may follow a chaotic route to Earth. *Nature* **315,** 731–733.

WISDOM, J. 1987. Chaotic dynamics in the Solar System. *Icarus* **72,** 241–275.

WISDOM, J., S. J. PEALE, AND F. MIGNARD 1984. The chaotic rotation of Hyperion. *Icarus* **58,** 137–152.

WISDOM, J., AND W. C. TITTEMORE 1988. A map for the Hénon–Heiles problem. In preparation.

YODER 1979. Diagrammatic theory of transition of pendulum-like systems. *Celest. Mech.* **19,** 3–29.